UNIVERSIDADE FEDERAL DE MINAS GERAIS
Programa de Pós-Graduação em Engenharia Mecânica

METHODOLOGY FOR ANALYSIS OF BOUNDARY CONDITIONS IN ORDER TO INCREASE ACCURACY ASSOCIATED TO INTERNAL COMBUSTION ENGINE CFD 3D MODELS

LEONARDO GUIMARÃES FONSECA

Belo Horizonte
2019

Leonardo Guimarães Fonseca

METHODOLOGY FOR ANALYSIS OF BOUNDARY CONDITIONS IN ORDER TO INCREASE ACCURACY ASSOCIATED TO INTERNAL COMBUSTION ENGINE CFD 3D MODELS

Tese apresentada ao Programa de Pós-Graduação em Engenharia Mecânica da Universidade Federal de Minas Gerais , como requisito parcial à obtenção do título de Doutor em Engenharia Mecânica.

Área de Concentração: Energia e Sustentabilidade

Orientador: Prof. Dr. Ramon Molina Valle

Belo Horizonte
2019

Leonardo Guimarães Fonseca
METHODOLOGY FOR ANALYSIS OF BOUNDARY CONDITIONS IN ORDER TO INCREASE ACCURACY ASSOCIATED TO INTERNAL COMBUSTION ENGINE CFD 3D MODELS/ Leonardo Guimarães Fonseca. – Belo Horizonte, 2019-
156 p. : il. (algumas color.) ; 30 cm.

Supervisor: Prof. Dr. Ramon Molina Valle

Tese – Universidade Federal de Minas Gerais , 2019.

1. cfd 3d. 2. rans. 3. internal combustion engines. 4. intake pressure. 5. wall temperature. I. Universidade Federal de Minas Gerais. II. Escola de Engenharia. III. METHODOLOGY FOR ANALYSIS OF BOUNDARY CONDITIONS IN ORDER TO INCREASE ACCURACY ASSOCIATED TO INTERNAL COMBUSTION ENGINE CFD 3D MODELS

UNIVERSIDADE FEDERAL DE MINAS GERAIS
PROGRAMA DE PÓS-GRADUAÇÃO EM
ENGENHARIA MECÂNICA
Av. Antônio Carlos, 6627 - Campus Universitário
31270-901 – Belo Horizonte – MG
Tel.:+55 31 3409.5145
E-mail: cpgmec@demec.ufmg.br

"METHODOLOGY FOR ANALYSIS OF BOUNDARY CONDITIONS IN ORDER TO INCREASE ACCURACY ASSOCIATED TO INTERNAL COMBUSTION ENGINE CFD 3D MODELS"

LEONARDO GUIMARÃES FONSECA

Tese submetida à Banca Examinadora designada pelo Colegiado do Programa de Pós-Graduação em Engenharia Mecânica da Universidade Federal de Minas Gerais, como parte dos requisitos necessários à obtenção do título de **"Doutor em Engenharia Mecânica"**, na área de concentração de **"Energia e Sustentabilidade".**

Tese aprovada no dia 03 de outubro de 2019.

Por:

Prof. Ramon Molina Valle
Orientador - Departamento de Engenharia Mecânica/ UFMG

Prof. Rudolf Huebner
Departamento de Engenharia Mecânica/ UFMG

Prof. Sérgio de Morais Hanriot
Departamento de Engenharia Mecânica/ PUC-MINAS

Prof. André Augusto Campagnole dos Santos
Centro de Desenvolvimento da Tecnologia Nuclear/ CDTN

Prof. Jose Guilherme Coelho Baeta
Departamento de Engenharia Mecânica/ UFMG

Aos meus pais, Lincoln e Vânia;

Às minhas avós, Alvicina(in memoriam) and Terezinha(in memoriam).

ACKNOWLEDGEMENTS

The author acknowledge the following persons and institutions, for their fundamental role in this work:

- CTM-UFMG, for the infrastructure which was made available for the implementation of this thesis;
- CAPES (Coordination for the Improvement of Higher Education Personnel) for the scholarship from the program "CAPES - DEMANDA SOCIAL", PhD level;
- FCA Latin America, for the research project in partnership with UFMG, the very begining of this project;
- DETEM/UFSJ (Telecommunications and Mechatronic Engineering Department - Federal University of São João del-Rei), for the support conceived to this thesis since may 2018;
- CMT - Motores Térmicos, for the partnership and for the hospitality;
- Prof. Ramon Molina, for his support since the master degree;
- Prof. Rudolf Huebner, for his support since the under graduation simulation projects;
- Prof. Sérgio de Morais Hanriot, Dr. André Augusto Campagnole dos Santos, Prof. José Guilherme Coelho Baeta, for their contribution to this thesis;
- Prof. Ricardo Novella and Prof. Pablo Olmeda, for the partnership and for the good work performed together;
- Prof. Guilherme Gomes, for the support concerning my dedication to this project.

The author is very grateful.

AGRADECIMENTOS

Primeiramente, agradeço a Deus, princípio, meio e fim de todas as coisas, a luz mais brilhante na caverna mais sombria. A cada conquista, seja sempre o primeiro agradecimento do coração, dar glórias a Deus no mais alto dos céus!!!

À minha esposa Jéssica, companheira de todos os momentos, dos mais fáceis aos mais sombrios. O meu está concluído, agora está com você princesa, é a sua vez!

Aos meus pais, Lincoln e Vânia, as joias mais raras que Deus presenteou a mim e a meus irmãos Flávia, Rodrigo e Lucas. Minha família, meu refúgio, minha rocha e proteção, abrigo durante as tempestades, as muitas que aconteceram nos últimos 4 anos. Aos meus tios e primos, Virgínia, Gilmar, Dudu e Elisa, Anderson, Patrícia, Heitor e Henrique, com quem estou imensamente em falta, mas espero me redimir!

Às minhas avós, Alvicina (*in memorian*) e Terezinha (*in memorian*), que deixaram mais que ensinamentos e exemplos, deixaram um legado de caráter, determinação, obstinação e perseverança, que caminharam tanto conosco antes do início deste processo, mas que durante este processo concluíram suas jornadas.

Aos colegas do CTM, Oscar, Carlos, Vinícius Gaúcho, Vinícius Rimsa, Lucimar, Natalia, Arthur, José Arthur, Bryan, Juan, que compartilharam momentos difíceis e confraternizações ao longo dos últimos anos.

Aos colegas do LCFD, Raphael, Clarissa e Filipe, os herdeiros deste legado em simulação CFD 3D de motores de combustão interna.

Ao secretário do CTM, Alexandre, sempre um bom amigo, nas horas fáceis, difíceis, sempre eficiente e fiel ao CTM.

Ao Prof. Ramon Molina e Ao Prof. Rudolf Huebner, mais que exemplos, grandes amigos, os únicos que ousaram acreditar neste projeto, quando todos os demais acreditaram que eu deveria desistir.

Aos colegas do DETEM/UFSJ, Guilherme, Edgar, Rina, Tarsis, Cláudio, Leandro, Diego, Alfredo, muito trabalho, muitos desafios e muitas alegrias nos aguardam. Vamos juntos!

De modo geral, a todas as pessoas que contribuíram comigo durante este processo, e que não tiveram seus nomes citados acima...

MUITO OBRIGADO!!!

"*...rise and rise again, until lambs become lions...*" (Autor desconhecido. Robin Hood, 2010.)

ABSTRACT

The use of internal combustion engine simulation models for aiding the development of more efficient and less pollutant engines is by so far known. Engine CFD 3D models are a new tool for this development, although its methodology still needs some improvement in order to systematically produce accurate results. In this thesis, a method for analysis and treatment of boundary conditions for engine CFD 3D models using RANS approach is presented, which should be capable of producing accurate results for different engine operating conditions using the same values for all of the constants of the sub models for turbulence, spray and combustion, so the engine CFD 3D model would be used in a systematic and repetitive way. For intake pressure boundary conditions, a correction for pulsating flow effects is applied, and for wall temperature, the engine CFD 3D results for heat transfer coefficient are used decoupled iteratively with a zero dimensional heat transfer model. The method is applied to a naturally aspired single cylinder research engine available at CTM-UFMG, fueled with commercial ethanol, for which geometry information and experimental data are available. For the engine CFD 3D model with experimental data intake pressure boundary conditions, the results obtained for injected mass of fuel, lambda and trapped mass of air are compared to experimental data, and excess of air is observed for six different engine operating conditions. The results obtained by the engine CFD 3D model, using corrected intake pressure boundary conditions, are presented for injected mass of fuel, lambda and trapped mass of air for six different engine operating conditions, using two different sets of wall temperature boundary conditions calculated by the zero dimensional heat transfer model. For all of those results, the difference to experimental correlated data is systematically reduced in comparison with the direct use of experimental data for intake pressure boundary conditions. In cylinder pressure trace is compared between experimental data and three different sets of boundary conditions for two selected engine operating conditions, once the trends observed for the selected conditions are representative. The results obtained by the proposed method present better agreement to experimental correlated data than the direct use of experimental data for intake pressure boundary condition, specially during compression and expansion strokes. It is concluded that for this specific naturally aspired engine, pressure correction of intake experimental boundary conditions is mandatory for performing engine CFD 3D modelling using RANS approach. Once the method has been applied in only one engine, it is only possible to infer, and not to state, that pressure correction of intake experimental boundary conditions is mandatory for this application.

Keywords: CFD 3D, RANS, Internal Combustion Engines, Intake Pressure, Wall Temperature

RESUMO

O uso de modelos para simulação de motores de combustão interna, com objetivo de desenvolver motores mais eficientes e menos poluentes, é prática comum tanto na indústria quanto nos centros de pesquisa. Modelos CFD 3D para motores de combustão interna são uma nova ferramenta para esta aplicação, contudo sua metodologia ainda precisa de algum desenvolvimento para produzir sistematicamente resultados confiáveis. Nesta tese, é apresentada uma metodologia para análise das condições de contorno implementadas em modelos CFD 3D de motores de combustão interna que utilizam o tratamento RANS para turbulência, sendo que esta metodologia deve ser capaz de produzir resultados confiáveis para diferentes condições de operação do motor utilizando sempre os mesmos valores para todas as constantes dos sub modelos relacionados a turbulência, "spray" e combustão. Para condições de contorno de pressão na admissão, uma correção é aplicada aos dados experimentais devido ao efeito do escoamento pulsante na admissão, enquanto para as temperaturas de parede, os resultados do modelo CFD 3D para coeficiente de transferência de calor são usados de forma iterativa desacoplada com um modelo de transferência de calor zero dimensional. A metodologia é aplicada a um motor monocilindro de pesquisa aspirado disponível no CTM-UFMG, utilizando etanol comercial, em relação ao qual informações sobre geometria e dados experimentais foram disponibilizados para esta pesquisa. Para o modelo CFD 3D utilizando dados experimentais como condição de contorno de pressão na admissão, os resultados obtidos para massa de combustível injetada, lambda e massa de ar aprisionada são comparados com dados experimentais, e é constatado excesso de ar para seis diferentes condições de operação do motor. Os resultados obtidos pelo modelo CFD 3D, utilizando pressão corrigida como condição de contorno na admissão, são apresentados para massa de combustível injetada, lambda e massa de ar aprisionada para todos os casos, usando dois tipos de condição de contorno de temperatura de parede calculados pelo modelo zero dimensional de transferência de calor. Para todos os resultados, a diferença em relação aos dados experimentais correlatos é sempre menor que a obtida pelo uso direto dos dados experimentais de pressão na admissão como condição de contorno. Os resultados do modelo CFD 3D utilizando pressão corrigida como condição de contorno na admissão também apresentam melhor correlação com dados experimentais correlatos em comparação com os obtidos pelo mesmo modelo usando diretamente dados experimentais para a mesma condição de contorno, em termos do comportamento da pressão dentro do cilindro ao longo do ciclo e da temperatura dentro do cilindro ao longo do ciclo. Conclui-se que para o motor monocilindro aspirado em análise, a correção da condição de contorno de pressão na admissão é obrigatória para a modelagem CFD 3D de motores de combustão interna utilizando tratamento RANS para turbulência.

Palavras chave: CFD 3D, RANS, Motores de Combustão Interna, Pressão da Admissão, Temperatura de Parede

LIST OF FIGURES

LIST OF TABLES

NOMENCLATURE

Abbreviations

CO_2	Carbon Dioxide
NO_X	Generic Nitrogen Oxide
0D	Zero Dimensional
1D	One Dimensional
2D	Two Dimensional
3D	Three Dimensional
AKTIM	Ark and Kernel Tracking Ignition Model
ANSYS	Trade name of ANSYS INC.
ASME	The American Society of Mechanical Engineers.
BDC	Bottom Dead Center
CAD	Crank Angle Degrees
CCV	Cycle to Cycle Variations
CFD	Computational Fluid Dynamics
CFX	Trade name of a commercial software, which actually belongs to ANSYS INC.
CHT	Conjugate Heat Transfer
COV	Co Variance
CTM	*Centro de Tecnologia da Mobilidade*, (Mobility Technology Center, from Portuguese)
dim	Dimensionless
DISI	Direct Injection Spark Ignition
DNS	Direct Numerical Simulation
ECFM-3Z	Extended Coherent Flame Model - Three Zones
EGR	Exhaust Gas Recirculation

HPC	High Performance Computing
HT	Heat Transfer
ICE	Internal Combustion Engines
IMEP	Indicated Mean Effective Pressure
KIVA	Trade name of an open source software
KIVA-3V	Trade name of an open source software
LES	Large Eddy Simulation
PDF	Probability Density Function
PISO	Pressure Implicit with Splitting of Algorithm
PIV	Particle Image Velocimetry
RANS	Reynolds Averaged Navier Stokes
RNG	Re Normalization Group
SGS	Sub Grid Scale
STAR-CD	Trade name of a commercial software, which actually belongs to SIEMENS GmBH.
TDC	Top Dead Center
THC	Total Hydrocarbon
UFMG	*Universidade Federal de Minas Gerais* (Federal University of Minas Gerais, from Portuguese)

Greek symbols

α	ECFM-3Z model constant [-]
β	ECFM-3Z model constant [-]
$\delta(Z)$	Probability density function for unmixed air zone [-]
$\delta(Z-1)$	Probability density function for unmixed fuel zone [-]
$\delta(Z-\overline{Z}^M)$	Probability density function for mixture zone [-]
ε	Dissipation of turbulent kinetic energy $[m^2/s^3]$

ε_{cyl}	Weighting factor for heat transfer between valve stem surface and port gas flow, for which the reference is the heat transfer modeled as flow past a cylinder
$\overline{\rho}$	Flow field average density $[kg/m^3]$
ϕ	Generic trasport variable [-]
ϕ_{i+1}	Value of the generic variable ϕ at grid $i+1$ [-]
ϕ_i	Value of the generic variable ϕ at grid i [-]
Σ	Flame surface density $[m^2/m^3]$

Latin symbols

$\overline{I}$	Flow field average total internal energy $[kJ]$
$\overline{P}$	Flow field average pressure $[Pa]$
$\overline{T}$	Flow field average temperature $[K]$
$\overline{U}$	Flow field average velocity component $[m/s]$
$\overline{V}$	Flow field average velocity component $[m/s]$
$\overline{W}$	Flow field average velocity component $[m/s]$
$\overline{Z}^M$	Average Mixture Fraction [-]
$\vec{\overline{U}}$	Flow field average velocity vector $[m/s]$
A	Air plus Exhaust Gas Recirculation Zone [-]
A_{cc}	Area of the combustion chamber for the global heat transfer model $[m^2]$
A_{exh}	Area of the exhaust port for the global heat transfer model $[m^2]$
A_{int}	Area of the intake port for the global heat transfer model $[m^2]$
$A_{lin,ext}$	Area of cylinder outside surface exposed to coolant flow $[m^2]$
c	Reaction progress variable [-]
C'_{gal}	Constant in the equation for thermal conductance between piston surface and oil [-]
C_2	Constant in the Woschni equation [-]
C_u	Constant in the Woschni equation [-]

C_{w1}	Constant in the Woschni equation [-]
C_{w2}	Constant in the Woschni equation [-]
D	Generic experimental measurement [-]
D_{curv}	Port curvature diameter [m]
D_{cyl}	Cylinder diameter (bore) in the Woschni equation [m]
D_{gal}	Piston inner diameter in the region of the lubricating oil gallery [m]
d_{gal}	Diameter or hydraulic diameter of the piston lubricating oil gallery [m]
D_{pis}	Piston diameter [m]
D_{port}	Port diameter or hydraulic diameter [m]
E	Generic comparison error [-]
e_{cc}	Thickness of the combustion chamber for the global heat transfer model
e_{exh}	Thickness of the exhaust port for the global heat transfer model
e_{int}	Thickness of the intake port for the global heat transfer model
e_{lin}	Thickness of the cylinder wall for the global heat transfer model
F	Unburned Fuel Zone [-]
h	Grid characteristic length [mm]
h_{coarse}	Characteristic length of a coarse grid [mm]
$h_{cylinder}$	Heat transfer coefficient between valve stem surface and port gas flow, modeled as flow past a cylinder [W/m^2K]
h_{fine}	Characteristic length of a fine grid [mm]
$h_{flatplate}$	Heat transfer coefficient between valve stem surface and port gas flow, modeled as flow past a flat plate [W/m^2K]
$h_{gal-cool}$	Heat transfer coefficient between head cooling gallery surface and coolant flow [W/m^2K]
h_{gas}	Heat transfer coefficient for in cylinder gas [W/m^2K]
$h_{lin-cool}$	Heat transfer coefficient between cylinder outside surface and coolant flow [W/m^2K]

$h_{lin-oil}$ Heat transfer coefficient between cylinder liner surface and oil $[W/m^2K]$

h_{pc} Piston ring height $[m]$

$h_{pis-lin}$ Heat transfer coefficient between piston surface and cylinder liner surface $[W/m^2K]$

$h_{portcurv}$ Heat transfer coefficient between port surface and port gas flow, for curved tube approximation $[W/m^2K]$

$h_{stemgas}$ Heat transfer coefficient between valve stem surface and port gas flow $[W/m^2K]$

$h_{straighttube}(x=\infty)$ Heat transfer coefficient between port surface and port gas flow, for straight tube approximation in fully developed flow $[W/m^2K]$

k Turbulent kinetic energy $[m^2/s^2]$

K_{cc-gal} Thermal conductance between combustion chamber surface and head cooling gallery surface $[W/K]$

k_{cc} Thermal conductivity of the cylinder wall, for the global heat transfer model $[W/m.K]$

k_{cc} Thermal conductivity of the engine head in the region of the combustion chamber, for the global heat transfer model $[W/m.K]$

$K_{exh-gal}$ Thermal conductance between exhaust port surface and head cooling gallery surface $[W/K]$

k_{exh} Thermal conductivity of the engine head in the region of the exhaust port, for the global heat transfer model $[W/m.K]$

$K_{gal-cool}$ Thermal conductance between head cooling gallery surface and coolant flow $[W/K]$

$K_{gas-head}$ Thermal conductance between in cylinder gases and combustion chamber surface $[W/K]$

$K_{gas-lin}$ Thermal conductance between in cylinder gases and cylinder liner surface $[W/K]$

$K_{gas-pis}$ Thermal conductance between in cylinder gases and piston surface $[W/K]$

$K_{gas-valv}$ Thermal conductance between in cylinder gases and valve surface $[W/K]$

$K_{int-gal}$ Thermal conductance between intake port surface and head cooling gallery surface $[W/K]$

k_{int}	Thermal conductivity of the engine head in the region of the intake port, for the global heat transfer model $[W/m.K]$
$K_{lin-cool}$	Thermal conductance between cylinder liner surface and coolant flow $[W/K]$
$K_{lin-oil}$	Thermal conductance between cylinder liner surface and oil $[W/K]$
$K_{pis-lin}$	Thermal conductance between piston surface and cylinder liner surface $[W/K]$
$K_{pis-oil}$	Thermal conductance between piston surface and oil $[W/K]$
k_{pis}	Thermal conductivity of the piston, for the global heat transfer model $[W/m.K]$
M	Mixture Zone [-]
m	Constant in the equation for thermal conductance between piston surface and oil [-]
N	Total number of finite volumes in a grid [-]
$Nu_{cylinder}$	Nusselt number for heat transfer between valve stem and port gas flow, modeled as flow past a cylinder [dim]
$Nu_D(x)$	Nusselt number for heat transfer between port surface and port gas flow, for turbulent entrance length flow [dim]
$Nu_D(x=\infty)$	Nusselt number for heat transfer between port surface and port gas flow, for turbulent fully developed flow [dim]
$Nu_{flatplate}$	Nusselt number for heat transfer between valve stem and port gas flow, modeled as flow past a flat plate [dim]
p_{ivc}	Pressure of the in cylinder gases at intake valve closing [bar]
r	Grid refinement ratio [dim]
Re	Reynolds number [dim]
S	Generic simulation result [-]
S_{cyl}	Cylinder stroke $[m]$
S_p	Average piston speed for the global heat transfer model [-]
$T_{gas-head}$	Cycle average in cylinder gas temperature, as it is seen by combustion chamber surface [K]

$T_{gas-lin}$	Cycle average in cylinder gas temperature, as it is seen by cylinder liner surface [K]
$T_{gas-pis}$	Cycle average in cylinder gas temperature, as it is seen by piston surface [K]
$T_{gas-valv}$	Cycle average in cylinder gas temperature, as it is seen by valve surface [K]
T_{ivc}	Temperature of the in cylinder gases at intake valve closing [K]
$U_{95\%}$	Uncertainty of a given result, for a 95% confidence interval [-]
V_D	Displaced volume in the Woschni equation [-]
V_{ivc}	Volume of the in cylinder gases at intake valve closing [m^3]
V_i	Volume of the i_{th} cell [mm^3]
x	Port length for heat transfer between port surface and port gas flow [m]
Z	Mixture fraction variable [-]
P _1aIT	Results for in cylinder pressure trace obtained by engine CFD 3D model using fitted intake pressure boundary conditions along with first iteration wall temperatures calculated by global heat transfer model [bar]
P _2aIT	Results for in cylinder pressure trace obtained by engine CFD 3D model using fitted intake pressure boundary conditions along with second iteration wall temperatures calculated by global heat transfer model [bar]
P _envelope	Experimental data for in cylinder pressure, associated to the dispersion of the 200 cycles for in cylinder pressure experimental data [bar]
P _EXP	Experimental data for in cylinder pressure trace [bar]
P _max	Maximum pressure of in cylinder pressure trace (peak pressure) [bar]
P _piexp	Results for in cylinder pressure trace obtained by engine CFD 3D model using experimental data intake pressure boundary conditions along with first iteration wall temperatures calculated by global heat transfer model [bar]

CONTENTS

1 INTRODUCTION

Engine simulation models are valuable tools for engineers either working in the automotive industry or belonging to the research community, with the aim to design engines that comply with the strict emissions legislation while keeping high performance(PARIOTIS E.G.; RAKOUPOULOS, 2012; BERNARD; LEBAS; DEMOULIN, 2011; GE et al., 2009). The simulation of internal combustion engines (ICE) is an essential part of the engine design process. It is used for preliminary design studies and for diagnostics in the case of unexpected phenomena caused by fluid flow, fuel-air mixture or combustion (BUHL et al., 2017).

The increasing acceptance and significance of 3D CFD as a reliable tool for the combustion process design is mainly due to two aspects. On one hand, significant progress has been achieved in describing physical and chemical processes such as the turbulent fluid flow, turbulent combustion or pollutant formation. Sometimes this even allows numerical predictions without parallel verification by experiments. On the other hand, there is an increase in the availability of high-performance computing (HPC) resources in combination with CFD software capable of using those resources efficiently (HASSE, 2016).

A major challenge for combustion scientists and engine development engineers is to optimize engine combustion for improved fuel economy and reduced exhaust emissions while maintaining outstanding performance, durability, and reliability at an affordable price (MILLO et al., 2014; ALKIDAS, 2007; DRAKE; HAWORTH, 2007). The stringent environmental constraints have led the industry to look for new technologies that improve the design of ICE, mainly focused on achieving higher thermal efficiency and reducing pollutant emissions. Numerical simulations play a key role for optimizing engine design, but modelling the physical processes such as the combustion and the heat transfer to the walls, represents a challenge due to the complexity of the *phenomena* involved (BROATCH et al., 2019).

Although current research favours alternative and eco-friendly energy sources in order to reduce the environmental damage caused by fossil fuels, the difficulties still encountered to replace internal combustion engines for transport mean that these will probably remain important for the automobile market in the coming years, if only as part of the hybrid solutions (BROATCH et al., 2019).

Over the years, researchers have tried to simulate the combustion process in engines in order to predict emissions at different operation conditions without having to perform many expensive experimental tests. However, it is still difficult to obtain accurate results with any model, and development is still ongoing to improve them (BROATCH et al., 2019).

Similar to other engineering applications, internal combustion engines development is nowadays aided by computational fluid dynamics (CFD) models. Those models use, in majority, finite volume method to solve transient reactive flow inside the cylinder, intake and exhaust ducts.

1.1 ENGINE CFD 3D MODELS

The three dimensional (3D) simulation of fluid flow and combustion processes using computational fluid dynamics (CFD) has become an essential part of the engine design process. Especially in the early development phase, sometimes even before hardware is available, simulation results allow engine performance to be estimated. In combination with experimental investigations and zero dimensional (0D) or one dimensional (1D) process simulation, engine CFD 3D can be used to evaluate specific engine parts (such as an intake port) or even whole concepts. This can help in identifying the most promising variants for further detailed studies. In fact, the combined use of experiment and simulation is a major contributor to reduced cost and development time (Adapted from (HASSE, 2016)).

Selection of CFD models is mainly determined by flow regime, target accuracy, and available computational resources (XING, 2015). Three main approaches are available for engine CFD 3D simulation: DNS, LES and RANS. Direct numerical simulation (DNS) is mainly used as a fundamental research tool for understanding flow physics at low or moderate Reynolds (Re) numbers (XING, 2015), this way DNS simulations applied to internal combustion engines are found in literature only for simplified geometries (SCHMITT et al., 2016b).

Considering high Re, turbulence models are needed such as Reynolds-averaged Navier-Stokes (RANS), large eddy simulation (LES), and hybrid RANS/LES. LES solves spatially filtered Navier Stokes equations such that large scales of the turbulent flow field are better resolved than RANS and the smallest and most expensive scales of the solution are modeled using sub-grid scale (SGS) models (XING, 2015). Due to prohibitive computational costs, ICE simulations in industrial applications are still mainly limited to the Reynolds-averaged Navier–Stokes (RANS) framework (ŠARIĆ; BASARA; ŽUNIČ, 2017), although several authors in literature perform engine CFD 3D analysis using LES approach, even if it is for simplified geometries.

Engine CFD 3D models using RANS approach have been widely used for several purposes, for its low computational cost relative to LES approach. In the RANS approach, all turbulent scales are modeled and consequently RANS approaches provide only information about a typical, average cycle (MASOULEH et al., 2018; ROBERT et al., 2015).

Multidimensional simulations, such as RANS and LES techniques, solve the governing equations for mass, momentum, energy, and species conservation, together with an appropriate turbulence closure model (MA et al., 2017). Sub models are used to simplify, inside the three dimensional flow field, phenomena which would make solution more complex or even unfeasible. Complex phenomena are represented by sub models inside engine CFD 3D model for reactive flow inside the engine. Among these models, some examples are:

- Turbulent flow related sub model

- Fuel injection related sub model
- Combustion related sub model

The entire set of equations is resolved for a finite volume grid which is modified each time step to accommodate piston and valves movement, still not allowing great deformations of mesh volumes. Techniques for adding and removing cells are used to represent the effect of mobile parts displacement at the reactive flow field inside the cylinder.

The maturing of Computational Fluid Dynamics (CFD) codes for practical calculations of complex turbulent flows comes with a need to establish the credibility of the results. Either the demands of end-users of the results or just scientific interest will sooner or later persuade or force the numerical analyst to assess the quality of his work. This quality assessment is commonly denoted as Verification & Validation (EÇA; HOEKSTRA, 2014).

Accuracy of measurement is defined by the guide to the expression of uncertainty in measurement (JCGM, 2008) as the closeness of the agreement between the result of a measurement and a true value of the measurand. The concept of accuracy of a computational simulation is used several times in standard ASME V&V 20 (ASME, 2009), although there is not a statement for definition of such concept. Once there are several uses of such concept in (ASME, 2009), in this thesis accuracy of a computational simulation is used similar to their use, which is also an adaption of the concept stated in (JCGM, 2008) for accuracy of measurement. Thus, in this thesis, accuracy of a computational simulation is considered the closeness of the agreement between the result of a simulation and the experimentally measured value. Indeed, this concept is very close to the numerical definition of validation comparison error E, defined by Equation 1.1 (ASME, 2009):

$$E = S - D \tag{1.1}$$

where S is the value of a selected simulation result, and D is the value of the corresponding experimental measurement.

The great majority of recent papers in literature concerning engine CFD 3D modelling perform qualitative validation, in general, for in cylinder pressure trace comparison with experimental results. Many times, the comparison is performed for the full range of time and pressure, which can hide several differences between numerical and experimental results. Concerning engine CFD 3D modelling using RANS approach, the validation is performed after tuning the constants of some sub model, perhaps the combustion sub model, for a single engine operating condition. Indeed, it has been found one paper in literature which presents results for one supercharged engine, at two different loads, which are maximum power and maximum torque conditions (BERNI; CICALESE; FONTANESI, 2017). Moreover, no paper in literature has been found presenting results, validated or not, for more than one engine operating conditions.

This way, it is a major challenge in this thesis to present engine CFD 3D results for a given engine at different engine operating conditions without changing the values of sub models constants, in such a manner those results are accurate for all of the presented engine operating conditions.

1.2 PULSATING EFFECTS ON INTAKE FLOW

The intake manifold is a system designed to deliver air to the engine through pipes connected to each cylinder, called runners. The lengths of these pipes, and to a certain extent their diameters, must be chosen carefully as they will determine the resonant frequencies of the manifold (SOUZA et al., 2019). This geometry parameters influences the amount of the intake air mass flow which, in turn, is also hampered by the interference of the pressure fluctuations generated in the pistons and valves (HANRIOT; QUEIROZ; MAIA, 2019).

The effects of pulsating flow at intake ducts (manifolds, runners, ports) of internal combustion engines are known and have long time been studied (HANRIOT, 2001; CEVIZ, 2007; PEREIRA, 2008). Most of the authors in literature highlight the design of the intake system in order to take advantage of ram or tunning effects (CEVIZ, 2007; HANRIOT; QUEIROZ; MAIA, 2019; SOUZA et al., 2019), or the use of different strategies to improve engine breathing, for example varying intake plenum length or using a Helmholtz resonator (HANRIOT; QUEIROZ; MAIA, 2019).

One important effect concerning pulsating flow at intake ducts of internal combustion engines is the reduction of the volumetric efficiency, which occurs at naturally aspired engines without any specific device (Helmholtz resonator) or design (variable length plenum) to improve volumetric efficiency. This effect can be seen as a reduction in the trapped mass of air per cycle by an engine cylinder. Some authors studied steady intake flow by means of engine CFD 3D simulation (GIANNAKOPOULOS et al., 2017; INAGAKI et al., 2010), but none of them considered the effect of intake pulsating flow over volumetric efficiency. Most of the models that takes into account pulsating flow effects over in cylinder trapped mass of air are 0D or 1D.

Concerning engine CFD 3D models using RANS approach for turbulence, it has not been found in literature any publication referring to its use to capture the effects of intake pulsating flow over volumetric efficiency. It is implicit in this situation that engine CFD 3D models using RANS approach can not capture the effect of pulsating flows over volumetric efficiency.

Although there is no report in literature concerning engine CFD 3D modelling using RANS approach for turbulence capturing the effects of pulsating flow over in cylinder volumetric efficiency, in terms of trapped mass of air, it is of common use to perform engine CFD 3D analysis using RANS approach, in order to reduce computational cost. The boundary conditions used for those simulations are intake and exhaust pressure and temperature, measured or modeled. Considering verification and validation trends for engine CFD 3D

models, only measured boundary conditions should be used.

The main contribution of this thesis is the consideration of intake pulsating flow effect over volumetric efficiency, by means of a procedure for treatment of intake pressure boundary conditions.

1.3 WALL TEMPERATURE BOUNDARY CONDITIONS

In addition to sub-models focusing on turbulence, spray, and combustion, attention has been especially paid on the heat flux on combustion chamber wall. The wall heat transfer can contribute to a significant heat loss in the overall fuel conversion process, and the in cylinder combustion processes and engine operation can also be affected. In addition, the wall heat flux determines the distribution of thermal stress in the mechanical components of the engine. Consequently, an accurate calculation of the chamber wall heat transfer is essential to improve the performance of engine simulation, which thereby can be more helpful in the design of more fuel efficient engines (ZHANG, 2018).

Among other boundary conditions, temperature of engine internal surfaces in contact with the reactive flow is essential for any combustion model to represent properly in cylinder phenomena. However, it is difficult and expensive to measure material temperatures. Some authors use thermocouples to directly measure temperature at specific points of in cylinder surface in contact with reactive flow field (BROATCH P. OLMEDA; WAREY, 2017; TORREGROSA et al., 2017; GÜRBÜZ, 2016; FINOL; ROBINSON, 2006; FINLAY et al., 1988; ALKIDAS, 1993). Although, direct measurement of engine internal surface temperatures involves drilling of the engine structure and other complicated operations (BROATCH P. OLMEDA; WAREY, 2017; TORREGROSA et al., 2017). Because of its complicated geometry, positioning thermocouples in the cylinder head is a delicate operation. To measure the piston temperature, a wireless transmission system is required.

An alternative to measurements is numerical simulation (TORREGROSA et al., 2006). In literature, some authors studied internal combustion engine heat transfer modelling and wall temperature calculation from engine operation parameters (BAKER; ASSANIS, 1994; BOHAC; BAKER; ASSANIS, 1996; TORREGROSA et al., 2006; PIEDRAHITA, 2009; TORREGROSA P. OLMEDA; ROMERO, 2011). Some references uses finite element models to calculate iteratively in cylinder reactive flow field and wall heat transfer, which is commonly named as conjugate heat transfer (CHT)(BROATCH et al., 2019; KIKUSATO; KUSAKA; DAISHO, 2015). Some authors perform finite element modelling of specific engine parts, like pistons using ceramic coating (DUDAREVA; ENIKEEV; IVANOV, 2017), although no reference was found in literature for the use of heat transfer models and correlations to obtain boundary conditions for engine CFD 3D models.

1.4 OBJECTIVES

Considering the trends observed in literature for engine CFD 3D model using RANS approach for turbulence and its qualitative validation at a single engine operating condition after tuning sub model parameters, the pulsating flow effects over volumetric efficiency and the wall temperature boundary conditions for engine CFD 3D models, the following objectives are proposed for this thesis, in order to contribute to engine CFD 3D modelling state of the art.

1.4.1 General objective

To develop a methodology for CFD 3D simulation of the thermal fluid dynamics processes inside internal combustion engines (engine CFD 3D modelling), using RANS approach for turbulence, which is capable of producing accurate results for different engine operating conditions using the same values for all of the constants of the sub models. The proposed methodology must takes into account intake pulsating flow effects over trapped mass of air, and should resolve a heat transfer model decoupled iteratively with engine CFD 3D model in order to calculate surface temperature of engine internal surfaces.

1.4.2 Specific objective

To achieve general objective, the following specific objectives are defined:

1. Implement different heat transfer models available in literature, in such a manner to calculate engine internal surface temperatures in contact with the reactive flow field inside the cylinder, at intake and exhaust ducts;

2. Apply the heat transfer model for calculation of surface temperatures of the selected engine at one of the operating conditions;

3. For a selected engine operating condition, use engine surface temperature calculated at previous specific objective to resolve engine CFD 3D model of the selected engine, using experimental data for intake pressure boundary condition;

4. Calculate a correction for intake pressure boundary condition, concerning the effects of intake pulsating flow at in cylinder trapped mass of air;

5. Resolve decoupled iteratively heat transfer and CFD 3D models, using fitted pressure as boundary conditions for engine CFD 3D, until there is convergence of the heat transfer model;

6. Implement the previous specific objectives for different engine operating conditions of the selected engine, without changing the constants of any of the engine CFD 3D sub models, whether they are related to flow, spray or combustion;

7. Compare the results obtained using different sets of boundary conditions, concerning intake pressures and wall temperatures, for all of the operating conditions evaluated, in order to verify if the proposed methodology is capable of increasing the accuracy of engine CFD 3D model results, for a given engine at different engine operating conditions, without tuning the constants of any sub model.

2 LITERATURE REVIEW

In chapter 2, it is presented the literature review concerning the most important topics about reciprocating engine thermal fluid dynamic modelling, which are used in this thesis. Each topic in this literature review contain a brief description of the concepts used in the methodology described in chapter 3, along with several literature references for more in depth discussions. In section 2.1, basic concepts are presented. In section 2.2, the basis of engine CFD 3D modelling are presented. In section 2.3, some literature information about intake pulsating flow is presented. In section 2.4, the basis of engine heat transfer modelling, which is subject of an original literature review paper as a product of this thesis, is presented. Finally, in section 2.5, the most recent publications concerning the topics of this literature review are presented.

2.1 BASIC CONCEPTS

Aiming at offering a better comprehension for the methodology applied in this thesis to internal combustion engine CFD 3D simulation, it is necessary some information about fundamental concepts related to the topic. With this objective, it is made a brief description of basic concepts related to reciprocating internal combustion engines, mathematical modelling of internal combustion engines, and computational fluid dynamics (CFD) using RANS approach for turbulence. For sake of brevity, some references with more extensive explanation are pointed out for each topic.

2.1.1 Reciprocating internal combustion engine

The history of reciprocating internal combustion engine is interesting and involves more than one century of development and application, although the operation principle remains the same since it's invention. According to (HEYWOOD, 2018), internal combustion engine are used since 1876, when Nicolaus Otto developed the first spark ignition engine, and 1892, when Rudolf Diesel developed the first compression ignition engine.

The purpose of internal combustion engines is the production of mechanical power from the chemical energy contained in the fuel (HEYWOOD, 2018). In reciprocating engines, piston moves back and forth inside a cylinder and transfer power to engine crankshaft thorough connecting rod mechanism. Piston reaches zero velocity at top dead center (TDC) and bottom dead center (BDC) positions, where cylinder volume is minimum and maximum, respectively. Cylinder minimum volume is known as combustion chamber volume, and the difference between minimum and maximum volumes is the piston swept volume. The ratio between maximum and minimum volumes is an important parameter for project and operation of such engines, which is called volumetric compression ration (HEYWOOD, 2018).

2.1.2 Mathematical modelling of thermal fluid dynamic processes inside ICE

Engine simulation models are valuable tools for engineers either working in the automotive industry or belonging to the research community, with the aim to design engines that comply with strict emissions legislation while keeping high performance (PARIOTIS E.G.; RAKOUPOULOS, 2012; BERNARD; LEBAS; DEMOULIN, 2011; GE et al., 2009). The classification of simulation models is subject for several authors (HEYWOOD, 1980; JAMES, 1984; RAMOS, 1989; BARROS, 2003; MELO, 2012). Some authors simplify this classification into two main categories: phenomenological models and tridimensional models based on finite volume method usually named CFD models (PARIOTIS E.G.; RAKOUPOULOS, 2012; BERNARD; LEBAS; DEMOULIN, 2011).

The main differences between those two main categories are computational cost and the level of description in the results. Phenomenological models don't solve directly the fluid flow inside the engine, this way computational time is smaller for some orders of magnitude. On the other hand, for tridimensional models based on finite volume method, or CFD models, flow of working fluids inside the engine is resolved coupled to thermodynamics, and some times to diffusion of species and chemical reactions. This category of model offers detailed results of flow field during the whole engine cycle, with a much higher computational cost (PARIOTIS E.G.; RAKOUPOULOS, 2012).

- Phenomenological models

Zero dimensional and quasi dimensional models are also known as phenomenological or thermodynamic models, once they are based on the thermodynamic analysis of engine working fluid. Zero dimensional models are written based on first law of thermodynamics, time is the only independent variable, and fuel burning rate is used from empirical and semi empirical models. Quasi dimensional models use a sub model for fuel burning rate based on turbulent combustion process, aiming to predict combustion delay and evolution. In cylinder gases are divided into two zones: burned and unburned gases. Flame front is usually considered spherical, allowing its velocity calculation. For diesel engines, those models are often used to study pollutant emissions, especially nitrogen oxide (NO_x), unburned hydrocarbons (THC) and soot formation (MELO, 2012).

- Engine CFD 3D models

Differently than phenomenological models, in multidimensional or CFD 3D models special iterative techniques are used to solve the conservation equations of mass, *momentum*, energy and species, usually coupled to a turbulence model at a discretized computational domain that covers the whole cylinder volume (PARIOTIS E.G.; RAKOUPOULOS, 2012). In the past 40 years, the development of CFD 3D models dedicated to reciprocating internal combustion engines, or Engine CFD 3D models, produced tridimensional models capable of

estimating the velocity of the flow field and combustion inside the cylinder with a fair degree of accuracy (Adapted from QI et al. 2012). Along with multidimensional models, some times phenomenological engine models can be coupled in order to calculate boundary conditions (MELO, 2012; VERSTEEG; MALALASEKERA, 2007).

2.1.3 Computational Fluid Dynamics - CFD

Computational fluid dynamics or CFD is the analysis of systems involving fluid flow, heat transfer and associated *phenomena* such as chemical reactions by means of computer-based simulation (VERSTEEG; MALALASEKERA, 2007). The technique spans a wide range of industrial and non industrial applications, among which is the analysis of thermal fluid dynamic processes taking place inside internal combustion engines. The generic sense of the expression, any fluid flow calculation using a computer is a CFD application. Although, as a consequence of the frequent use in the past 30 years, nowadays CFD is directly associated to the discrete solution of flow fields generally using finite volume method, whether the analysis has one, two or three dimensions.

The basic set of equations for applying CFD modeling to any application is composed by conservation of mass, conservation of *momentum* and conservation of energy, along with some gas model for gas flows. The direct simulation of those equations, comprises the solution of the complete flow problem, which in most cases involves vortex calculation for laminar and turbulent flows. Once that for practical reasons in terms of computational resources the complete solution of vortex is not possible, except for simple geometries and specific cases, those equations are usually resolved coupled to a turbulence model.

There are two alternatives for solving flow problems along with turbulence models. First one is to solve conservation equations for average values of flow field properties, and model the fluctuations using turbulence models, which results in smaller computational cost. Second one is to use statistic filters based in space, to limit vortex scales to be resolved directly, which increases computational cost, and model the effect of the smaller vortex using turbulence models. In this thesis, the first approach is the selected one, once it is the approach that offers the smaller computational cost available, which is compatible to the computational infrastructure which will be described in section 3.1.

The finite volume method highlights from other discretization methods for its physical bases, once it represents the numerical integration of conservation equations through each finite volume considering constant properties at each volume (VERSTEEG; MALALASEKERA, 2007). The discretization process is described in literature (VERSTEEG; MALALASEKERA, 2007) and previous work (FONSECA, 2014).

In several applications, pressure-velocity coupling is solved using pressure implicit with splitting of operators (PISO) algorithm, applied to the convergence of the discretized equations each time step. The matrix of equations is solved by the conjugate gradient method, using Cholesky algorithm as conditioner (CD-ADAPCO, 2013).

- Reynolds Averaged Navier Stokes - RANS

The conservation equations are treated in terms of average values of flow field properties, which in cases where only Navier Stokes equations are solved produces the Reynolds Averaged Navier Stokes (RANS) equations. The description of conservation equations, turbulence, Reynolds decomposition and RANS treatment is described in literature (VERSTEEG; MALALASEKERA, 2007) and previous work (FONSECA, 2014).

For engine CFD 3D modelling, conservation of energy equation is also mandatory, so the basic equations, after applying RANS treatment are Equation 2.1 through Equation 2.5:

$$\frac{\partial \overline{\rho}}{\partial t} + div(\overline{\rho}\vec{\overline{U}}) = 0 \tag{2.1}$$

$$\frac{\partial \overline{\rho}\overline{U}}{\partial t} + div(\overline{\rho}\overline{U}\vec{\overline{U}}) = -\frac{\partial \overline{P}}{\partial t} + div(\mu grad\overline{U}) + \Big[-\frac{\partial(\overline{\bar{\rho}u'^2})}{\partial x} - \frac{\partial(\overline{\bar{\rho}u'v'})}{\partial y} - \frac{\partial(\overline{\bar{\rho}u'w'})}{\partial z} \Big] + S_{M_x} \tag{2.2}$$

$$\frac{\partial \overline{\rho}\overline{V}}{\partial t} + div(\overline{\rho}\overline{V}\vec{\overline{U}}) = -\frac{\partial \overline{P}}{\partial t} + div(\mu grad\overline{V}) + \Big[-\frac{\partial(\overline{\bar{\rho}u'v'})}{\partial x} - \frac{\partial(\overline{\bar{\rho}v'^2})}{\partial y} - \frac{\partial(\overline{\bar{\rho}v'w'})}{\partial z} \Big] + S_{M_y} \tag{2.3}$$

$$\frac{\partial \overline{\rho}\overline{W}}{\partial t} + div(\overline{\rho}\overline{W}\vec{\overline{U}}) = -\frac{\partial \overline{P}}{\partial t} + div(\mu grad\overline{W}) + \Big[-\frac{\partial(\overline{\bar{\rho}u'w'})}{\partial x} - \frac{\partial(\overline{\bar{\rho}v'w'})}{\partial y} - \frac{\partial(\overline{\bar{\rho}w'^2})}{\partial z} \Big] + S_{M_z} \tag{2.4}$$

$$\frac{\partial \overline{\rho}\overline{I}}{\partial t} + div(\overline{\rho}\overline{I}\vec{\overline{U}}) = -\overline{P}div(\vec{\overline{U}}) + div(\Gamma grad\overline{T}) + \Big[-\frac{\partial(\overline{\bar{\rho}u'i'})}{\partial x} - \frac{\partial(\overline{\bar{\rho}v'i'})}{\partial y} - \frac{\partial(\overline{\bar{\rho}w'i'})}{\partial z} \Big] + \Phi + S_I \tag{2.5}$$

For Equation 2.1 through Equation 2.5, the average field variables are $\overline{\rho}$ for average density, $\overline{P}$ for average pressure, $\vec{\overline{U}}$ for average velocity vector, $\overline{U}$, $\overline{V}$, $\overline{W}$ for average velocity components, $\overline{I}$ for average total internal energy, $\overline{T}$ for average temperature.

- RNG k-ε

Fluid flow turbulence is accounted for by means of the ReNormalization Group (RNG) closure for the two-equation $k-\varepsilon$ model (PERINI; MILES; REITZ, 2014; HAN; REITZ, 1995). For sake of brevity, the description of turbulent viscosity models, $k-\varepsilon$ family models and RNG $k-\varepsilon$ model are omitted, and can be found in literature (VERSTEEG; MALALASEKERA, 2007; YAKHOT et al., 1992; YAKHOT; ORSZAG, 1986) and previous work (FONSECA, 2014). This model includes two conservation equations for turbulent kinetic energy k and dissipation of turbulent kinetic energy ε (CD-ADAPCO, 2013):

$$\frac{\partial \overline{\rho}k}{\partial t} + div(\overline{\rho}k\vec{\overline{U}}) = div\Big((\mu + \frac{\mu_t}{\sigma_k})grad(k)\Big) + \mu_t(P + P_B) - \overline{\rho}\varepsilon - \frac{2}{3}\tau_{ij}S_{ij} \tag{2.6}$$

$$\frac{\partial \overline{\rho}\varepsilon}{\partial t} + div(\overline{\rho}\varepsilon\vec{U}) = div\Big((\mu + \frac{\mu_t}{\sigma_\varepsilon})grad(\varepsilon)\Big) + C\varepsilon 1\frac{\varepsilon}{k}(\mu_t P - \frac{2}{3}\tau_{ij}S_{ij}) - C_{\varepsilon 2}\overline{\rho}\frac{\varepsilon_2}{k} + C_{\varepsilon 3}\frac{\varepsilon}{k}\mu_t P_B + C_{\varepsilon 4}\overline{\rho}\varepsilon S_{ij} - \frac{C_\mu \eta^3(1-\frac{\eta}{\eta_0})}{1+\beta\eta^3}\frac{\overline{\rho}\varepsilon^2}{k} \quad (2.7)$$

2.2 ENGINE CFD 3D MODEL

Computational fluid dynamics technique can be used to analyze several *phenomena* for industrial or academic application. In the case of reciprocating internal combustion engine, few computer programs have been developed specifically to deal with inherently complex physics associated to this kind of engine. Valves opening and closing are particularly hard to describe in a common CFD code. For some analysis intervals, intake and exhaust ports are simply unnecessary, and it would be better if they were not there. For others, the same regions are essential for correct flow field calculation. Another example is piston movement, which cannot be describe simply by mesh deformation, once grid volumes would be to stressed in bottom dead center and to compressed in top dead center.

Among other options, STAR-CD commercial code, which nowadays is property of SIEMENS, is one of the most traditional commercial codes for engine CFD 3D modelling (MILLO et al., 2014; BARATTA; RAPETTO, 2014; BAUMANN; MARE; JANICKA, 2014; BERNI; CICALESE; FONTANESI, 2017; MANDANIS et al., 2018) . The complete description of STAR-CD methodology can be found in the program manuals, and only the mesh generation procedure will be briefly described here. Most of the grid generation process can be resumed in Figure 2.1, where four steps are described: 2D template, 3D template, cut parts and assembled model for reference grid.

Figure 2.1 – Grid generation process at ES-ICE module.

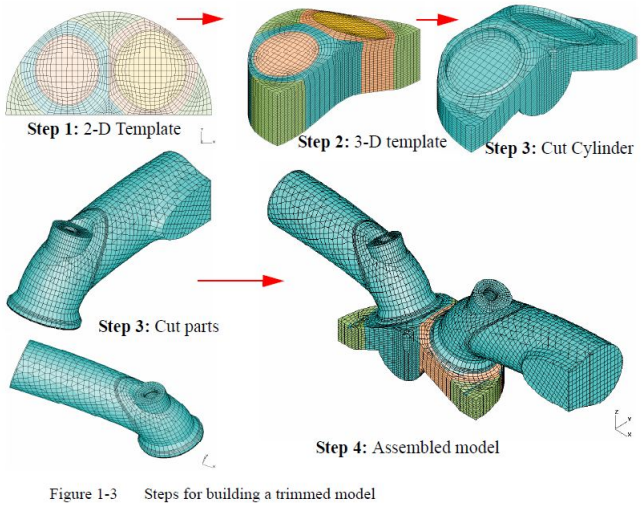

Figure 1-3 Steps for building a trimmed model

SOURCE: (CD-ADAPCO, 2013)

The first step is the generation of a 2D grid template, based on piston, combustion chamber and valves relative geometry. Second step is the generation of a 3D grid template,

which is more dedicated to the combustion chamber geometry. The steps 3 and 4 in Figure 2.1 can be grouped in one step, which is the generation of the reference grid, named assembled model. Based on this reference grid, the program calculates a grid database for a selected number of cycle instants. The interval for grid generation can be defined, and is used as 5 crank angle degrees as a best practice.

2.2.1 Near wall flow and heat transfer models

Several mathematical formulations have been proposed aiming at estimate reliably near wall flow and heat transfer through the combustion chamber, intake and exhaust ducts (plenum, runner, port) walls. The first models were developed for nearly isothermal flows, starting from the evidence that turbulent flows exhibit universal velocity and temperature near-wall profiles if wall distance, velocity and temperature are properly scaled, which is similar to phenomenological heat transfer models. After some research, it has been realized that a reliable estimation of the heat fluxes by means of CFD 3D calculations cannot be considered isothermal at all as near-wall gas temperatures are relevantly higher than wall temperatures during compression and combustion (BERNI; CICALESE; FONTANESI, 2017; NIJEWEME et al., 2001).

This is the reason why several authors decided to propose wall heat transfer models able to account for variations of density and even variations of all other gas properties with temperature. Among other variable density models two of the most diffused are the Angelberger et al. (ANGELBERGER; POINSOT; DELHAY, 1997) and the Han and Reitz (HAN; REITZ, 1997) ones. A deepening on these models can be found in (BERNI; CICALESE; FONTANESI, 2017).

More recently, several authors proposed near wall models for RANS approach (BERNI; CICALESE; FONTANESI, 2017) and LES approach (ŠARIĆ; BASARA; ŽUNIČ, 2017; MA et al., 2017). The models proposed for LES approach are beyond the objectives of this thesis, and the one proposed by (BERNI; CICALESE; FONTANESI, 2017) is dedicated to high performance turbocharged engine, which is far from the single cylinder naturally aspired engine used in this thesis. This way, the best formulation for RANS approach considered for this thesis is still the one proposed by Angelberger et al. (ANGELBERGER; POINSOT; DELHAY, 1997).

2.2.2 ECFM-3Z for engine combustion

In the extended coherent flame model - 3 zones (ECFM-3Z), the state of the gases mixture is defined by variables Z and c, where Z is the mixture fraction variable and c is the reaction progress variable. It is simultaneously described in terms of mixing and progress of reaction as schematically represented in Figure 2.2

According to Figure 2.2, each cell of the grid is divided into three mixture zones:

Figure 2.2 – Schematic of ECFM-3Z model.

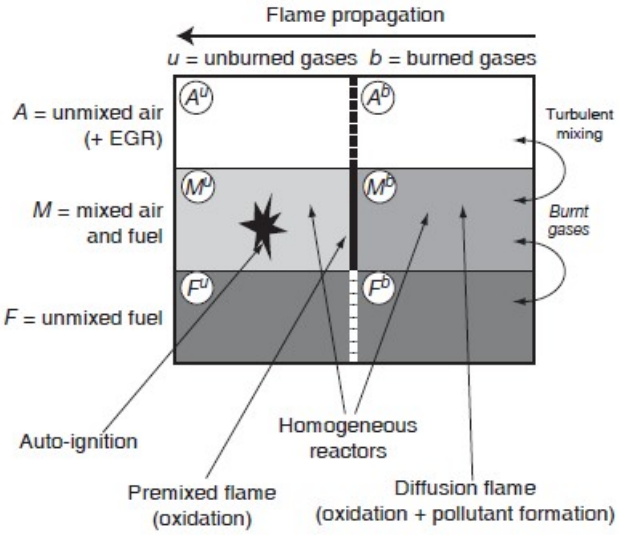

SOURCE: (COLIN; BENKENIDA, 2004)

unburned fuel zone (F), mixture region which contains air, fuel and EGR (M) and unmixed air plus EGR (A). This scheme is represented by the probability density function (PDF) of mixture variable Z through a three delta distribution:

$$P(Z) = a\delta(Z) + b\delta(Z - \overline{Z}^{M}) + c\delta(Z - 1) \tag{2.8}$$

Where $\overline{Z}^{M}$ is the average value of mixture fraction into mixture region. First delta function corresponds to unmixed air region A, second delta function represents mixture region M and third function corresponds to unmixed fuel region F. Taking into accout that combustion cannot happen into regions A and F, combustion just happens into region M, and is defined by ECFM model equations (COLIN; BENKENIDA; ANGELBERGER, 2003). The complete description of combustion representation by ECFM-3Z is available in literature (COLIN; BENKENIDA; ANGELBERGER, 2003; COLIN; BENKENIDA, 2004).

- Flame surface density

The model ECFM-3Z has been proposed by Colin and Benkenida (2004) as an extension of coherent flame model (CFM) (DUCLOS; ZOLVER; BARITAUD, 1999). The coherent flame model has its main characteristic on the definition of a flow field property Σ, which is the flame surface density, which helps the calculation of flame front propagation. Property Σ is defined by

$$\Sigma = \frac{\delta A}{\delta V} \tag{2.9}$$

Where A is flame surface area [m^2] and V is the volume enclosed by flame surface [m^3]. The authors proposed Equation 2.10 as conservation equation for Σ inside each cell of the grid

(COLIN; BENKENIDA; ANGELBERGER, 2003):

$$\frac{\partial \Sigma}{\partial t} + \frac{\partial u_i \Sigma}{\partial x_i} = \frac{\partial}{\partial x_i}\left(\frac{\mu_t}{Sc_t} + \frac{\mu}{Sc}\right)\frac{\partial(\Sigma/\overline{\rho})}{\partial x_i} + (P_1 + P_2 + P_3)\Sigma - D + P_k \tag{2.10}$$

Where (COLIN; BENKENIDA; ANGELBERGER, 2003):

- $P_1 = \alpha K_t$ represents the flame surface production by turbulent stretch, where K_t is the ITNFS stretch (MENEVEAU; POINSOT, 1991) and $\alpha = 1.6$ is a model constant;
- $P_2 = \frac{\partial ui}{\partial x_i}$ quantifies the production by means of flow dilatation;
- $P_3 = \frac{2}{3}\overline{s}_l \frac{1-c}{c}\Sigma$ models the effects of flame thermal expansion and curvature;
- $D = \beta \overline{s}_l \frac{\Sigma^2}{1-\tilde{c}}$ is a destruction term due to consumption, where $\beta = 1$ is a model constant;
- P_k is a source term applied during the ignition period by the spark plug.

It should be highlighted from Equation 2.10 that there are semi empirical constants involving the use of this model. The program STAR-CD implements this equation with two adjustment parameters: α and β. As it is mentioned by (COLIN; BENKENIDA; ANGELBERGER, 2003), the values proposed by the authors are $\alpha = 1.6$ and $\beta = 1$.

2.2.3 Fuel injection models

Fuel injection inside the simulation domain is represented through introduction of droplet packages, which movement depends on the injection pressure and relative position. This way it is possible to represent complete simulation of injection *phenomena* and obtain similar effects, thus reducing computational cost. Figure 2.3 illustrates the break-up diagram of a hollow cone jet, where the most important *phenomena* involved in the fuel injection process are represented. Full description of fuel injection physics and modelling is available in literature (BAUMGARTEN, 2006).

- Primary break-up

There are only very few detailed models for the simulation of primary break-up of high-pressure sprays. One reason is that the experimental investigation is extremely complicated because of the dense spray and the small dimensions (BAUMGARTEN, 2006). One solution is to use distribution functions, which method assumes that the fuel is already fully atomized at the nozzle exit and that the distribution of drop sizes can be described by mathematical or statistical functions (BAUMGARTEN, 2006).

For hollow-cone sprays with pressure-swirl atomizers, the investigations of (HAN et al., 1997) have shown that the measured droplet sizes are better represented by the Rosin-Ramler

Figure 2.3 – Hollow-cone spray break-up diagram.

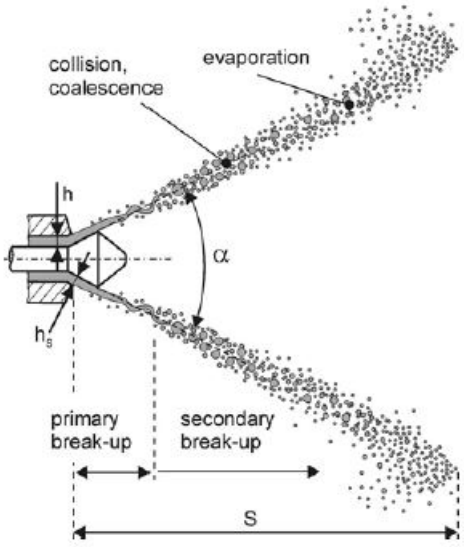

SOURCE: (BAUMGARTEN, 2006).

distribution (BAUMGARTEN, 2006). The distribution of Rosin-Rammler is calculated using Equation 2.11 (CD-ADAPCO, 2013):

$$Q = 1 - exp\left[-\left(\frac{D}{X}\right)^{q}\right] \tag{2.11}$$

Where Q is the fraction of the total volume occupied by droplets of diameter smaller than D, and also the quantities X and q are empirical constants (CD-ADAPCO, 2013).

- Secondary break-up

Among other secondary break-up models, the models of Kelvin-Helmholtz (KH) proposed by (REITZ et al., 1987), and the Rayleigh-Taylor, proposed by (TAYLOR, 1950), are highlighted. It is common nowadays engine CFD 3D programs use combined secondary break-up models, in order to obtain better accuracy for practical applications, therefore the use of KH and RT models coupled is of common practice as a single model, KH-RT.

In the case of the KH-RT model, both models are implemented in CFD codes in a competing manner. Both models are allowed to grow unstable waves simultaneously, and if the RT-model predicts a break-up within the actual time step, the disintegration of the whole drop according to the RT mechanism occurs. Otherwise the KH model will produce small child droplets and reduce the diameter of the parent drop (BAUMGARTEN, 2006).

The complete description of the model is available in literature (BAUMGARTEN, 2006; CD-ADAPCO, 2013), and the model empirical constants are B_0 with a default value of 0.61, B_1 with a default value of 40.0, C_3 with a default value of 0.1, and C_τ with a default value of 1.0 (CD-ADAPCO, 2013).

- Coalescence and collision

The collision models used in CFD codes usually do not take all the different collision phenomena into account. One of the reasons for the use of more simple models in engine simulations is that a direct evaluation of a collision model by comparison with experimental data is not possible. The relevant spray parameters like droplet sizes and velocity components for example are always a result of many phenomena like break-up, evaporation, and collision, and it is impossible to quantify the single effects from measurements (BAUMGARTEN, 2006). This way, coalescence and collision models are not used in this work.

- Evaporation and drag

In the simulation program used, the coefficients of drag, heat transfer and mass transfer are functions of the small-scale flow features around the individual droplets, and these features are impractical to resolve spatially when there are more than just a few droplets. This way, semi empirical correlations are implemented in order to reduce computational cost. For the drag coefficient, Equation 2.12 is used (CD-ADAPCO, 2013):

$$C_d = \begin{cases} \frac{24(1+0.15Re_d^{0.687})}{Re_d} & , \quad Re_d \leq 10^3 \\ 0.44 & , \quad Re_d > 10^3 \end{cases} \tag{2.12}$$

Where Re_d is the droplet Reynolds number (CD-ADAPCO, 2013). For the heat transfer coefficient $h_{droplet}$, the El Walkil correlation, Equation 2.13, is used (CD-ADAPCO, 2013; WAKIL; UYEHARA; MYERS, 1954):

$$h_{droplet} = \frac{k_m NuZ}{(e^Z - 1)D_d} \tag{2.13}$$

Where Nu is the Nusselt number given by the Ranz-Marshal correlation in Equation 2.14 (CD-ADAPCO, 2013; RANZ; MARSHALL et al., 1952):

$$Nu = 2(1 + 0.3Re_d^{1/2}Pr^{1/3}) \tag{2.14}$$

- Droplet wall interaction

The interaction between spray and wall is usually described in literature as spray wall impingement, as an important process associated to wall spray development and wall film evolution, in such a manner that both processes may strongly influence combustion efficiency and the formation fo pollutants (BAUMGARTEN, 2006). The complete description of the spray wall impingement is out of the scope of this thesis, and for this purpose there is literature available (BAUMGARTEN, 2006) and commercial program manuals (CD-ADAPCO, 2013).

2.3 ICE INTAKE MANIFOLD PULSATING FLOW

The intake manifold is a system designed to deliver air to the engine through ducts connected to each cylinder (SOUZA et al., 2019). The length, diameter and internal surface

finish of the intake tubes directly influence the mixing result and of course, the power (HANRIOT; QUEIROZ; MAIA, 2019). The lengths of these ducts, and to a certain extent their diameters, must be chosen carefully as they will determine the resonant frequencies of the manifold (SOUZA et al., 2019; JEMNI; KANTCHEV; ABID, 2011).

Considering the intake ducts (manifold, runner, port), important design criteria are: low air flow resistance; good distribution of air and fuel between cylinders; runner and port lengths that take advantage of ram and tuning effects (CEVIZ, 2007). The application of geometric modifications to the intake manifold to improve engine breathing has provided positive results using different strategies, such as varying the intake plenum length or adding a Helmholtz resonator (HANRIOT; QUEIROZ; MAIA, 2019).

The pressure in intake manifold varies during each cylinder intake process due to the piston velocity variations, valve open area variations, and the unsteady gas flow effects that result from these geometric variations. The mass of air inducted into the cylinder, and hence the volumetric efficiency, is almost entirely determined by the pressure level in the intake port during the short period before intake valve is closed (CEVIZ, 2007).

Based on the above discussion, it can be stated that should no change or optimization be implemented to the intake manifold geometry, the effect of pulsating flow would be a reduction at volumetric efficiency. This effect would be observed for all of the engine operating conditions different to the one for which the intake system is designed or optimized. The reduction in volumetric efficiency for all of the operating conditions different to the optimized one can be expressed as a reduction in the trapped mass of air per cycle.

The great majority of the models proposed to capture the effects of pulsating flow at intake air mass flow and in cylinder trapped mass of air are zero dimensional or one dimensional (HANRIOT; QUEIROZ; MAIA, 2019; SOUZA et al., 2019; SILVA; OCHOA; HENRÍQUEZ, 2019; MEZHER et al., 2013). Almost all of those zero dimensional or one dimensional models consider that the pressure variations generated by the pulsating flow can be used to improve the intake pressure level, by configuring the intake manifold in order to optimize the pressure pulses in the intake system(CEVIZ, 2007).

Several engine CFD 3D simulations have been performed for intake manifolds, including DNS simulations, but none of them consider the effects of intake pulsating flow at in cylinder trapped mass of air (GIANNAKOPOULOS et al., 2017; WANG et al., 2015; MILLO et al., 2014; BAUMANN; MARE; JANICKA, 2014; SAKOWITZ; MIHAESCU; FUCHS, 2014; QI et al., 2012; JEMNI; KANTCHEV; ABID, 2011).

2.4 ENGINE HEAT TRANSFER MODELLING

Research on in-cylinder heat transfer of internal combustion engines has been conducted since 1923 (BORMAN; NISHIWAKI, 1987), in order to optimize engine design, due to the significant impact of heat transfer on engine's efficiency, power and emissions (BROEKAERT

et al., 2016b; DENG et al., 2013; YAMAKAWA et al., 2012). Prediction of heat transfer plays an important role in engine development as heat losses influence overall engine efficiency, exhaust emissions and component thermal stresses (ŠARIĆ; BASARA; ŽUNIČ, 2017). By modeling engine heat transfer, design changes can be readily assessed with minimal prototype construction and testing. This enables new engines to be designed more rapidly, cost effectively, and with improved thermal signatures (BOHAC; BAKER; ASSANIS, 1996).

Reviews about engine heat transfer have been published in order to organize the knowledge on this research and development area (BORMAN; NISHIWAKI, 1987; FINOL; ROBINSON, 2006), and in depth reviews were conducted in Ph.D. thesis (PIEDRAHITA, 2009). The organization in a literature review paper of the state of the art on actual engine heat transfer modelling is a product of this thesis (FONSECA et al., 2019).

The models published in literature for estimation/calculation of engine heat transfer and wall temperature can be organized in three heat transfer modelling approaches: gas to wall heat transfer, wall to wall heat transfer and wall to liquid heat transfer. The combination of gas to wall, wall to wall and wall to liquid approaches is required to estimate/calculate engine internal wall surface temperature, inside the cylinder, ports and ducts, and specially for valves and piston. For any kind of engine, using those approaches means working with convection-conduction problems, although in diesel engines, it can involve radiation in some cases (very sooting flames).

- Gas to wall heat transfer;

Gas to wall heat transfer is the modelling approach for the heat exchange between gases and walls in cylinder, intake and exhaust engine regions. Most of the papers in literature addressing heat transfer inside internal combustion engines refers exclusively to this heat transfer approach. The previous literature review deals with the major part of those models before 2009 (BORMAN; NISHIWAKI, 1987; FINOL; ROBINSON, 2006; PIEDRAHITA, 2009). The near wall temperature models are included in this heat transfer approach.

- Wall to wall heat transfer;

Wall to wall heat transfer approaches are those used to calculate heat fluxes inside engine parts (head, piston, valves, block, etc.). Three approaches are included in this group:

1. Global heat transfer models, which solves one dimensional phenomenological equations in order to calculate one single value for each surface under analysis;

2. Nodal heat transfer models, which splits each engine part into few number nodes, and solves the heat transfer between the nodes and from the nodes to their boundaries in two or three dimensions;

3. Finite element models, which splits each engine part into large amount of nodes, and solves the discrete form of energy diffusion equation, generally in three dimensions.

- Wall to liquid heat transfer.

The third modelling approach is dedicated to calculate heat flux to coolant and lubricating oil. Several are the publications dedicated to this heat transfer approach. Some examples for heat transfer to the coolant are (TORREGROSA et al., 2014; MEHDIPOUR; BANIAMERIAN; DELAURÉ, 2016), and for heat transfer to the oil is (LIU et al., 2014).

- Conjugate heat transfer (CHT)

More recently, several authors have turned their attention to the importance of wall temperature boundary conditions at engine CFD 3D models, and the interaction between reactive flow field and wall heat transfer. The coupled solution for the reactive flow field and solid heat transfer has been called conjugate heat tranfer (CHT) analysis (BROATCH et al., 2019; MANDANIS et al., 2018; ZHANG, 2018; BERNI; CICALESE; FONTANESI, 2017; SCHMITT et al., 2016b; MEHDIPOUR; BANIAMERIAN; DELAURÉ, 2016; MISDARIIS; VERMOREL; POINSOT, 2015; KIKUSATO; KUSAKA; DAISHO, 2015).

The conjugate heat transfer modeling is an extension of heat transfer calculation into the solid components of a thermal device and is achieved through the solution of energy equation for the solid phase simultaneously with that for the fluid phase (ZHANG, 2018).

Despite the improvement of overall simulation performance, a 30% increase in computational load was induced by the CHT modeling, compared to a regular simulation of fluid-phase dynamics. Hence, methods to reduce the computer time are always of interest for engine simulation that involves application of advanced sub-models (ZHANG, 2018; LI; KONG, 2011).

2.5 STATE OF THE ART

In this section, it is presented a brief resume of the most relevant publications from the last five years (since 2014) related to the main topics of this thesis, which are: engine CFD 3D modelling, ICE intake manifold pulsating flow modelling, engine heat transfer modelling and conjugate heat transfer at engine CFD 3D models.

Based on this resume, it is presented the contribution proposed in this thesis to the knowledge of engine CFD 3D simulation, in terms of limitations of the RANS approach concerning intake pulsating flow, treatment of intake pressure boundary conditions, use of zero dimensional heat transfer models for CHT analysis, and most important, systematic calculation of accurate results by means of engine CFD 3D modelling with the proposed methodology, without tuning any of the sub models constants.

The state of the art is organized as follows:

- Articles related to engine CFD 3D modelling
- Articles related to ICE intake manifold flow and pulsating flow modelling
- Articles related to engine heat transfer modelling
- Articles related to conjugate heat transfer at engine CFD 3D models
- Articles related to verification and validation of CFD models

2.5.1 Articles related to engine CFD 3D modelling

(BAUMANN; MARE; JANICKA, 2014) used an engine CFD 3D model with LES approach for turbulence, performed at STAR-CD commercial program, to build numerical analysis of the variable results compared to experimental PIV measurements, aiming at validation of LES simulation of internal combustion engines. The authors modeled a single cylinder research engine operating at motoring conditions, and performed an adjustment at intake pressure, based on Bernoulli's equation, in order to correctly predict the measured in cylinder mass of air. The authors explain the difference in trapped mass of air inside the cylinder by means of geometrical details and albeit minimal approximations. The results are presented for in cylinder velocity flow fields, velocity line distributions, velocity gradient tensor associated variables and turbulence resolution index. The authors conclude that LES results are in excellent agreement with experimental results, which means only qualitative validation is performed.

(MILLO et al., 2014) presented the project, analysis using a CFD 3D program, and the test of modified cylinder head in a turbocharged SI engine fuelled with gasoline. The engine CFD 3D model was used to evaluate the in cylinder charge motion of the projected head, in terms of turbulent kinetic energy and turbulent intensity, and compare with similar characteristics obtained for baseline head. The authors used commercial software STAR-CD, to simulate a model that included intake and exhaust ports, but used half of the combustion chamber geometry, based in geometric symmetry from piston, intake and exhaust ports. The authors used standard $k-\varepsilon$ model for turbulence, commercial software GT-POWER to provide boundary conditions in terms of temperature and pressure at intake and exhaust ports, and a grid of approximately 1.5 million cells at bottom dead center with a cell grid size of approximately 1.5 mm. The authors conclude that, at low loads, the proposed geometry increase the turbulent intensity inside the cylinder, and the performance of the engine is considerably increased.

(BARATTA; RAPETTO, 2014) presented an analysis using engine CFD 3D model about simulation of compressed natural gas injection inside internal combustion engines, along with 2D CFD simulation of supersonic under expanded free jet issuing form a nozzle study. The objective of the 2D CFD analysis specific for the jet is to study the best form of representing the flow field and shock wave coming from the fuel jet inside the CFD 3D

domain. The authors performed the engine CFD 3D analysis using STAR CD commercial program with standard $k-\varepsilon$ for turbulence, using two separated grids: one specific for the gaseous fuel injection region, another one for the rest of the domain including cylinder, intake and exhaust ports. The authors conclude that the model is capable of representing engine cycle and fuel mixture formation for an compressed natural gas engine, but for that a minimum resolution of 40 cells is necessary for the region close to the gas injector outlet.

(PERINI; MILES; REITZ, 2014) used a comprehensive computational model of a high swirl, light duty optical diesel engine, to present a description of the engine fluid flow properties. The model performed at KIVA engine CFD 3D software, using $RNGk-\varepsilon$ for turbulence approach and a chemical kinetics code for combustion, is used at a four valve cylinder considering intake and exhaust ducts. The authors conclude that RANS turbulence modeling is suitable for computational modeling of cycle averaged experimental measurements, and no noticeable differences in the flow field characteristics were seen for multicycle simulations.

(KHALILARYA; NEMATI et al., 2014) performed CFD 3D simulation of the closed cycle of a supercharged four valve, four stroke spark ignition engine, fueled with gasoline, ethanol, methanol and hydrogen, to evaluate the influence of EGR. The geometry of the simulation domain is only the combustion chamber, once only closed valve period is simulated, which is modeled using $RNGk-\varepsilon$ for turbulence, and coherent flame model for combustion.The results for six different fuels are compared to experimental data for in cylinder pressure, using different amount of EGR for each fuel. The authors conclude that increasing EGR ratio causes a decline in the indicated mean effective pressure due to lower flame speed.

(LINSE; KLEEMANN; HASSE, 2014) proposed a model to predict knock in engine CFD 3D models within the limits of RANS turbulence approach, using a probability density function coupled with chemical kinetics. The authors derived transport equations specific for an ignition progress variable, and used it along with presumed PDF approach for the chemical source term closure at the engine CFD 3D program ANSYS CFX. The authors used a half symmetry geometry of one cylinder from a 3.0 L six cylinder spark ignition engine fueled with gasoline, with fixed wall temperature boundary conditions calculated by several iterative simulations of in cylinder flow, structure and coolant simulations, although heat transfer models are not described. The results for several engine CFD 3D cycles are presented, with different in cylinder pressure histories, and evaluated for the percentile occurrence of knocking. The authors conclude that regions with high probability to auto ignite were clearly identified by the applied knock model.

(CLENCI et al., 2014) presented the evaluation of the gas exchange *phenomena* and internal aerodynamics of a port fuel injection engine using low intake valve lift. The authors performed a CFD 3D dynamic simulation of the engine operating in motoring condition. They used referenced experimental results measured at the modeled engine as boundary conditions for performing the simulations, and validating the simulation. The engine CFD 3D model was

developed at ANSYS-Fluent, aiming at providing quantitative information about the engine's internal aerodynamics for maximum and minimum lift. The authors used a 1.23 milling elements grid at top dead center and 1.58 million element grid at bottom dead center, and did not refined the mesh for the computational cost of the simulation. The boundary conditions used are imposed pressure values at intake and exhaust boundary surfaces, and the wall of the engine are considered adiabatic, once the engine operates at motoring condition. The time step used was $0.5\,\mathrm{deg}\,CA$, and the pressure velocity coupling was resolved using the PISO algorithm. A second order discretization scheme was used for the moment and turbulence conservation equation, along with realizable $k-\varepsilon$ model. After presenting a qualitative validation, the authors present the comparison of the CFD 3D model results for two conditions: maximum and minimum valve lift, and based on those results the authors conclude that the variable valve lift has the potential to increase turbulence parameters of in cylinder flows.

(ROBERT et al., 2015) present an engine CFD 3D model for predicting knock tendency in a spark ignition internal combustion engine fueled with iso octane. The model proposed by the authors uses LES approach for turbulence, and a modified version of ECFM model specific for LES calculations, along with some modifications to take into account flame front development and auto ignition simultaneously. The authors presents comparison between numerical and experimental results IMEP, COV of IMEP and in cylinder pressure trace during combustion analysis period for one specific engine operating condition, which is 1800 rpm and 19 bar. The main argument for considering the proposed model a valid one is the comparison between IMEP and COV of IMEP, although no information about $U_{95\%}$ is informed for both experiment or model. After performing this validation, the authors use the models 3D results to estimate the most important knocking spots. The authors conclude that for the evaluated operating point, knock occurs for fast burning cycles, and that auto ignition spots are random but occur essentially below exhaust valve.

(WANG et al., 2015) performed cycle variation analysis using engine CFD 3D model with LES approach to capture instantaneous in cylinder turbulent structures in a DISI engine equipped with a tumble control valve at intake duct. The authors used proper orthogonal decomposition to evaluate in cylinder flow field variables at cold flow conditions. The results are presented for several variables of flow field, considering average velocities, local velocities, tumble coefficients, and including in cylinder mass. Although, no result is presented for volumetric efficiency, and no combustion case is presented. The authors conclude that the closed tumble flap leads to higher tumble ratio, with lower amplitude of fluctuation compared with open tumble flap.

(TOOSI; FAROKHI; MASHADI, 2015) used KIVA-3V software to perform engine CFD 3D simulations in a spark ignition engine fueled with gasoline. The authors developed a modified eddy dissipation concept at a static burner, and applied the proposed model at the engine CFD 3D simulation. The results are compared to a RANS simulation performed at the same engine. The authors conclude that the best values for eddy dissipation model constants

are obtained by adjustment for one of the results.

(HASSE, 2016) presented an in depth state of the art review concerning scale resolving simulations, such as large eddy simulations(LES), and their application to engine development industrial applications. The author presents the discussion concerning several applications of LES presented in literature 5 years before the articles publication, although several papers from early LES engine applications are also presented. One of the main conclusions of the author is that in the until 2020, the university engine CFD 3D applications would be mainly based on LES models, and that industry would also evolve in order to start using this approach for engine development.

(BUHL et al., 2017) presented a comparative study between different LES and hybrid LES/RANS turbulence models applied for a simplified geometry of a two stroke internal combustion engine operating at 200 rpm, considered by the authors an ICE benchmark case. The authors focus in the description of the turbulence models comparing LES and hybrid LES/RANS, once the geometry and boundary conditions are used from literature, along with previous DNS and LES results. Velocity and turbulence results from the flow field are compared between five different turbulence models, for different instants of the engine cycle. The authors conclude that, for the averaged velocity and resolved velocity fluctuations, all of the models shows good agreement.

(FAN et al., 2018) presented numerical investigation of boundary layer flow and wall heat transfer in a gasoline direct injection engine, operating in motoring condition at low engine speed. The authors used commercial code ANSYS FLUENT to simulate 32 consecutive engine cycles using a hybrid approach between RANS and LES for turbulence, for having higher precision than wall function with less computational cost than LES. Wall temperature boundary conditions are constant wall temperature below 400 K, once the engine is operating at motoring condition. The model results are compared to experimental measurements using particle image velocimetry. The comparison between engine CFD model and PIV measurements shows good agreement for velocity fields and near wall flow. The authors don't perform validation, and present results for one specific engine speed.

(MASOULEH et al., 2018) presented an in depth analysis of cycle to cycle variation using engine CFD 3D model with a hybrid LES/RANS turbulence approach of a simplified engine geometry, in terms of flow and thermal fields. The hybrid turbulence approach uses LES for calculating the turbulent core of the flow, while a wall model for RANS approach is used for the near wall flow, and the velocity fluctuations are calculated by consideration of isotropic turbulence. The geometry of the model is a simplified engine geometry, without considering intake ducts and also without considering spark plug, so the spark in included into the domain as an spherical kernel with given energy and dimension values. The results are compared to literature values for obtained using DNS and LES approaches. The authors concluded that both flow and temperature fields contributed to cycle to cycle variations, with the flow field providing dominant contribution.

2.5.2 Articles related to ICE intake manifold flow and pulsating flow modelling

(SAKOWITZ; MIHAESCU; FUCHS, 2014) implemented two methods for flow decomposition methods to the analysis of a CFD 3D model concerning the intake manifold of a six cylinder diesel engine, specifically proper orthogonal decomposition and dynamical mode decomposition. The authors implemented a CFD 3D simulation of the intake manifold using LES approach for turbulence, considering two types of inlet, namely fresh air and exhaust gas recirculation, and twelve outlet surfaces, being two outlets at each cylinder. The boundary conditions used are measured pressure at inlet surfaces, and calculated mass flow at outlets, being the calculated mass flow obtained by means of one dimensional model, although neither the experimental apparatus or the one dimensional model are described. The results obtained by the authors showed that the pulsating flow dominates the intake manifold, being the main frequencies at 30 and 60 Hz, which are attributed by the authors to the inlet of exhaust gas recirculation and outlet flow, respectively.

(GIANNAKOPOULOS et al., 2017) presented an in depth analysis of turbulent flow vortex at intake pipe of an internal combustion engine by means of direct numerical simulation. The authors considered the domain as the intake runner of the TCC-III engine (SCHIFFMANN et al., 2016), which is a circular cross section 90◦ elbow with a diameter $D = 25.4mm$ and center line radius of $R_c = 60mm$, including the valve body at an static at half way position. In this small domain, the authors performed DNS simulation with a grid containing around 207 million cells, with a main objective of representing the valve discharge coefficient experimental test by the simulation flow. The boundary conditions are intake velocity profile at runner intake and pressure outlet at valve curtain. The authors present several results for flow vortex at the domain, the behaviour of the observed vortex at space for two different Reynolds number, and also considering Dean number, which is an special form of Reynolds number for curved pipes.

(HANRIOT; QUEIROZ; MAIA, 2019) performed experimental and numerical studies on the acoustics of the intake manifold, in order to develop a complex expression to determine the natural frequency of the intake manifold, and thus improve intake mass air flow of the engine using of a Helmholtz resonator. The authors used a facility designed to perform experiments of the flow conditions at intake and exhaust systems of cylinder head considering only the waves that propagate into intake/exhaust systems, in steady state and transient regimes, with measurement of mass flow, pressure, temperature and engine speed. A mathematical 0D model is proposed to calculate the resonant frequencies of the system, using an equivalent circuit representation for the intake system with the Helmholtz resonator, considering the acoustic impedance of the ducts and the resonator. The results for mass flow rate show that the average mass flow rate for all cases was increased for all cases when Helmholtz resonator was present. The authors conclude that the best conditions was achieved when the resonator was tuned to the natural frequency of the static test bench.

(SOUZA et al., 2019) used GT-Power 1D commercial software, along with experimental results, to model a four stroke four cylinder spark ignition engine operating at

motoring conditions, in order to investigate the effects of different intake manifolds geometries over the engine volumetric efficiency. The experimental apparatus consists of a four cylinder 2.0 L engine operating at motoring conditions, with a hot wire mass flow meter corrected by a temperature sensor installed at an equalization tank after the exhaust manifold, for which an accuracy greater than 3% is stated by the authors. The authors performed the validation of the 1D model by means of qualitative comparison of pressure traces at intake manifold, calculated by the model and measured by the experiment for 2500 rpm. The comparison is performed at four different intake manifold geometries, and the authors consider the model validated for the good agreement observed in the comparison charts. The model was then used to perform 1D combustion simulation of the evaluated engine fueled with ethanol at several operating conditions. The authors conclude that the numerical simulation was considered satisfactory.

2.5.3 Articles related to ICE heat transfer modelling

(LIU et al., 2014) performed a series of laboratory experiments on oil jet cooling of reciprocating engine pistons, and proposed an area average correlation for heat transfer correlated to oil jet impingement. The authors reviewed the available correlations for piston cooling, and the ones for liquid jet impingement heat transfer on generic surface geometries. The experimental apparatus is a static test bench where a jet of heated oil is used to cool an engine piston in an insulated piston test section, where electrical resistances provide heat to the piston. The insulation guarantees that the only way for cooling the piston is the oil jet. The authors present results for the heat transfer coefficient at different oil flow speed conditions, and make those results dimensionless for a correlation between Nusselt and Reynolds numbers. The authors conclude that the correlation that best fit the experimental results is the one proposed in the paper, and define the validity of such correlation.

(RASHEDUL et al., 2014) presented a zero dimensional thermodynamic model for engine cycle analysis used for evaluate different ethanol gasoline blends. The model is based in the first law of thermodynamics to resolve combustion inside an engine using different mixture concentrations of ethanol and gasoline. The use of different heat transfer correlations available in literature, in case Annand, Woschni, Hohemberg and Eichelberg correlations, is compared based on the model results. In the end, the authors highlight that the best results were obtained by Hohemberg's correlation.

(CERIT; COBAN, 2014) used a finite element model to evaluate temperature and thermal stresses on a ceramic coated aluminum alloy diesel engine piston. The ceramic material is modeled for different thickness, and the temperature and thermal stresses are evaluated based only on the simulation results. The authors conclude that temperature and thermal stresses distribution are a function of coating thickness.

(OLMEDA et al., 2015) developed a correlation for estimation of in cylinder heat transfer coefficient h between gases and walls, considering the influence of intake air tumble motion on this coefficient. The authors proposed the modification based on a theoretical

review about heat transfer coefficient, performed the modification based on CFD 3D simulations, and calibrated the new model based on experimental results obtained in a single cylinder 2 stroke diesel engine operating under skip firing condition. The model proposed obtained a 70% reduction on the root mean square error, compared to the reference Woschni based model, for the case of high tumble engine.

(IRIMESCU et al., 2015) used experimental results obtained in an optical single cylinder research engine for two different flame images acquisition systems, in order to test current available heat transfer correlations and propose a new correlation, which best fits the experimental results. The authors considered the models proposed by Woschni and Annand, and compared the results for both correlations with the one proposed. The results obtained by the authors shows that the results obtained by the proposed model are quite similar to the ones obtained by the two literature correlations.

(SCHMITT et al., 2015b) performed DNS simulation on an engine like geometry during compression stroke, in order to capture the evolution of velocity and thermal boundary layers, and thus provide reference framework for validation of near wall flow models. The authors present several results for flow and thermal fields evolution, and based on those results the authors present several reference values for non dimensional variables essential for near wall flow models. The authors conclude that no logarithmic boundary layer profiles were found in the DNS results, which indicates that the commonly used wall function approaches needs to be reconsidered for the development of novel wall heat transfer models for ICE flows.

(SCHMITT et al., 2015a) performed DNS simulation of an engine like geometry during compression stroke, in order to capture the evolution of flow, temperature and composition fields. The authors conclude, based on the results, that the flow field at top dead center is anisotropic, and the average fluctuation velocities in the axial direction are approximately 30% smaller compared to those in the radial and azimuthal direction, posibly due to smaller axial dimension at TDC.

(CERDOUN; CARCASCI; GHENAIET, 2016) performed an in depth study concerning heat transfer through valves of internal combustion engines, basically dedicated to exhaust valves, but possible to apply to intake ones. The authors perform a finite element analysis of heat transfer through a single valve, and evaluate the boundary conditions for different heat transfer *phenomena* taking place at different valve surfaces. Using circumferential symmetry, the authors propose a 2D finite element model with seven surface boundary regions: combustion face, seat, stem-port, stem-guide, stem-tip, stem-port/guide, stem-guide/tip. The two last regions account for valve movement, once they are hybrid regions whose boundary conditions change during the calculation between two regions. Several heat transfer correlations are used, based on literature correlations, in order to represent boundary conditions for each surface region heat transfer *phenomena*, including contact heat transfer between valve seat and cylinder head respective surface. The results obtained are calculated temperature values as high as $860 \circ C$ for valve face regions, and low temperatures at the valve

tip close to $300 \circ C$. Once no comparison with experimental results is presented, the authors present as a propose for future work the comparison with experimental results.

(MICHL et al., 2016) derived and validated a new phenomenological model for calculation of heat transfer based on experimentally measured in cylinder pressure. The evaluation of the proposed model and comparison with previous models available in literature is performed by means of a comparison with wall heat transfer measurements performed at a compression ignition engine fueled with hydrogen. The engine is drilled and instrumented with 14 thermocouples in the cylinder head and 15 in the cylinder liner, in such a manner that the thermocouple junction is always parallel to the wall surface, and the signal from piston thermocouples are transmitted using a mechanical linkage using flexible wires. The authors conclude that the proposed model is validated to perform heat flux calculation, once it presents better agreement to experimental wall heat flux than the previous correlations.

(BROEKAERT et al., 2016b) presented an experimental study on the influence of some engine operation parameters over heat transfer rate of homogeneous charge compression ignition internal combustion engine. The authors performed a design of experiments analysis taking into account the effect of several engine control parameters, and implemented an analysis of variance to compare the influence of the parameters and of the interaction between the parameters. Among other conclusions, the authors state that peak heat flux is a quadratic function of volumetric compression ratio and intake air temperature, once both affect start of combustion.

(BROEKAERT et al., 2016a) presented an analysis of heat transfer in premixed spark ignition engines, aiming to identify factors that affect heat transfer. The authors highlight the importance of heat transfer between gases and combustion chamber walls, but with some comments about correlations frequently referenced in literature, specially Annand and Woschni correlations, once the development of those models was driven by fossil fuels based experiments. The authors affirm that usual heat transfer models their predictions, when the used fuel presents properties considerably different than fossil fuels in gaseous phase, for example ethanol or hydrogen. The authors conclude the analysis with the design of experiment for studying the influence of several parameters into heat flux measurement in internal combustion engine.

(ŠARIĆ; BASARA; ŽUNIČ, 2017) proposed a new model to calculate near wall heat transfer for engine CFD 3D models using RANS approach. The proposed model is validated for benchmark of turbulent nitrogen jet on a heated wall, and tested against literature experimental available data for a spark ignition engine. The wall heat transfer formulation is applied on a 90◦ sector grid of a spark ignition engine at 1500 rpm fueled with propane at equivalence ratio 0.87, and runs from -30 CAD until 30 CAD after top dead center, once the literature data is available only for this interval, using ECFM-3Z as combustion model. Two different grids are used, the coarse one with characteristic size of 1 mm, and the fine one 0.5 mm, and the results are presented for engine CFD 3D model using the proposed wall heat transfer approaches and

the formulation proposed by Han and Reitz (HAN; REITZ, 1997), in comparison with literature data. The authors conclude that the proposed model is superior than Han and Reitz formulation for cases involving meshes with y^+ ranging form the buffer region down to the viscous sub layer.

(LU et al., 2017) presented a numerical analysis of temperature field and thermal stress under steady temperature test applied to the piston of a diesel engine. The authors used a finite element method to calculate the temperature distribution and thermal stress, along with literature heat transfer coefficient correlations for all piston surfaces. The authors compared model results with measured temperatures for steady state temperature difference test, and after this comparison, used literature in cylinder gas temperature along with Woschni correlation to impose transient heat transfer boundary condition.

(MA et al., 2017) performed high speed micro PIV measurements in the boundary layer of a research single cylinder internal combustion engine, in order to evaluate the assumptions of algebraic wall models frequently used in engine CFD 3D models. The authors proposed a small part of the in cylinder domain for simulation of conditions relevant to the research engine operating condition of 400 and 800 rpm. Non equilibrium wall models were adapted to IC boundary layer domain and the performance of different models have been compared to experimental measurements, considering results for viscous and thermal wall boundary layer. The authors conclude that equilibrium wall functions yields acceptable results for the shear velocity if the first node is within the viscous sublayer, but shows substantial deficiencies in describing the in cylinder near wall region if the matching location is located outside the viscous sublayer.

(CUYPER et al., 2017) performed motored and fired tests in a four stroke, four cylinder spark ignition engine, instrumented with prototype thin film gauge heat flux sensors, to evaluate empirical heat transfer models. The main objective of the authors is to evaluate the semi empirical heat transfer models for in cylinder gas to wall heat transfer most used in engine thermodynamic analysis, which are affirmed to be Woschni and Annand correlations. The prototype heat flux sensors are installed at intake valve, squish surface and the end zone, and the authors described in details the sensor used, but did not mention the communication between the sensor and acquisition system, once the sensor seems to be a wireless one but no description of signal transmission is mentioned. The results are presented as traces for heat flux and convective coefficient during combustion analysis period, compared between measurements and calculations by Woschni and Annand.

(BENAJES et al., 2017) performed experimental evaluation of swirl effect on the global energy balance of a high speed direct injection diesel engine. Along with experimental apparatus and strategy, a set of zero dimensional models are used to calculate combustion parameters based on in cylinder measured pressure. Among other models, the authors used a nodal lumped conductance model to calculate wall temperatures in the chamber and ports, along with heat rejection repartition to coolant and oil, consisting of 102 nodes in the cylinder

head, 66 in the liner, 10 in the piston and some boundary nodes that take into account the oil, coolant, fresh air, in cylinder, intake and exhaust gases. Among other conclusions, the authors verify that swirl ratio increment did not always affect break thermal efficiency in the same way, and its global impact depends on the operating condition and the swirl level.

(TANOV et al., 2017) performed experimental tests to, along with a nodal heat transfer model, evaluate the influence of the number of injections on piston heat rejection of an optical compression ignition diesel engine operating at low temperature combustion conditions. The authors used PIV experimental data obtained at an optical access diesel engine using partially premixed combustion strategy for one, two and three injections. Along with PIV data, a model for swirl number and turbulent kinetic energy calculation was used coupled to a thermodynamic model and a nodal lumped conductance heat transfer model to calculate heat transfer coefficient from in cylinder reactive flow field to piston surface, piston surface temperature, heat release rate and heat flux density at piston surface. The results show that the case with single injection shows the highest heat release rate, heat flux density and heat rejection, and heat flux with triple injection was 4% higher than double injection.

(BROATCH P. OLMEDA; WAREY, 2017) presented an experimental study to evaluate the impact of swirl on in cylinder heat transfer in a light duty diesel engine, in which study a nodal heat transfer model based on lumped conductance is evaluated. The authors used a four cylinder 1.9L diesel engine, instrumented with 88 K-type thermocouples, 54 of them in the cylinder head and other 34 in the cylinder liner. Along with temperature measurements, a zero dimensional thermodynamic model is presented, for which the lumped conductance heat transfer model is coupled to obtain calculation of rate of heat release, in cylinder gas temperature, among other combustion related quantities. The authors concluded that the highest impact of swirl was found in the center of the firedeck, and that the zero dimensional model was able to simulate temperatures and heat fluxes properly.

(WANG et al., 2018), (WANG et al., 2017), (DENG et al., 2017) and (LV et al., 2015) performed numerical and experimental investigations on piston cooling galleries of diesel engines. The authors used similarity to implement deionized water experiments for evaluating two phase flow heat transfer inside piston cooling galleries, and performed volume of fluid simulations for analyzing two phase flow heat transfer phenomena. The authors concluded that both impinging velocity and liquid filling ratio must be simultaneously considered for heat transfer efficiency, and proposed a method to qualitatively estimate heat transfer enhancement of gas liquid two phase flow during periodic piston motion, based on wall shear stress and average liquid phase velocity.

2.5.4 Articles related to conjugate heat transfer at engine CFD 3D models

(KIKUSATO; KUSAKA; DAISHO, 2015) used a 60○ sector mesh to perform engine CFD 3D simulation of a diesel engine using RANS approach, in order to predict wall surface temperature distributions and its effects at combustion chamber. The authors used a 1D unsteady

heat transfer model to calculate wall heat transfer, and a detailed chemical kinetics was used to solve combustion, for ten consecutive cycles in order to obtain convergence of wall temperature calculation. The model is applied to a single cylinder compression ignition engine fueled with diesel, and the results are compared to experimental ones for in cylinder pressure trace. The authors conclude that the heat flux form the in cylinder gases to the combustion chamber walls is considerably affected by wall temperature values, therefore the failure to consider the wll temperature distribution can affect the calculation of combustion and emissions.

(MISDARIIS; VERMOREL; POINSOT, 2015) performed a CHT analysis between an engine CFD 3D modelling using LES approach for turbulence, coupled to a finite element heat transfer model for the complete engine head, and valves. The authors used the coupled CHT analysis to better estimate engine wall temperatures and thus obtain a better prediction of knocking occurrence and knock spot location. The engine CFD 3D model is performed at a single cylinder research engine for the operating condition of 1800 rpm, 19 bar of IMEP, using a two step chemistry approach for combustion modelling. The authors present results for cyclic variability of temperature, heat fluxes and in cylinder pressure, along with wall temperature and flame surfaces. The authors present the conclusions without performing numerical comparison between experiment and engine CFD model, but state that the focus of the paper is the strategy that allows obtaining more realistic wall temperature values, although no comparison to experimental results are performed. No information about trapped mass of air, injected mass of fuel or lambda is presented by the authors, and nothing is stated about pulsating flow effects at intake ducts.

(MEHDIPOUR; BANIAMERIAN; DELAURÉ, 2016) used a CFD 3D model of a conventional rectangular channel to simulate nucleate boiling occuring inside internal combustion engine cooling galleries. The authors used a mixture model available at ANSYS Fluent commercial software to consider two phase mixture flow, which is capable of calculating any value of volume fraction between 0 and 1 at each finite volume cell. The authors compared their results with results available in literature for different Reynolds number values, and concluded that the model results is able to represent heat transfer and bubble formation in cooling passages of vehicle engines, once their model is independent from geometry. Nevertheless, the authors state that this model is not able to represent experimental results for situations where vapour film is formed near the wall, which reduces the local heat transfer coefficient an causes a local increase in wall temperature.

(SCHMITT et al., 2016a) performed a DNS simulation on an engine like geometry during the compression stroke, in order to evaluate local wall heat flux distribution and provide validation data for the ICE wall heat transfer using DNS. The authors used an engine like geometry, for which data is available in literature, to perform DNS simulations during compression stroke in a symmetric domain, using refined grids near the wall smaller than 13.8 μm to resolve near wall flow and heat transfer. A separate DNS of intake stroke was performed to calculate initial conditions for compression stroke, and boundary conditions for wall

temperatures are constant at 500 K. The authors conclude based on DNS results that the correlation of the temperature field with the local heat flux distribution depends strongly on the distance to the wall, meanwhile the correlation of the velocity field with the local heat flux distribution depends strongly on the flow direction.

(BERNI; CICALESE; FONTANESI, 2017) proposed a modified thermal wall function for the estimation of gas to wall heat fluxes in engine CFD 3D simulations, applied to high performance spark ignition engines. The wall function proposed by the authors is based on two of the most used in the literature: Han and Reitz (HAN; REITZ, 1997) and Angelberger (ANGELBERGER; POINSOT; DELHAY, 1997). For evaluating both wall functions and compare with the proposed one, the authors performed a series of experimental and numerical analysis, including a global thermal balance over the geometry of four different high performance spark ignition engine, for one specific condition at each engine. The heat flux boundary conditions for the CHT analysis are provided by engine CFD 3D simulations using STAR-CD commercial code, with ECFM-3Z as combustion model. The authors demonstrate with the results presented that the previous models are valid for the engine used for validation, but not for the turbocharged engines considered. The authors conclude that both previous models are still valid for engine CFD 3D models, for cases where low thermal gradient associated to smaller power densities are observed.

(ZHANG, 2018) performed conjugate heat transfer between engine CFD 3D and discrete heat diffusion in solid walls of a sector mesh from the cylinder of a diesel engine. The authors used open source code KIVA-4 to implement coupled calculation of in cylinder reactive flow along with heat diffusion at cylinder head and piston, in a sector grid, which is a grid applied to a sector of a circular domain considered symmetric. The results presented by the authors for wall temperature evolution during 80 cycles shows piston temperatures above 700 K at piston bowl edge, meanwhile other regions of the piston are at temperatures around 550 K, including piston bowl surface. Consequently, results for gas temperature close to piston bowl edge shows that these region is at considerably higher temperatures than the rest of the in cylinder gases. Among other results, the authors presented the comparison between experimental results for soot and NO_X emissions for few timesteps close to top dead center, and the comparison is declared to be in good agreement.

(MANDANIS et al., 2018) presented a comparison between LES and DNS turbulence approaches for calculation of wall heat flux and thermal stratification in a geometry similar to the geometry of an internal combustion engine. The authors used the same geometry as (SCHMITT et al., 2016a; SCHMITT; BOULOUCHOS, 2016; SCHMITT et al., 2015b; SCHMITT et al., 2015a), who performed DNS modelling of a symmetrical geometry similar to the one of an internal combustion engine. No experimental data is used, so the reference is the DNS simulation. The grid declared is a purely hexahedral one with an average cell size below 0.4 mm, and the first grid layer at the cylinder liner is 200 μm thick normal to the wall. The authors conclude that LES models significantly underestimates the wall heat flux,

especially during the second part of compression.

(BROATCH et al., 2019) presented a new approach to study heat transfer in internal combustion engines by 3D modelling. The authors performed a previous combustion simulation in GT-Power 1D combustion model using constant wall temperature, in order to obtain the rate of heat release trace for the combustion analysis interval. The calculated values for rate of heat release was used as boundary condition for a multicycle analysis in a three dimensional model for conjugate heat transfer, which resolves coupled iteractively the thermal fluid dynamics for the reactive in cylinder flow and heat transfer at wall using finite element method. The authors present as results several traces comparisons between in cylinder pressure, temperature, rate of heat release between model results only, for combustion analysis and for rate of heat release boundary conditions analysis. The authors conclude that using rate of heat release as boundary conditions produces approximately the same results as combustion results, with a considerably smaller computational time.

2.5.5 Articles related to verification and validation of CFD models

(MARE; KNAPPSTEIN; BAUMANN, 2014) performed systematical investigation of the applicability of quality criteria for in cylinder flow simulations, using validated engine CFD 3D models of a direct injection spark ignition engine with LES approach for turbulence. The authors apply different quality criteria for LES modelling proposed in the literature, under the explanation that Richardson extrapolation cannot be used to LES models, once modelling and numerical errors cannot be separated. The authors conclude that all of the verified quality criteria are capable of characterizing the flow field in terms of adequacy of grid resolution.

(MARE; KNAPPSTEIN, 2014) evaluated the results of cold flow engine CFD 3D simulations using LES approach by means of statistical analysis and proper orthogonal decomposition. The authors used a complete engine geometry to solve the engine CFD 3D model using LES approach under operating conditions without fuel injection, and evaluated the flow field variables such as velocity, kinetic energy and flow frequencies by means of statistical analysis and proper orthogonal decomposition. The authors conclude that proper orthogonal decomposition is able to provide useful insight in the flow topology, and that the system complexity can be reduced by expressing the flow field by a few modes without loosing too much of the information contained in the turbulent structures.

(XING, 2015) proposed a general framework for verification and validation concerning CFD 3D models using LES approach for turbulence. The authors base their framework at the ones proposed for RANS models, but highlight that the actual framework have limitations at coupling numerical and modeling errors, not considering modeling error in the validation uncertainty and don't consider mixed numerical approaches for the discretization error. The author concludes that the framework proposed can be used for different CFD 3D modelling applications using LES approach for turbulence.

2.5.6 Summary of state of the art

From the resume presented at the state of the art, it can be seen that engine CFD 3D modelling is used for several applications, and RANS approach for turbulence is still very important when the full engine is to be simulated (MILLO et al., 2014; BARATTA; RAPETTO, 2014; PERINI; MILES; REITZ, 2014; KHALILARYA; NEMATI et al., 2014; LINSE; KLEEMANN; HASSE, 2014; CLENCI et al., 2014; KIKUSATO; KUSAKA; DAISHO, 2015; BERNI; CICALESE; FONTANESI, 2017). Indeed, several of the LES or DNS engine CFD 3D models are performed at engine like geometries or simplified engine geometries, due to the prohibitive computational cost of such approaches (BUHL et al., 2017; FAN et al., 2018; MASOULEH et al., 2018; SCHMITT et al., 2015a; SCHMITT et al., 2015b; SCHMITT et al., 2016b; ZHANG, 2018).

Nevertheless, there is a clear dismiss in the state of the art concerning volumetric efficiency, pulsating flow effects and trapped mass of air, either for RANS, LES or DNS approaches of engine CFD 3D modelling. Few papers identify the excess of air, and some of them including propose some analysis to reduce the trapped mass of air, for example the use of Bernouli's equation (BAUMANN; MARE; JANICKA, 2014), and at any moment connect the excess of air to the pulsating flow occurring at intake, or either perform engine CFD 3D modelling of different engine operating condition in order to identify systematic excess of air.

Concerning pulsating flow modelling, it can be seen that the most important modelling and validation of pulsating flow at intake ducts is performed at zero dimensional or one dimensional modelling (SOUZA et al., 2019; HANRIOT; QUEIROZ; MAIA, 2019), where dedicated models are used along with modal analysis in order to identify the most important frequencies, and their impact at volumetric efficiency and thus at trapped mass of air per cycle. Meanwhile for CFD 3D modelling, it is important to note that some papers in literature started to take more attention to the flow at intake ducts, and dedicated LES or DNS CFD 3D models (SAKOWITZ; MIHAESCU; FUCHS, 2014; GIANNAKOPOULOS et al., 2017). Although, neither have used pulsating flow boundary conditions, or compared the results obtained to experimental results, or either verified excess of air, reduction of trapped mass of air due to a specific frequency modeled, or any similar analysis. This way, the literature is starting to take note of the importance of considering pulsating flow effects at engine CFD 3D modelling, still it is very preliminary, in such a manner that no study has been found relating the frequencies of the pulsating flow at intake ducts to the trapped mass of air, or to the volumetric efficiency, calculated by any engine CFD 3D model.

Concerning engine heat transfer modelling, it is clear that CHT-engine CFD 3D analysis is now one of the most investigated subjects, being subjects of several literature publications (KIKUSATO; KUSAKA; DAISHO, 2015; MISDARIIS; VERMOREL; POINSOT, 2015; MEHDIPOUR; BANIAMERIAN; DELAURÉ, 2016; SCHIFFMANN et al., 2016; BERNI; CICALESE; FONTANESI, 2017; FAN et al., 2018; ZHANG, 2018) . All of the papers highlight two important aspects: first, the importance of the calculation of wall

temperatures along with solving reactive flow field, either for RANS, LES or DNS engine CFD 3D modelling; second, the great computational effort dedicated to resolve CHT-CFD coupled iteractive or decoupled iteractive, when heat transfer is modeled using 3D finite element analysis (MANDANIS et al., 2018; BROATCH et al., 2019). It is also important to note the great quantity of papers presenting heat transfer correlations for different engine parts, such as piston, exhaust valves and ducts, and not only the heat transfer between in cylinder gases and walls (LIU et al., 2014; RASHEDUL et al., 2014; CERDOUN; CARCASCI; GHENAIET, 2016).

Concerning verification and validation of engine CFD 3D models, some papers has been found with the first efforts towards the quantification of differences between model and experiment, although those efforts are nowadays quite distant (MARE; KNAPPSTEIN; BAUMANN, 2014; MARE; KNAPPSTEIN, 2014; XING, 2015). More efforts must be made in order to present methods to quantify the differences between engine CFD 3D model results and correlated experimental data, or use work flows already available, for example, ASME V&V 20 standard and all of its references (ASME, 2009).

In this thesis, it is presented a contribution to the state of the art of engine CFD 3D modelling, by means of a methodology capable of producing accurate results for different engine operating conditions using RANS approach for turbulence, without changing any of the constants of the sub models. The proposed methodology takes into account the effects of pulsating flow at intake ducts (manifold, runner, port) over volumetric efficiency, by means of calculating a pulsating flow head loss and imposing it over the engine CFD 3D model, and also solves decoupled iteratively a zero dimensional global heat transfer model, in order to calculate the wall temperatures along with the calculation of the reactive flow field.

3 METHODOLOGY

In chapter 3, the methodology proposed and infrastructure available are presented. In section 3.1, the computational infrastructure used is described, in terms of hardware and software. In section 3.2, the experimental reference for comparison of engine CFD 3D model is presented. In section 3.3, the geometry of the simulation domain is presented, along with its correlation to the experimental reference. In section 3.4, it is presented the basic information about grid dependence study, along with the selected grid and time step. In section 3.5, the equations used for the model are presented. In section 3.6, the description of the boundary conditions is presented. In section 3.7, the global heat transfer model is presented, along with literature correlations implemented at this model. In section 3.9, it is described the presentation of results in chapter 4, and in section 3.10, the final remarks concerning chapter 3 are presented.

In section 3.8, the simulation methodology for the decoupled iterative process between engine CFD 3D and global heat transfer models is presented. This methodology involves treatment of experimental data at cycle selection procedure, treatment of intake pressure boundary condition at intake pressure correction procedure, and finally the decoupled iterative solution between engine CFD 3D and global HT models. A workflow of the method is presented in Figure 3.7, which illustrates the strategy proposed in this thesis to perform engine CFD 3D simulation of each engine operating condition, without changing any of the constants of the sub models, based on the treatment, modification, modelling and analysis of boundary conditions, specifically intake pressure and wall temperature.

Unprecedented topics are:

- the global heat transfer model, in section 3.7;
- the cycle selection procedure, in subsection 3.8.1;
- the intake pressure correction, in subsection 3.8.2;

The geometry and grid dependence study sections are complemented with data and explanation available at Appendix A and Appendix B, respectively. Those extra information are included because both important for the specific workflows concerning geometry and grid, but are not directly connected to the main simulation methodology.

3.1 COMPUTATIONAL INFRASTRUCTURE

In this section, computational infrastructure available in CTM-UFMG is described, in terms of hardware and software for engine CFD 3D simulation. It is also briefly described the part of this infrastructure used for this project.

3.1.1 Hardware

Engine CFD 3D simulations are performed at CTM-UFMG cluster, which is composed by several personal workstations used for preparation and analysis of simulation results and treatment of experimental data, a few simulation servers dedicated to engine CFD 3D simulation and one server dedicated to perform as license server.

For this thesis, it has been used one personal workstation for preparation and analysis of simulation results, one personal workstation for treatment of experimental data provided by CTM, one personal mobile computer for graphics and analysis, and seven simulation servers. The personal computers were available most of the time, 4 of the simulation servers were partially available during the project, and the other 3 simulation servers were only available at the last months of the project.

The personal computer for preparation and analysis of engine CFD 3D simulation is an Intel Pentium 5, 4 physical cores, 16 GB of RAM memory, running CentOS LINUX distribution. The personal computer for treatment of experimental data is an Intel Celeron, 1 physical core, 2GB of RAM memory, running Windows 10. Four of the simulation servers, which was most used for simulating engine CFD 3D cases in this project, are Intel Server, 16 physical cores each, 64 GB of RAM memory, running CentOS LINUX distribution. The other three simulation servers, which was used specifically in the last months of this project, are Intel Server, 36 physical cores each, 128 GB of RAM memory, running CentOS LINUX distribution.

3.1.2 Software

Engine CFD 3D simulations are performed using Siemens STAR-CD commercial code, coupled to expert module ES-ICE, dedicated to calculate moving meshes for engine CFD 3D simulations. This software operates in spread licensed system, in such a manner each part of the program needs specific licenses. For this thesis, the following parts of the code are used: STAR-CD main code; ES-ICE expert modulus; parallel processing and combustion models.

For STAR-CD main code, half of the project was performed with 8 licenses, and the other half with 16 licenses. For ES-ICE expert modulus, half of the project was performed with 8 licenses, and the other half with 16 licenses. For parallel processing, half of the project was performed with 50 licenses, and the other half with 150 licenses. For combustion models, half of the project was performed with 5 licenses, and the other half with 10 licenses.

For parallel processing and simulation cases, not all of the licenses are available. For the used program, ES-ICE and combustion models specific licenses cannot be used for parallel processing, although they must be available in order to perform the simulation. This way, for maximum parallel processing licenses, only STAR-CD and parallel processing licenses are accounted, and the maximum of parallel processing available is 166 licenses.

3.2 ENGINE AND TEST BENCH

The engine used is a single cylinder research one, as described in previous master degree dissertation produced in CTM-UFMG (COSTA, 2017; NETTO, 2018). The reason for this choice is the availability of the engine itself, along with the availability of detailed engine geometry and experimental data for this engine. It is a four strokes spark ignition, four valves per cylinder, used as direct injection. The information about the engine is summarized in Table 3.1.

Table 3.1 – Single cylinder research engine parameters.

Model	AVL 5495
Type	Single Cylinder
Bore	82 mm
Stroke	86 mm
Connecting rod length	144 mm
Volumetric compression ratio	11,5:1
Swept volume	454,16 cm^3
Number of valves	4
Injection	DI

SOURCE: (COSTA, 2017)

The engine and the experimental apparatus are illustrated in Figure 3.1, where the location of the following sensors are indicated: intake gas temperature sensor; manifold air pressure sensor (MAP); intake pressure sensor; in cylinder pressure sensor; lambda sensor and exhaust pressure sensor. In this assembly, a flow box was used at intake manifold in order to control turbulence and vorticity of the flow field inside the cylinder. The mentioned assembly produced poor results in terms of volumetric efficiency, so one of the objectives of the simulation results is to contribute to a better understanding of this problem.

The description of the experimental apparatus is far beyond the scope of this thesis, and for this purpose there are references that used the same engine at CTM-UFMG (COSTA, 2017; NETTO, 2018). Still, there are specific sensors for which the measurements are relevant for obtaining boundary conditions and performing validation process, and for those sensors the most important information are in Table 3.2.

Except for the fuel mass flow measurement system, the position of the sensors in Table 3.2 are highlighted in Figure 3.1. The position of the other sensors, their relative distances and other information are far beyond the scope of this thesis, and for this purpose the literature is indicated (COSTA, 2017; NETTO, 2018).

3.2.1 Engine operating conditions

For the selected engine, experimental data concerning operation at the conditions given in Table 3.3 are available at CTM-UFMG, and therefore are used in this thesis for simulation.

Figure 3.1 – Engine test bench.

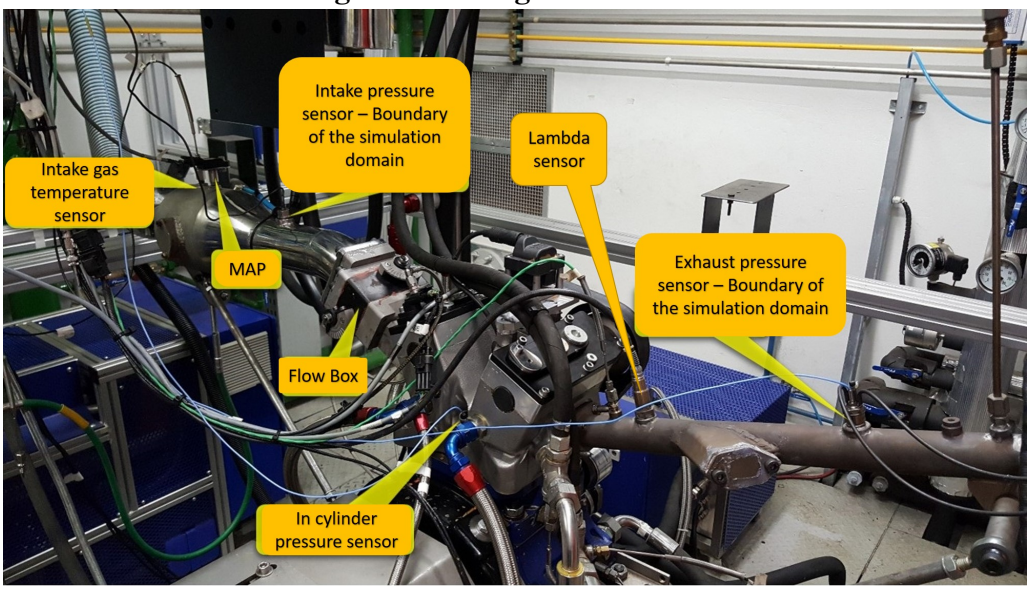

SOURCE: Adapted from (COSTA, 2017).

Table 3.2 – Relevant experimental sensors for simulation procedure. Uncertainties are given in terms of full scale values (FS) or measurement values(M).

Sensor	Sensor model	Type	Range	Source for uncertainty	Uncertainty (Type B)
In cylinder pressure sensor	AVL GU22C	Piezoelectric	0 - 250 bar	AVL GmBH	±0.3%(FS)
Intake pressure sensor	AVL LPD11DA05	Piezoelectric	0 - 5 bar	AVL GmBH	±0.1%(FS)
Exhaust pressure sensor	AVL GU21C	Piezoelectric	0 - 10 bar	AVL GmBH	±0.1%(FS)
Lambda sensor	BOSCH LSU 4.9	Wide band	0.65 - 8.0	BOSCH GmBH	0.009(FS)
Fuel mass flow	AVL 733	Gravimetric	0 - 160 kg/h	AVL GmBH	±0.05%(M)

SOURCE: Adapted from (COSTA, 2017).

The use of the engine operating conditions at Table 3.3 is performed for the availability of data, and because there are three different engine speeds and engine loads.

Table 3.3 – Engine operating conditions.

Engine load IMEP [bar]	8.0	-	X	X
	5.0	-	-	X
	3.0	X	X	X
Engine speed [rpm]		1000	2000	2500

SOURCE: Elaborated by the author.

The engine loads selected include two conditions at maximum load (8.0 [bar]), three conditions at minimum load (3.0 [bar]), and one condition at intermediate load (5.0 [bar]), for this reason a wide range of engine loads is evaluated. The engine speeds selected include the

lowest speed (1000 [rpm]) and two intermediate speeds (2000 [rpm] and 2500 [rpm]). This way, a considerable range of engine speeds is covered.

There is also the constraint of computational time available, this way six engine operating conditions, which cover considerable ranges of engine speed and load, are resolved at the available time concerning the computational infrastructure described in section 3.1.

Experimental data is available for in cylinder pressure evolution for 200 cycles and average in cylinder pressure evolution, indicated mean effective pressure (IMEP) for 200 cycles and average IMEP, evolution of intake and exhaust pressures for 200 cycles and average intake and exhaust pressure. Experimental data is also available for combustion analysis, for which data is available from -30 crank angle degrees (CAD) until 90 CAD, which is considered combustion analysis interval. In cylinder gas mixture calculated temperature is one of the combustion analysis experimental data. Other information from experimental data, is injected mass of fuel per cycle and trapped mass of air, both calculated based on measured quantities, and lambda factor, which is measured at exhaust duct.

Fuel used is ethanol, directly injected into combustion chamber. The properties of ethanol used at the experimental tests are described by (COSTA, 2017; NETTO, 2018).

3.3 GEOMETRY AND SIMULATION DOMAIN

The geometry of the simulation domain is described in Figure 3.3 and it consists in the volume of fluid geometry enclosed by the engine and experimental apparatus described in Figure 3.1, restricted to the regions inside the cylinder, intake and exhaust ducts (manifolds, runners, ports), where the flow of the working fluids takes place. The generation of this geometry comes from the treatment of the CAD assembly of the engine solid parts, as described in Figure 3.2.

In Figure 3.2, the drawings of all of the solid parts for engine head, piston, cylinder, along with intake and exhaust manifolds are assembled in a geometry similar to the engine test bench described in Figure 3.1. Also in Figure 3.2, the limits of the domain are highlighted by the regions which correspond to the intake and exhaust pressure sensors, which are also correlated to Figure 3.1.

Based on the CAD assembly in Figure 3.2, the geometry of the simulation domain described in Figure 3.3 is obtained from the subtraction between engine solid parts and a group of reference fluid volumes. This subtraction operation, represented in Figure A.1, produces the geometry in Figure 3.3 which consists in the negative parts of the intake and exhaust manifolds and ports, along with in cylinder.

For sake of brevity, the details of the geometry of the simulation domain are better described in Appendix A. The combination of the simulation domain and the solid parts of the engine are described in Figure A.1, in such a manner to highlight the correspondence between Figure 3.2 and Figure 3.3. Indeed, both Figure 3.2 and Figure 3.3 have the regions

Figure 3.2 – Engine parts assembled in a CAD drawing.

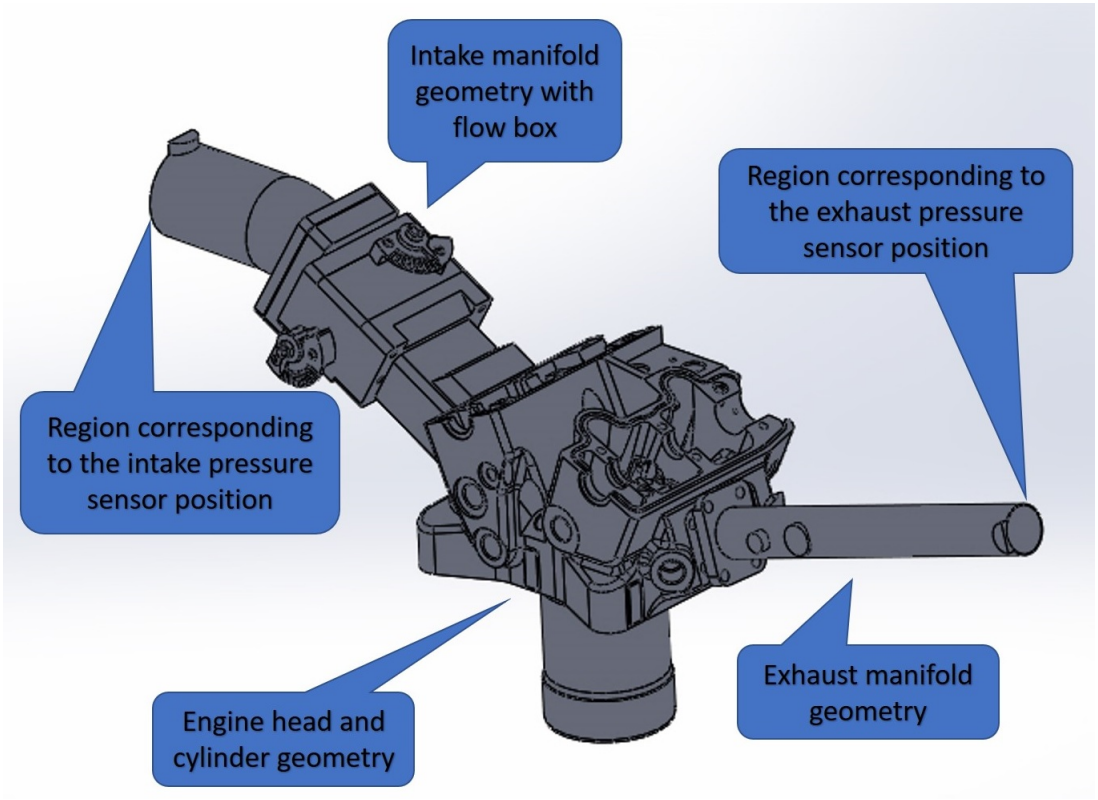

SOURCE: Elaborated by the author.

corresponding to intake and exhaust pressure sensors positions highlighted, along with other important regions. This way, Figure 3.1, Figure 3.2 and Figure 3.3 are correlated, and the simulation domain in Figure 3.3 represents the volume of fluid of the engine described in Figure 3.1.

The geometry of the simulation domain is based in the engine CAD files, so its main features are captured. However, due to limitations in computational resources, the geometry is simplified in order to make it possible meshing and simulation processes, this way the simulation domain has small differences in comparison to the real geometry. Although those simplifications are considered, the differences between experiment and model for combustion chamber volume, total volume and volumetric compression ratio are smaller than 0,5%, as it can be seen in Table 3.4. The values of engine volume were measured at CTM-UFMG, and are based on the methodology described by (COSTA, 2017).

Table 3.4 – Comparison between experiment and model volume and volumetric compression ratio.

Parameter	Experiment	Model	Difference
Combustion chamber volume $[cm^3]$	43.32	43.25	0,15%
Total volume $[cm^3]$	497.49	497.43	0.01%
Volumetric compression ratio $[dim]$	11.48	11.50	-0.14%

SOURCE: Elaborated by the author.

Once the geometry of the simulation domain is defined in Figure 3.3, it is important to

Figure 3.3 – Geometry of the simulation domain, which consists in the volume of fluid regions inside intake manifold, intake port, in cylinder, exhaust port and exhaust manifold.

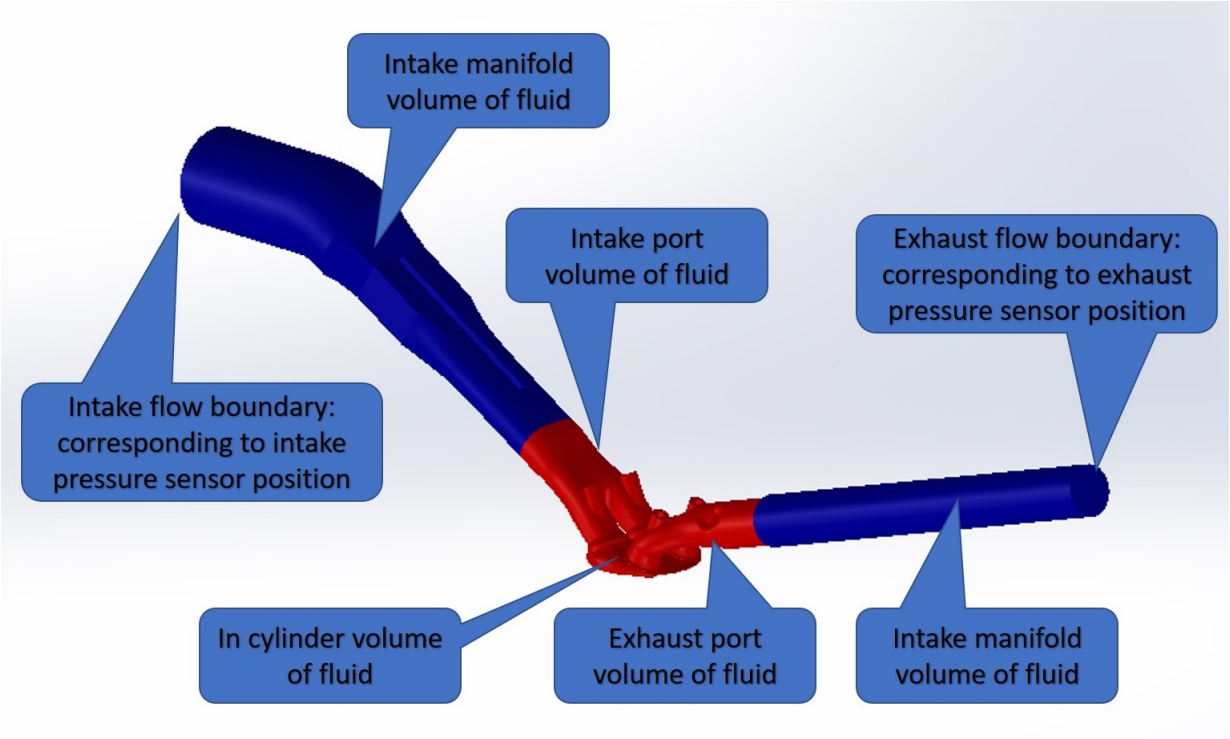

SOURCE: Elaborated by the author.

highlight the physical meaning of each surface bounding this geometry. The only flow surfaces are one at intake manifold, for intake inflow, which corresponds to intake pressure sensor position, and the other one at the exhaust manifold, for exhaust outflow, which corresponds to exhaust pressure sensor position. It is important to reinforce the correspondence between Figure 3.1, Figure 3.2 and Figure 3.3, and to state that both flow boundaries of the simulation domain are defined at pressure measurement regions, which can be verified by the comparison of the aforementioned figures, along with the figures contained in Appendix A. All of the other boundaries are wall regions, where the flow is limited by solid surfaces at the flow ducts and inside the cylinder.

3.4 GRID STUDY

Grid dependence study is performed to evaluate how engine CFD 3D model results are affected by the size of the grid used, and also by the time step used. It is also an objective to define the best grid and best time step to be used based on the compromising between quality of the results and computational cost. The more in depth description of the grid study is presented at Appendix B, and in this section only the most important information is described.

3.4.1 Grid generation

The geometry of the simulation domain, described in Figure 3.3, is used in the grid generation procedure, as described in section B.1. For each grid, a 2D template is generated based on cylinder bore, cylinder dome and valves relative geometry, than used to build a 3D template. The 3D template is used along with cylinder, intake and exhaust ports geometry to generate a reference mesh, which is used to create the mesh database necessary for simulation of moving parts. After the database is ready, the mesh for any instant during engine cycle can be previously generated and evaluated, similar to the cylinder and ports mesh at TDC in Figure B.2 and at BDC at Figure B.3, or to the mesh corresponding to the complete simulation domain at BDC in Figure 3.4, and the physics of the case can be introduced in order to perform the engine simulation.

In Figure 3.4, it is illustrated the grid for the complete simulation domain at BDC, for the grid with a reference characteristic length of 1 mm. This illustration is perform in order to make it easier the comparison between Figure 3.1, Figure 3.2, Figure 3.3 and Figure 3.4, and to see how the engine volume of fluid geometry at section 3.2 is represented by the engine CFD 3D model in a discrete manner.

Figure 3.4 – Complete simulation grid at bottom dead center, for the grid 1 with a characteristic length of 1 mm.

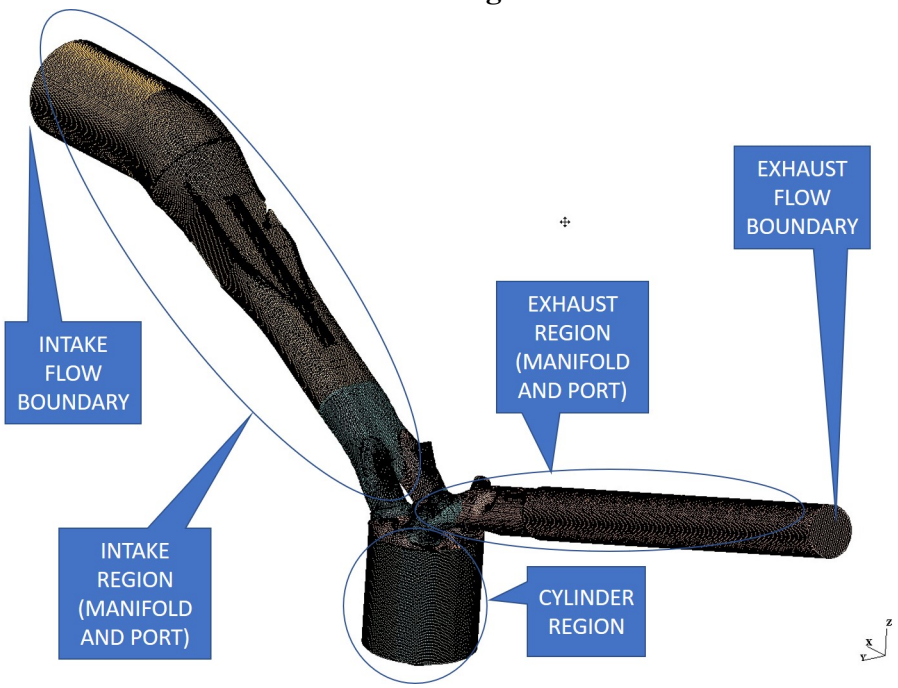

SOURCE: Elaborated by the author.

3.4.2 Grid refinement based on characteristic length

The grid dependence study performed in this thesis, described in Appendix B, has 4 consecutive refined grids, whose refinement process has been guided by characteristic length h. The characteristic length is evaluated for 2D template in subsection B.1.1, and also for

meshes generated at TDC and BDC in subsection B.1.2, in order to control and evaluate mesh generation. Based on ASME V&V20 (ASME, 2009), the characteristic length h is calculated by Equation 3.1:

$$h = \left[\frac{\sum_{i=1}^{N} \Delta V_i}{N}\right]^{\frac{1}{3}} \tag{3.1}$$

Where ΔV_i is the volume of the i_{th} cell, and N is the total number of cells in the grid or grid block. The grid refinement factor, $r = [h_{coarse} \backslash h_{fine}]$, is used in this study with a reference value $r = 1.11$ for the consecutive grid refinements, where h_{coarse} is relative to the coarser grid and h_{fine} is relative the finer grid, for any comparison. The reference values for characteristic length are listed in Table 3.5. The actual values for the characteristic length are presented in section B.1, along with the complete description of the grid generation process.

Table 3.5 – Reference characteristic length for different grids used in this work.

GRID	1	2	3	4
h $[mm]$	1.000	0.900	0.810	0.720
r $[dim]$	-	1.11	1.11	1.11

SOURCE: Elaborated by the author.

One of the standard workflows for verification and validation at CFD 3D models available nowadays recommends that grid refinement ratio should always be greater than 1.3, in order to achieve verification and validation. One important information described at subsection B.1.4, is that the computational cost estimated for the use of a grid refinement factor greater than 1.3 is prohibitive, and for this reason $r = 1.11$ is used in this thesis. The most important implication is that one result obtained by the engine CFD 3D model could even produce the calculation of an uncertainty value associated to this specific result, but this uncertainty would not be according the this specific standard for verification and validation, once the ratio for grid refinement is not according to the standard. This way, it is mandatory to highlight at this point that in this thesis no verification or validation workflow is considered, once the methodology proposed here is a necessary step towards those objectives. Moreover, in order to attend to any CFD 3D verification and validation workflow at engine CFD 3D models, other methodologies need to be developed, in order to complete verification and validation workflow for this application.

3.4.3 Grid dependence study

The last step in the grid dependence study is the comparison of results between different grids, which is described in section B.2. One of the engine operating conditions is selected from Table 3.3, in case, 1000 rpm 3 bar. For this engine operating condition, the engine CFD 3D model is performed at each of the four grids described at Table 3.5, using experimental data for intake pressure boundary condition. In order to compare engine CFD 3D results between different grids, combustion cycle average variables, for example IMEP, would

be the first option, but for all of the 4 grids simulated using experimental data for intake pressure boundary conditions, poor mixture is produced inside the cylinder, and no combustion results are obtained. This is better described in section B.2, and the poor mixture obtained by the engine CFD 3D model using experimental data for intake pressure boundary conditions is one of the most important results, in section 4.1.

Trapped mass of air inside the cylinder is a mean variable for any kind of engine model, and is fundamental for correct evaluation of engine performance. A more in depth discussion about the selection of in cylinder trapped mass of air for the grid dependence study evaluation variable is presented in section B.2. This way, trapped mass of air inside the cylinder is chosen as evaluation variable for grid dependence study. Each engine cycle produces one single value of trapped air mass, and those values are compared between consecutive grids. Equation 3.2 is used to calculate $\Delta\phi\%$, which is the difference between generic variable ϕ for grids i and $i+1$:

$$\Delta\phi\% = \frac{\phi_{i+1} - \phi_i}{\phi_i} \tag{3.2}$$

Where ϕ_{i+1} is the value of ϕ at grid $i+1$, and ϕ_i is the value of ϕ at grid i. In this study, trapped mass of air inside the cylinder is selected, and should be used in place of ϕ in Equation 3.2. The most important results for grid dependence study are presented in Table 3.6, and more in depth results are presented in Table B.9 at Appendix B.

Table 3.6 – Grid dependence study results.

Grid	1	2	3	4
h [mm]	1.000	0.900	0.810	0.729
Trapped air mass [mg]	212.4	211.0	210.4	208.4
$\Delta\phi\%$	-	-0.69%	-0.29%	-0.96%

SOURCE: Elaborated by the author.

From the results for the grid dependence study in Table 3.6, it is possible to observe that the differences between trapped air mass results obtained for the evaluated grids are all below or equal to 1.0%. From Table B.9 in Appendix B, it can also be estimated that the simulation of grid 5 would require 52 extra days of simulation, which is prohibitive. Considering a quality criteria of 2.0% for the grid dependence study, although the differences between trapped mass of air are reducing for all of the grids tested, the reduction obtained doesn't justify the simulation of a grid finer than grid 4, due to the computational cost associated.

Based on the results presented in Table 3.6 and Table B.9, grid 2 is selected for presenting the best compromising between quality of results and computational cost, similar to section B.2.

3.4.4 Time step refinement

The evaluation of the change in the results due to a change in the time step is the last task in the grid dependence study performed in this thesis. Once grid 2 is already selected as

the best trade off between quality of results and computational cost, it is used for the time step refinement. For that purpose, the results of the engine CFD 3D model are also evaluated for the selected grid using two different time steps.

The time step used at all of the grids is 0.1 CAD, and the simulation runs for 3 cycles, which makes it a total of 22,295 time steps per simulation, as described in Table B.10 at section B.3. For the time step refinement test, a time step of 0.05 CAD is used, which is half of this described time step, making the engine CFD 3D model runs for a total of almost 45 thousand time steps. The most important results obtained by the time step refinement test are presented in Table 3.7.

Table 3.7 – Time step evaluation

TIME STEP	1	2
Time Step [CAD]	0.10	0.05
Trapped air mass [mg]	211.0	209.2
$\Delta\phi\%$	-	-0.83%

SOURCE: Elaborated by the author.

Similar to the comparison of results between different grids, the trapped mass of air is selected in order to evaluate the quality of results between the two different time steps, and the difference obtained is smaller than 1.0%. It is described in Table B.10 that the second time step consume almost 100% more simulation time than the first one, for the same grid, and produces almost the same result.

This way, the time step of 0.1 CAD, which is the first one, is selected for the best compromising between quality of results and computational cost.

3.5 MATHEMATICAL PHYSICS MODEL

In this work, the CFD 3D model for the thermal fluid dynamics processes occurring inside an internal combustion engine (Engine CFD 3D), resolves the equations of conservation of mass (Equation 2.1), conservation of *momentum* (Equation 2.2, Equation 2.3 and Equation 2.4), conservation of energy (Equation 2.5) and the ideal gas state equation. The Reynolds Averaged Navier Stokes (RANS) form of these equations are solved in an iterative coupled manner using the PISO algorithm, for the flow variables of interest ($\bar{\rho}$,$\bar{U}$,$\bar{V}$,$\bar{W}$,$\bar{I}$,$\bar{P}$), as described in subsection 2.1.3.

The above mentioned equations are solved in their finite volume method (FVM) discretized transient form, to each finite volume of the grid at each time step. Conservation of energy is discretized using upwind scheme, while conservation of mass is discretized by central differncing scheme. Conservation of *momentum* equations are discretized using a hybrid differencing scheme between central difference and upwind schemes. The temporal discretization of all equations is performed using a semi implicit scheme based on the fully implicit Euler scheme with explicit deferred correctors.

The algorithm PISO is used to solve pressure-velocity coupling iteratively each time step. The resulting set of equations is solved by the conjugate gradient method, using Cholesky method as conditioner.

Along with conservation equations, several submodel related equations are solved iteratively coupled each time step, in order to represent several phenomena occurring inside reactive flow field. They are organized in:

- Flow related submodels
- Spray related submodels
- Combustion related submodels

3.5.1 Flow related submodels

Turbulence modelling is performed using *RNG* $k-\varepsilon$ model, because it is recommended by literature (PERINI; MILES; REITZ, 2014; KHALILARYA; NEMATI et al., 2014; BERNI; CICALESE; FONTANESI, 2017) for Engine CFD-3D modelling as a good trade-off between quality of results and computational cost.

The equations of *RNG* $k-\varepsilon$ model, Equation 2.6 and Equation 2.7, are presented in subsection 2.1.3, and are solved coupled to the main conservation equations at the same iterative process. The constants used in those equations are described in (CD-ADAPCO, 2013).

3.5.2 Spray related submodels

Fuel injection inside CFD 3D Lagrangian domain is performed through injection of droplet packages described by Eulerian equations, as described in subsection 2.2.3. Droplet packages, named parcels, are transported through space carrying information about liquid fuel, have direction and initial velocity according to the type of injection, and also interact with surrounding media being decelerated by drag, transferring heat and mass. The droplets can also interact with engine walls, forming liquid film, and with other droplets, by collision and coalescence.

The fuel used at the engine experimental reference is commercial ethanol, as defined in the references (COSTA, 2017; NETTO, 2018). For this thesis, ethanol is modeled as liquid fuel injected directly at combustion chamber, with 6% in volume of water, which is in agreement with the definition of commercial ethanol described at (COSTA, 2017; NETTO, 2018). The air fuel ratio of ethanol with 6% of water is calculated based on the chemical equilibrium combustion of 1 mol of ethanol, with a calculated value of 8.427.

- First break-up

First break-up of the fuel jet is represented through statistic distribution of Rosin-Rammler in Equation 2.11, used to determine the diameter of the droplets inserted

inside flow field through statistical parameters. This is assumed because models for this phenomena usually present less quality results than this statistical formulation (BAUMGARTEN, 2006).

The values for the constants X and q are $3.7e^{-5}$ and 3.5, respectively, which have been adjusted to experimental data in previous research at CTM-UFMG.

- Second break-up

The model used to represent second break-up of fuel droplets is KHRT, as it is described in the commercial program manual (CD-ADAPCO, 2013). The values for the constants B_0, B_1, C_3, and C_τ are 0.61, 18.0, 2.0 and 1.0, which have been adjusted to experimental data in previous research at CTM-UFMG.

- Evaporation/drag

The correlation for droplet drag coefficient is Equation 2.12, and the correlation for droplet heat transfer coefficient, Equation 2.13, is the one proposed by El Wakil (WAKIL; UYEHARA; MYERS, 1954), which uses the correlation proposed by Ranz-Marshall, Equation 2.14, for the Nusselt number (RANZ; MARSHALL et al., 1952). All of those equations are used as they are described by the commercial program developer (CD-ADAPCO, 2013).

- Droplet-wall interaction

The injected fuel wall impingement phenomena is evaluated by a hybrid model available in the commercial program used (CD-ADAPCO, 2013), which is based in two different correlations available in literature (BAI; GOSMAN, 1995) and (ROSA et al., 2006).

- Colision/coalescence

In this work, it will not be used any model for both collision and coalescence, because according to literature (BAUMGARTEN, 2006), the models for this phenomena can not be validated directly in comparison to experimental results. It is also known as a best practice (CD-ADAPCO, 2013) that collision/coalescence models usually decrease the quality of the results.

3.5.3 Combustion related submodels

The model used to represent combustion is the Extended Coherent Flame Model for 3 Zones, or ECFM-3Z, described in section 2.2. This model is selected for its good trade-off between quality of results and computational cost. The adjustment parameters values are set to $\alpha = 1.6$ and $\beta = 1.0$ for all off the cases simulated.

3.6 BOUNDARY CONDITIONS

Boundary conditions for engine CFD 3D simulation are the main focus of this work. On one hand, there are the experimental data boundary conditions, for which the treatment of the available data is critical. On the other one, there are the not measured boundary conditions, which should use recommended values, literature values or either have some external model in order to provide values for those conditions.

There are two kinds of boundary surfaces in the engine domain: flow surfaces and wall surfaces. The presentation of boundary conditions follows this idea: first the boundary conditions for flow surfaces are presented, and latter the ones for wall surfaces.

3.6.1 Flow surfaces boundary conditions

There are only two flow surfaces in the simulation domain, as described in Figure 3.3, namely intake inflow and exhaust outflow. The locations of those surfaces represent in the simulation domain the position where pressure transducers are located in the engine test bench, both in intake and exhaust manifolds, which has already been highlighted in section 3.3. The relative position between the engine cylinder and the flow surfaces is described in Appendix A.

- Intake and exhaust pressure boundary conditions

Experimental data for intake and exhaust pressure, similar to the traces described in Figure 3.5, are used as boundary conditions at both flow surfaces.

Figure 3.5 – Example of experimental data for intake and exhaust pressure traces.

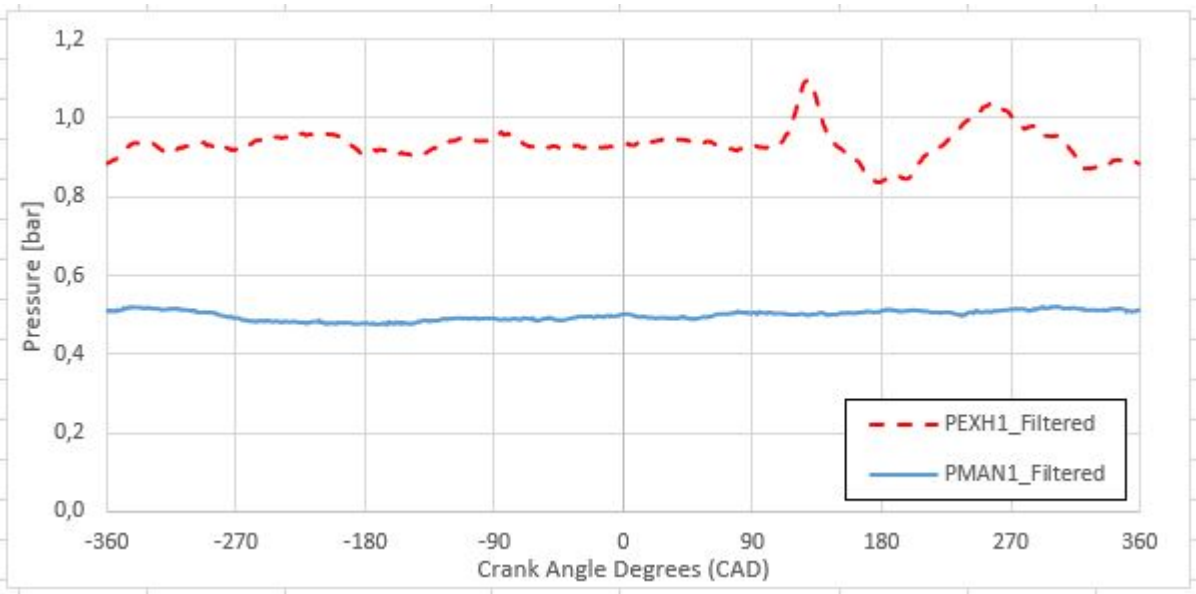

SOURCE: Elaborated by the author.

In Figure 3.5, experimental data for intake pressure trace (PMAN1_filtered) and exhaust pressure trace (PEXH1_filtered) are presented as their absolute values, and atmospheric

pressure is close to 0.9 [bar]. The engine operating condition is 1000 rpm 3 bar, which is one of the operating conditions evaluated in this thesis as described in section 3.2, Table 3.3. Those are intake and exhaust pressure traces for cycle 177, which is selected from 200 available cycles using cycle selection procedure described in subsection 3.8.1. Pressure experimental data are used as boundary conditions for equations of conservation of mass (Equation 2.1) and *momentum* (Equation 2.2, Equation 2.3 and Equation 2.4).

It is important to highlight that the best practice for intake pressure boundary condition is to directly use the intake pressure trace in Figure 3.5. Nevertheless this procedure is questioned in this thesis, and the implementation of intake pressure boundary condition is further discussed in section 3.8.

- Intake temperature boundary conditions

Gas temperature experimental data available in intake and exhaust manifolds are used as boundary conditions for conservation equation of energy (Equation 2.5). The gas temperature sensors in both intake and exhaust manifolds are not positioned at the same region as pressure transducers, so their location do not correspond exactly to the flow boundaries in the simulation domain. Nevertheless, once those values are the best representative ones for gas temperature at the flow boundaries of the domain, they are used as boundary conditions.

- Intake boundary conditions for turbulent intensity and turbulent length scale

Turbulent intensity is the boundary condition for the conservation equation of turbulent kinetic energy (Equation 2.6), and turbulent length scale is the boundary condition for the conservation equation of turbulent kinetic energy dissipation (Equation 2.7). Both of those quantities are not measured or modeled, so the values recommended by the developer of the engine CFD 3D commercial program are used.

3.6.2 Wall surfaces boundary conditions

For every wall surface of the domain, boundary condition for conservation equations of mass and conservation of species is the zero gradient condition.

- Near wall flow model

The Angelberger (ANGELBERGER; POINSOT; DELHAY, 1997) model is used as boundary condition for conservation equations of *momentum* (Equation 2.2, Equation 2.3 and Equation 2.4), turbulent kinetic energy (Equation 2.6) and turbulent kinetic energy dissipation (Equation 2.7). This model is referenced in literature (BERNI; CICALESE; FONTANESI, 2017) as a good trade off between quality of results and computational cost.

- Wall temperature - global HT model

Surface temperatures, calculated by the global heat transfer model presented in section 3.7, are used as boundary conditions for conservation of energy equation at every wall surface of the domain. The main reason for using those temperatures is the difficulty and experimental cost of measuring wall temperatures inside the engine, and the main reason for proposing a model for calculation of those temperatures are the influence of wall condition in the internal combustion engine physics, once all of the *phenomena* taking place are influenced by wall boundary condition.

3.7 GLOBAL HT MODEL

A one dimensional heat transfer model is used for calculating wall temperatures for different engine surfaces. It has not been found in literature any original paper, doctoral thesis or master degree dissertation using one dimensional heat transfer model for providing wall temperature values to be used as boundary conditions for engine CFD 3D modelling, therefore this methodology is considered unprecedented. Nevertheless, as it is shown in section 2.5, engine one dimensional heat transfer has been performed for several purposes, and thus the equations available in literature for other application are used as base for the proposed model.

Model in Figure 3.6 is a thermal resistance diagram, which illustrates heat transfer *phenomena* considered for the model used in this thesis, taking place inside the cylinder, and at intake and exhaust ports. This model is based in the global model proposed by (TORREGROSA et al., 2006), which used a thermal resistance network to calculate thermal energy diffusion inside one diesel engine. Temperature was calculated in 3 surfaces inside the cylinder, in such case cylinder head, cylinder liner and piston surfaces in contact with combustion chamber gases.

In the model proposed in Figure 3.6, surface temperatures are calculated for intake and exhaust ports and valves, aiming to expand surface temperature calculation in literature (TORREGROSA et al., 2006). The proposed model is considered a global one, based on the definition of wall to wall heat transfer approaches for internal combustion engines in section 2.4, once it provides one single value for each engine surface being modeled.

The solution of the proposed model provides the cycle average value of wall temperature, calculated for nine different surfaces, taking as boundary the temperatures of the in cylinder and exhaust hot gases, along with coolant, lubricating oil and intake cold gases. The surface temperatures calculated by the proposed model and their correlation to Figure 3.6 are presented in Table 3.8, and the boundary temperatures are presented in Table 3.9.

The model has been implemented in a commercial code devoted to solution of sets of equations, in case, the software EES. The calculation of wall temperatures depends:

- on gas temperature, heat transfer coefficient and other parameters of the phenomena taking place inside the cylinder, at intake and exhaust ports;

Figure 3.6 – Thermal resistance diagram for global heat transfer model.

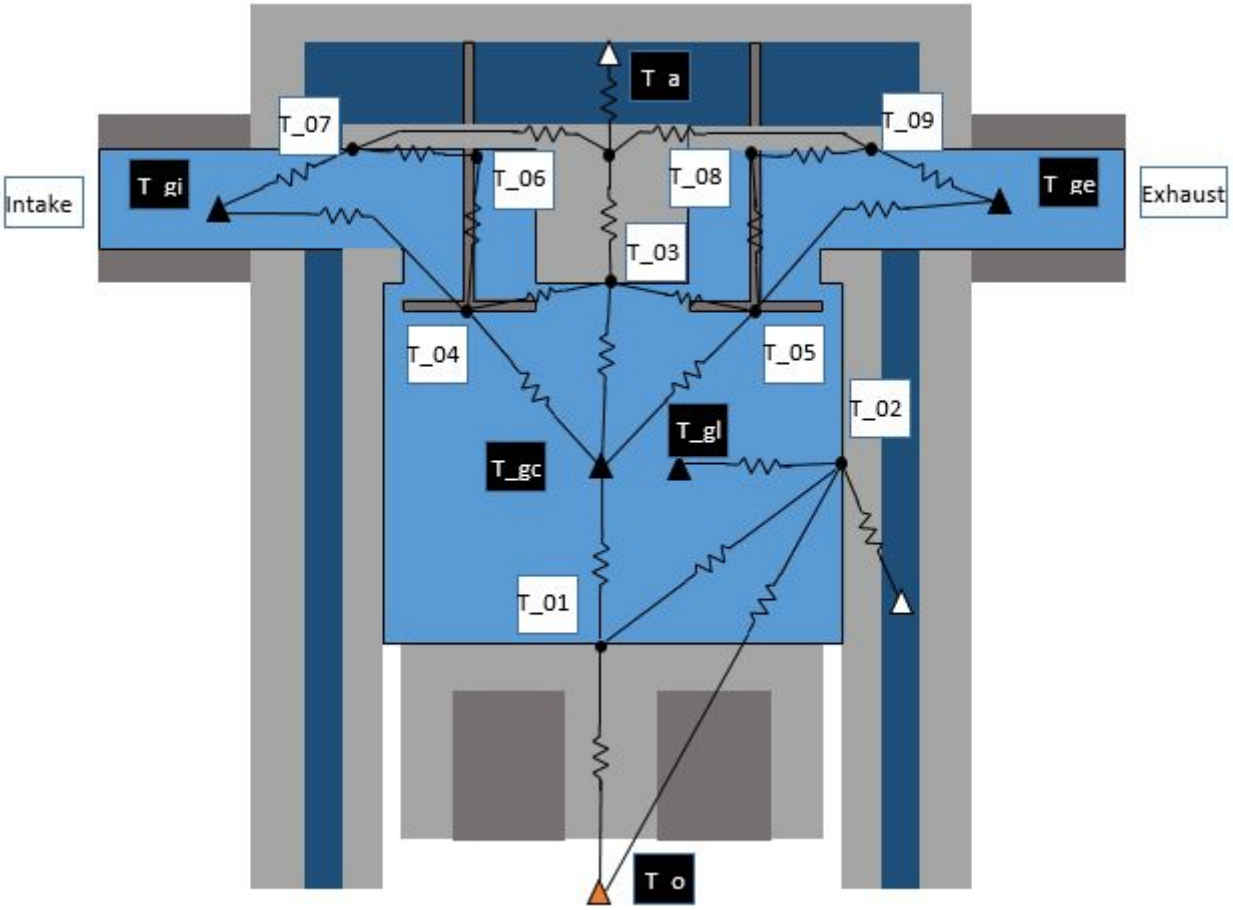

SOURCE: Elaborated by the author.

Table 3.8 – Surface temperatures calculated by the proposed global heat transfer model.

T_01	Piston
T_02	Cylinder liner
T_03	Cylinder head
T_04	Intake valve face
T_05	Exhaust valve face
T_06	Intake valve stem
T_07	Intake port
T_08	Exhaust valve stem
T_09	Exhaust port

- on the oil film flow inside the cylinder and through the piston galleries;
- on the coolant flow conditions at cylinder head and cylinder block;
- on the contact between piston and cylinder liner.

The global heat transfer model proposed in Figure 3.6 is based on the following assumptions:

Table 3.9 – Boundary conditions for the global heat transfer model.

T_gc	In cylinder gas temperature, combustion chamber
T_gl	In cylinder gas temperatures, cylinder liner
T_gi	Intake gas flow
T_ge	Exhaust gas flow
T_a	Coolant
T_o	Lubricating oil
T_09	Exhaust port

1. The different heat transfer phenomena can be modeled as a group of one dimensional heat transfer circuits;

2. Each thermal resistance is evaluated for steady state operation;

3. The major part of the heat rejected by the engine is driven by the coolant flow and oil heat exchangers, at the engine test bench described in section 3.2;

The following phenomena are neglected, all of them according to assumption number 3:

- The heat transfer from the engine outside surface to the test bench parts;
- The heat transfer from engine head towards intake and exhaust manifolds;
- The radiation from the engine outside to the test bench walls

The proposed HT model provides boundary conditions for engine CFD 3D model, in case the temperatures in Table 3.8, but the information which is input to this HT model is taken from engine CFD 3D model, for example, in cylinder gas temperature, intake and exhaust gas temperatures, heat transfer coefficients from gas flows to wall regions all over the domain. This means both models should be used in an iterative way. For the second iteration and ahead, CFD 3D results for in cylinder mean gas temperature and heat transfer coefficient for piston, cylinder liner, cylinder head, valve faces, valve stems and ports surfaces are used as inputs, along with measured values for coolant and oil temperature from engine test bench descibed in section 3.2. For the first iteration, a set of semi empirical correlations is proposed for providing a first attempt of wall temperatures, based on measured water temperature, oil temperature and in cylinder pressure, along with modeled in cylinder temperature. In the following sub sections, the correlations used for the first iteration of the HT model are presented in subsection 3.7.1 through subsection 3.7.13.

3.7.1 Heat transfer between gases and cylinder liner

Heat transfer between in cylinder gases and cylinder liner surface is solved similar to literature (TORREGROSA et al., 2006), calculating heat transfer coefficient for in cylinder gases h_{gas}, thermal conductance between in cylinder gases and cylinder liner surface $K_{gas-lin}$

and temperature of in cylinder gases as it is seen from cylinder liner surface $T_{gas-lin}$ using Equation 3.3, Equation 3.4 and Equation 3.5:

$$h_{gas} = 0.012 D_{cyl}^{-0.2} T^{-0.53} p^{0.8} \left(C_{w1} S_p + C_{w2} C_u + C_2 \frac{V_D T_{ivc}}{p_{ivc} V_{ivc}} (p - p_m) \right)^{0.8} \tag{3.3}$$

$$K_{gas-lin} = \frac{1}{720} \int_0^{720} h_{gas}(\alpha) A_{cyl}(\alpha) d\alpha \tag{3.4}$$

$$T_{gas-lin} = \frac{\int_0^{720} T_{gas}(\alpha) h_{gas}(\alpha) A_{cyl}(\alpha) d\alpha}{\int_0^{720} h_{gas}(\alpha) A_{cyl}(\alpha) d\alpha} \tag{3.5}$$

According to Equation 3.3, Equation 3.4 and Equation 3.5, $K_{gas-lin}$ and $T_{gas-lin}$ are cycle average values and h_{gas} is an instantaneous value, which depends on instantaneous values of in cylinder pressure p, temperature T and motoring pressure p_m. Equation 3.3 is the Woschni equation (WOSCHNI, 1967) for the heat transfer coefficient h_{gas} between in cylinder gases and in cylinder walls considering isothermal wall approximation, as it is used by (TORREGROSA et al., 2006).

The solutions of Equation 3.4 and Equation 3.5 in this thesis are performed using a table of values for p, T and p_m from experimental data, from -360 CAD to 360 CAD with an interval of 1 CAD, making it a 721 lines table, and for each table line a value for h_{gas} is calculated. The cycle average values for $K_{gas-lin}$ and $T_{gas-lin}$ are then calculated, considering the complete 721 lines table using Equation 3.4 and Equation 3.5.

Another important parameter in both Equation 3.4 and Equation 3.5 is $A_{cyl}(\alpha)$, which is the instantaneous cylinder liner area exposed to in cylinder gases. The proposed model follows the literature (TORREGROSA et al., 2006) and calculates heat transfer coefficient h_{gas} and instantaneous exposed cylinder liner area $A_{cyl}(\alpha)$ for each table line, in such a manner that the integral values of $K_{gas-lin}$ and $T_{gas-lin}$ calculated by Equation 3.4 and Equation 3.5 consider the variation of the cylinder liner area exposed to in cylinder gases.

It is also important to highlight that the proposed model is a thermal resistance one, this way no transient calculation is performed, once no thermal capacitance is considered. This use of instantaneous parameters is only part of the cycle average calculations performed by Equation 3.4 and Equation 3.5. Another important information is that h_{gas} presents significant variation between different engine operating conditions in Table 3.3, once it is a function of p, T and p_m, provided by experimental data.

3.7.2 Heat transfer between gases and piston

Heat transfer between in cylinder gases and piston surface is solved calculating heat transfer coefficient for in cylinder gases h_{gas}, thermal conductance between in cylinder gases

and piston surface $K_{gas-pis}$ and temperature of in cylinder gases as it is seen from piston surface $T_{gas-pis}$ using Equation 3.3, Equation 3.6 and Equation 3.7 (TORREGROSA et al., 2006):

$$K_{gas-pis} = A_{pis} \frac{1}{720} \int_0^{720} h_{gas}(\alpha) d\alpha \tag{3.6}$$

$$T_{gas-pis} = \frac{\int_0^{720} T_{gas}(\alpha) h_{gas}(\alpha) d\alpha}{\int_0^{720} h_{gas}(\alpha) d\alpha} \tag{3.7}$$

According to Equation 3.6 and Equation 3.7, $K_{gas-pis}$ and $T_{gas-pis}$ are cycle average values, which are calculated in a similar way to $K_{gas-lin}$ and $T_{gas-lin}$ in Equation 3.4 and Equation 3.5. In both Equation 3.6 and Equation 3.7, h_{gas} is heat transfer coefficient between in cylinder gases and in cylinder walls considering isothermal wall approximation, as it is described in subsection 3.7.1.

The most important difference between piston heat transfer in this section and cylinder liner heat transfer in subsection 3.7.1 is that piston surface area A_{pis} is constant, as it is seen from in cylinder gases, meanwhile cylinder liner surface changes throughout the cycle, as already explained in previous subsection.

Thus, the proposed model calculates heat transfer between in cylinder gases and piston surface in a similar way to heat transfer between in cylinder gases and cylinder liner. The same values of h_{gas}, calculated in subsection 3.7.1 from p, T and p_m 721 lines table from -360 CAD until 360 CAD with an interval of 1 CAD, are used to provide cycle average values for $K_{gas-pis}$ and $T_{gas-pis}$.

3.7.3 Heat transfer between gases and cylinder head

Heat transfer between in cylinder gases and cylinder head surface is solved similar to literature (TORREGROSA et al., 2006), calculating heat transfer coefficient for in cylinder gases h_{gas}, thermal conductance between in cylinder gases and cylinder head surface $K_{gas-head}$ and temperature of in cylinder gases as it is seen from cylinder head surface $T_{gas-head}$ using Equation 3.3, Equation 3.8 and Equation 3.9:

$$K_{gas-head} = A_{head} \frac{1}{720} \int_0^{720} h_{gas}(\alpha) d\alpha \tag{3.8}$$

$$T_{gas-head} = \frac{\int_0^{720} T_{gas}(\alpha) h_{gas}(\alpha) d\alpha}{\int_0^{720} h_{gas}(\alpha) d\alpha} \tag{3.9}$$

According to Equation 3.8 and Equation 3.9, $K_{gas-head}$ and $T_{gas-head}$ are cycle average values, which are calculated in a similar way to $K_{gas-pis}$ and $T_{gas-pis}$ in Equation 3.6 and Equation 3.7. Indeed, Equation 3.9 is equal to Equation 3.7 and the only difference between Equation 3.8 and Equation 3.6 is the change between cylinder head area exposed to in cylinder gases, A_{head}, and piston surface are exposed to in cylinder gases, A_{pis}.

The heat transfer between in cylinder gases and cylinder head surface exposed area is resolved similar to what is described in subsection 3.7.1 and subsection 3.7.2. The same values of h_{gas}, calculated in subsection 3.7.1 from p, T and p_m 721 lines table from -360 CAD until 360 CAD with an interval of 1 CAD, are used to provide cycle average values for $K_{gas-head}$ and $T_{gas-head}$.

3.7.4 Heat transfer between gases and valve faces

Heat transfer between in cylinder gases and valve faces is solved calculating heat transfer coefficient for in cylinder gases h_{gas}, thermal conductance between in cylinder gases and valve faces $K_{gas-valv}$ and temperature of in cylinder gases as it is seen from valve faces $T_{gas-valv}$ using Equation 3.3, Equation 3.10 and Equation 3.11 (TORREGROSA et al., 2006):

$$K_{gas-valv} = A_{valv} \frac{1}{720} \int_0^{720} h_{gas}(\alpha) d\alpha \tag{3.10}$$

$$T_{gas-valv} = \frac{\int_0^{720} T_{gas}(\alpha) h_{gas}(\alpha) d\alpha}{\int_0^{720} h_{gas}(\alpha) d\alpha} \tag{3.11}$$

Valve face area exposed to in cylinder gases is constant, similar to cylinder head and piston surface area, this way, Equation 3.10 and Equation 3.11 description are similar to the ones for Equation 3.6 and Equation 3.7 in subsection 3.7.2.

3.7.5 Heat transfer through valves

Heat transfer through valves is performed by splitting each valve into a small number of nodes, in case two nodes at valve plate and four nodes at valve stem. The discrete heat transfer equation is solved by finite difference method, between the different valve nodes in contact. The valve tip is considered adiabatic, in the sense that all of the heat flux trough the valves is driven to the cylinder head coolant flow, or some part to the intake gases in the case of intake valve. The boundary condition for each node depends on its location, and the following subsections describe the valve heat transfer boundary conditions.

3.7.6 Heat transfer between valves and cylinder head

The heat transfer between valves and cylinder head is modeled using contact conductance's for two regions. The first contact conductance is from valve plate to cylinder head trough valve seat. The contact conductance is estimated at 7000 W/m^2K (CERDOUN; CARCASCI; GHENAIET, 2016; JEEVANASHANKARA; MADHUSUDANA; KULKARNI, 1990) for both intake and exhaust valves, from valve plate to cylinder head. The second contact conductance is from valve stem to cylinder head trough valve guide. The contact conductance is estimated at 5000 W/m^2K (JEEVANASHANKARA; MADHUSUDANA; KULKARNI, 1990) for both intake and exhaust valves, from valve stem to cylinder head.

3.7.7 Heat transfer between valve stem and gas flow

Heat transfer between port gas flows and valve stem surfaces is calculated by the combination of two correlations, similar to (CERDOUN; CARCASCI; GHENAIET, 2016): one correlation for the flow past a cylinder, and the other one for the flow past a flat plate.

Heat transfer from valve stem to port gas flow, for the stem modeled as a cylinder, is calculated by Equation 3.12 (INCROPERA et al., 2007):

$$Nu_{cylinder} = 0.3 + \frac{0.62Re^{1/2}Pr^{1/3}}{[1+(0.4/Pr)^{2/3}]^{1/4}}\left[1+\left(\frac{Re}{282,000}\right)^{5/8}\right]^{-4/5} \tag{3.12}$$

Heat transfer from valve stem to port gas flow, for the stem modeled as a flat plate, is calculated by means of Equation 3.13 (INCROPERA et al., 2007):

$$Nu_{flatplate} = 0.037Re^{4/5}Pr^{1/3} \tag{3.13}$$

The heat transfer coefficient between valve stem and port gas flow is calculated by means of Equation 3.14, which is a combination of cylinder and flat plate approaches (CERDOUN; CARCASCI; GHENAIET, 2016).

$$h_{stemgas} = \varepsilon_{cyl}h_{cylinder} + (1-\varepsilon_{cyl})h_{flatplate} \tag{3.14}$$

The weighting factor ε_{cyl} in Equation 3.14 is a function of the angle between valve stem and the flow past it, and is directly associated to the component of the flow normal to the valve stem axial direction, which is related to the flow past a cylinder approximation. Once the angle between the valve stem and the flow past it is a result of the engine CFD 3D calculation, a value of 0.5 is used for ε_{cyl} in this thesis, as a first approach.

3.7.8 Heat transfer between gases and ports

Heat transfer between gas flows and walls at intake and exhaust ports is calculated in a similar way to literature (BOHAC; BAKER; ASSANIS, 1996; PIEDRAHITA, 2009). Sleicher and Rouse correlation is used to calculate Nusselt number $Nu_D(x=\infty)$ in internal turbulent flow fully developed:

$$Nu_D(x=\infty) = 5 + 0.015Re_{D,f}^{a}Pr_w^{b} \tag{3.15}$$

In Equation 3.15, $a = 0.83$ and $b = 0.66$. The correction for a given flow with pipe length less than entrance length is calculated using Equation 3.16:

$$\frac{Nu_D(x)}{Nu_D(x=\infty)} = 1 + \frac{2}{(x/D_{port})} \tag{3.16}$$

In Equation 3.16, D_{port} is port diameter or hydraulic diameter and x is port length. Correction for curvature effects is calculated using Equation 3.17:

$$\frac{h_{portcurv}}{h_{straighttube}(x=\infty)} = 1 + 3.5\frac{D_{port}}{D_{curv}} \tag{3.17}$$

In Equation 3.17, D_{port} is port diameter or hydraulic diameter and D_{curv} is port curvature diameter. Equation 3.15 through Equation 3.17 are used for resolving both intake and exhaust port heat transfer, similar to what is done in literature.

3.7.9 Heat transfer between combustion chamber surface, ports surfaces and coolant

Heat transfer inside engine head, between combustion chamber surface, intake and exhaust ports surfaces and coolant flow is solved in a coupled form. In the model described at Figure 3.6, the surface of engine head in contact with coolant flow is considered isothermal, for it is in contact with the most important heat sink. Nevertheless, combustion chamber, intake and exhaust ports surfaces are at different temperatures.

They are represented by a thermal circuit composed by three surfaces at different temperatures, namely combustion chamber, intake and exhaust ports, exchanging heat to one single surface at the same temperature, namely engine head coolant gallery surface.

- Heat transfer between combustion chamber surface and coolant gallery surface

Heat transfer between combustion chamber surface and coolant gallery surface is solved by calculating thermal conductance K_{cc-gal} using Equation 3.18, which represents heat transfer by conduction through engine head wall between combustion chamber surface and coolant gallery surface:

$$K_{cc-gal} = \frac{k_{cc}A_{cc}}{e_{cc}} \tag{3.18}$$

- Heat transfer between intake port surface and coolant gallery surface

Heat transfer between intake port surface and coolant gallery surface is solved by calculating thermal conductance $K_{int-gal}$ using Equation 3.19, which represent heat transfer by conduction through engine head wall between intake port surface and coolant gallery surface:

$$K_{int-gal} = \frac{k_{int}A_{int}}{e_{int}} \tag{3.19}$$

- Heat transfer between exhaust port surface and coolant gallery surface

Heat transfer between exhaust port surface and coolant gallery surface is solved by calculating thermal conductance $K_{exh-gal}$ using Equation 3.20, which represent heat transfer

by conduction through engine head wall between intake port surface and coolant gallery surface:

$$K_{exh-gal} = \frac{k_{exh} A_{exh}}{e_{exh}} \tag{3.20}$$

- Heat transfer between cooling gallery surface and coolant flow

Heat transfer between coolant gallery surface and coolant flow is solve by calculating thermal conductance $K_{gal-cool}$ using Equation 3.21, which represent heat transfer by forced convection and nucleate boiling between coolant gallery surface and coolant flow.

$$K_{gal-cool} = h_{gal-cool} A_{gal} \tag{3.21}$$

- Properties and geometry values

Heat transfer coefficient $h_{gal-cool}$ in Equation 3.21 is considered as the value of 4,900 $[W/m^2K]$, which is the one proposed by (TORREGROSA et al., 2006) for convective heat transfer between combustion chamber and coolant flow. Geometry values for A_{cc} and e_{cc} in Equation 3.18, A_{int} and e_{int} in Equation 3.19, A_{exh} and e_{exh} in Equation 3.20, along with A_{gal} in Equation 3.21 are used from geometry CAD files as described in Figure 3.2. This is possible for the availability of engine information stated in section 3.2, like CAD files, which proved this engine the correct selection. Material properties for k_{cc}, k_{int}, k_{exh}, which are thermal conductivities for the engine head material at different regions, are taken from software EES libraries based on NIST tables, which is one of the main reasons for selecting this program at the first attempt of this model.

3.7.10 Heat transfer between cylinder and coolant

Heat transfer between cylinder liner surface and coolant is solved calculating thermal conductance between cylinder liner and coolant $K_{lin-cool}$ using Equation 3.22, proposed by (TORREGROSA et al., 2006):

$$K_{lin-cool} = \left(\frac{ln\left(\frac{D_{cyl}+2e_{lin}}{D_{cyl}}\right)}{2.\pi.S_{cyl}.k_{cyl}} + \frac{1}{A_{lin,ext} h_{lin-cool}} \right)^{-1} \tag{3.22}$$

Equation 3.22 represents series association between thermal resistances for conduction at cylinder wall and forced convection plus nucleate boiling between cylinder external wall and coolant flow. The value for heat transfer coefficient $h_{lin-cool}$ is 4,800 $[W/m_2K]$ according to (TORREGROSA et al., 2006). Geometry values for e_{lin} and $A_{lin,ext}$ are taken from the geometry CAD files as described in Figure 3.2, and material properties for k_{cyl} are taken from software EES libraries based in NIST tables, for the same reasons highlighted in subsection 3.7.9.

3.7.11 Heat transfer between cylinder and oil

Heat transfer between cylinder liner surface and oil film is solved calculating thermal conductance between cylinder liner and oil $K_{lin-oil}$ using Equation 3.23, proposed by (TORREGROSA et al., 2006):

$$K_{lin-oil} = \pi D_{cyl} S_{cyl} h_{lin-oil} \tag{3.23}$$

3.7.12 Heat transfer between piston and oil

Heat transfer between piston surface and oil flow through piston is solved calculating thermal conductance between piston and oil using, proposed by (TORREGROSA et al., 2006):

$$K_{pis-oil} = \pi^2 D_{gal} (d_{gal})^m C'_{gal} (S_p)^m \tag{3.24}$$

3.7.13 Heat transfer between piston and cylinder

Heat transfer between piston surface and cylinder liner surface is solve calculating thermal conductance between piston and linder using, proposed by (TORREGROSA et al., 2006):

$$K_{pis-lin} = \left(\frac{ln\left(\frac{D_{pis}}{0.5D_{pis}}\right)}{2.\pi.h_{pc}.k_{pis}} + \frac{1}{\pi D_{cyl} h_{pc} h_{pis-lin}} \right)^{-1} \tag{3.25}$$

3.8 SIMULATION METHODOLOGY

In this section, the steps executed to perform each of the simulation cases described in Table 3.3 are presented.

First step is the selection of the engine, for which the single cylinder research engine at CTM-UFMG is selected, as described in section 3.2. Along with this step, the geometry of the engine is treated as described in section 3.3.

Second step is the treatment of experimental data measured at test bench, in order to use either as boundary conditions or as validation reference.

3.8.1 Cycle selection procedure

This is the procedure to select the cycle to take experimental data for boundary conditions and for verification of numerical results. For each engine operating condition, the average in cylinder pressure trace is calculated based on the total number of cycles, and for each cycle three parameters are calculated: maximum difference pressure, minimum difference pressure and average difference pressure.

Maximum difference pressure is the absolute value of the maximum positive difference between one given cycle and the average cycle. Minimum difference pressure is the absolute value of the maximum negative difference between one given cycle and the average cycle. Average difference is the sum of the differences between one given cycle and the average cycle for each measured instant, over the total number differences calculated.

The quality criteria is defined by experience, in order to select the cycle that best fits simultaneously the three parameters: 0.5 bar for maximum pressure, 0.5 bar for minimum pressure, and 0.05 bar for average pressure. Once this filter is applied, just a few or none cycles should be highlighted, attending simultaneously to the three parameters. If more than 3 cycles are highlighted, or none cycle is highlighted, the filter can be slightly adjusted in order to reduce the number of highlighted cycles. The selected cycle is the one that best fits the three parameters simultaneously.

After executing the cycle selection procedure, the following experimental data is obtained from the selected cycle: IMEP, in cylinder pressure, intake and exhaust pressure, motoring pressure, in cylinder temperature.

3.8.2 Intake pressure correction

It is observed in the results presented in section 4.1 that engine CFD 3D results for all of the selected operating conditions cannot reproduce experimental data for lambda. Considering as reference the experimental data for lambda, fuel mass flow, engine speed and injection time, along with equivalence ratio for ethanol with 6% of water, it is calculated the trapped mass of air based on experimental data, and for all cases the engine CFD 3D values for trapped mass of air exceed more than 20% the experimental data ones, which is named systematic excess of air.

Several attempts and lots of computational time have been spent in order to correct this effect without changing measured boundary conditions, but no success has been obtained. The only way to make engine CFD 3D trapped mass of air equal to experimental data is reducing intake pressure boundary condition. But by doing this, one would be changing the measured data, and missing accuracy for its model.

The basis for reducing the intake pressure comes from literature review in section 2.3 and subsection 2.5.2, where it is observed that one of the main effects of pulsating flow in intake ducts of reciprocating internal combustion engines is the reduction of volumetric efficiency (HANRIOT; QUEIROZ; MAIA, 2019; SOUZA et al., 2019). It is also observed in literature review that most of the engine CFD 3D model papers do not identify the excess of air, do not evaluate volumetric efficiency (MILLO et al., 2014; ROBERT et al., 2015; TOOSI; FAROKHI; MASHADI, 2015; FAN et al., 2018), or perform closed cycle engine CFD 3D where no intake flow is modelled (BUHL et al., 2017; MASOULEH et al., 2018).

It is implicit in this review that engine CFD 3D models using RANS approach for turbulence do not capture the effects of pulsating flow in terms of reducing the volumetric efficiency, which is considered in this thesis to produce systematic excess of air inside the

cylinder. This is only affirmed because no paper in literature has been found to evaluate the capabilities of engine CFD 3D models, either using RANS, LES or DNS, in terms of capturing trapped mass of air. Moreover, no paper in literature has been found in order to quantify the frequencies occurring at intake pulsating flow for which CFD 3D models are able to capture average mass flow *phenomena* in comparison to experimental data.

For this reason, in this thesis, it is not possible to reproduce experimental data for lambda and trapped mass of air using intake pressure boundary conditions experimental data, once the proposed engine CFD 3D model uses RANS approach, and can not capture the effect of pulsating flow at intake ducts over volumetric efficiency. It is not possible also to evaluate the frequencies of intake pulsating flow for which a given engine CFD 3D model produces accurate result for lambda and trapped mass of air, using LES or DNS approaches, for the given computational resources and time.

The only way to reproduce trapped mass of air inside the cylinder is to reduce intake pressure, in order to correct engine CFD 3D trapped mass of air for each engine operation condition. This way, pressure reduction performed in all cases is considered intake pressure correction for pulsating flow effect over volumetric efficiency at intake ducts. The correction of intake pressure due to effects of pulsating flow over volumetric efficiency in engine CFD 3D models has not been found in literature, and thus it is unprecedented.

- Intake pressure correction procedure

The intake pressure correction procedure is performed by executing the following steps for a given engine operating condition. The intake pressure trace selected is averaged, and the average intake pressure is used as boundary condition for engine CFD 3D simulation. The engine condition runs for 3 cycles, and the CFD 3D result for trapped mass of air using experimental intake pressure boundary condition is calculated and compared to the trapped mass of air calculated based on experimental data. The relative difference between CFD 3D and experimental data for trapped mass of air is applied as a pressure reduction, in order to reduce mass air flow.

The reduced intake pressure is used as boundary condition for engine CFD 3D simulation. The case runs for 3 cycles, and the CFD 3D result for trapped mass of air using reduced pressure is calculated and compared to both trapped mass of air for experimental data and for CFD 3D model using experimental data for intake pressure.

A first order interpolation in therefore applied for intake pressure, using as reference experimental data for trapped mass of air and both trapped mass of air calculated by CFD 3D model for experimental data intake pressure and reduced intake pressure. The interpolated pressure is the fitted pressure boundary condition for the given engine operating condition, and the trapped mass of air calculated by engine CFD 3D model using this fitted pressure should produce the correct lambda for the given engine operating condition.

3.8.3 Global heat transfer and engine CFD 3D iteration

Using the fitted pressure, the evaluated engine operating condition runs for three cycles, and the results of the third cycle are used as intake data for the second iteration of the global heat transfer model described at section 3.7. The global heat transfer model calculates wall temperature boundary condition for a second iteration, and these wall temperature values are compared to the first iteration values.

If any difference is greater than the convergence criteria, the engine CFD 3D model should run another iteration. For this thesis, the convergence criteria is defined as 5%.

The engine CFD 3D model runs three cycles using second iteration wall temperatures, and the results are once more extracted and used at global heat transfer model. The temperatures for third iteration are calculated, and if any difference is greater than the convergence criteria, the engine CFD 3D model run another iteration. If all differences are smaller than the convergence criteria, than the decoupled iterative process between engine CFD 3D model and global HT model is considered converged, and the previous global HT iteration results are considered the wall temperature for the given engine operating condition.

3.8.4 Block diagram of the simulation methodology

The simulation methodology is illustrated in Figure 3.7. In this figure, the workflow implemented for each engine operating condition evaluated at this thesis is described, considering the steps described in subsection 3.8.1, subsection 3.8.2 and subsection 3.8.3. The inputs for the procedure described at Figure 3.7 are the grid selected by the grid dependence study in section 3.4, one of the engine operating conditions described at Table 3.3 along with all of the experimental data available, and the global heat transfer model described at section 3.7.

The methodology described at Figure 3.7 is performed for all of the six different engine operating conditions at Table 3.3, in such a manner that the engine CFD 3D model is used always with the same values for the constants associated to all of the submodels described in section 3.5.

3.9 PRESENTATION OF RESULTS

The results are presented in the following sequence. All of the results presented for the engine CFD 3D model are results obtained at the third cycle.

First, the results obtained by the engine CFD 3D model using experimental data for intake pressure boundary conditions are presented, in terms of injected mass of fuel, trapped mass of air and lambda. The model results are always compared to experimental correlated data. In terms of lambda, the experimental value is directly measured, meanwhile for both injected mass of fuel and trapped mass of air the experimental value is calculated based on experimental

Figure 3.7 – Simulation methodology block diagram, comprising the decoupled iterative method between engine CFD 3D and global HT models.

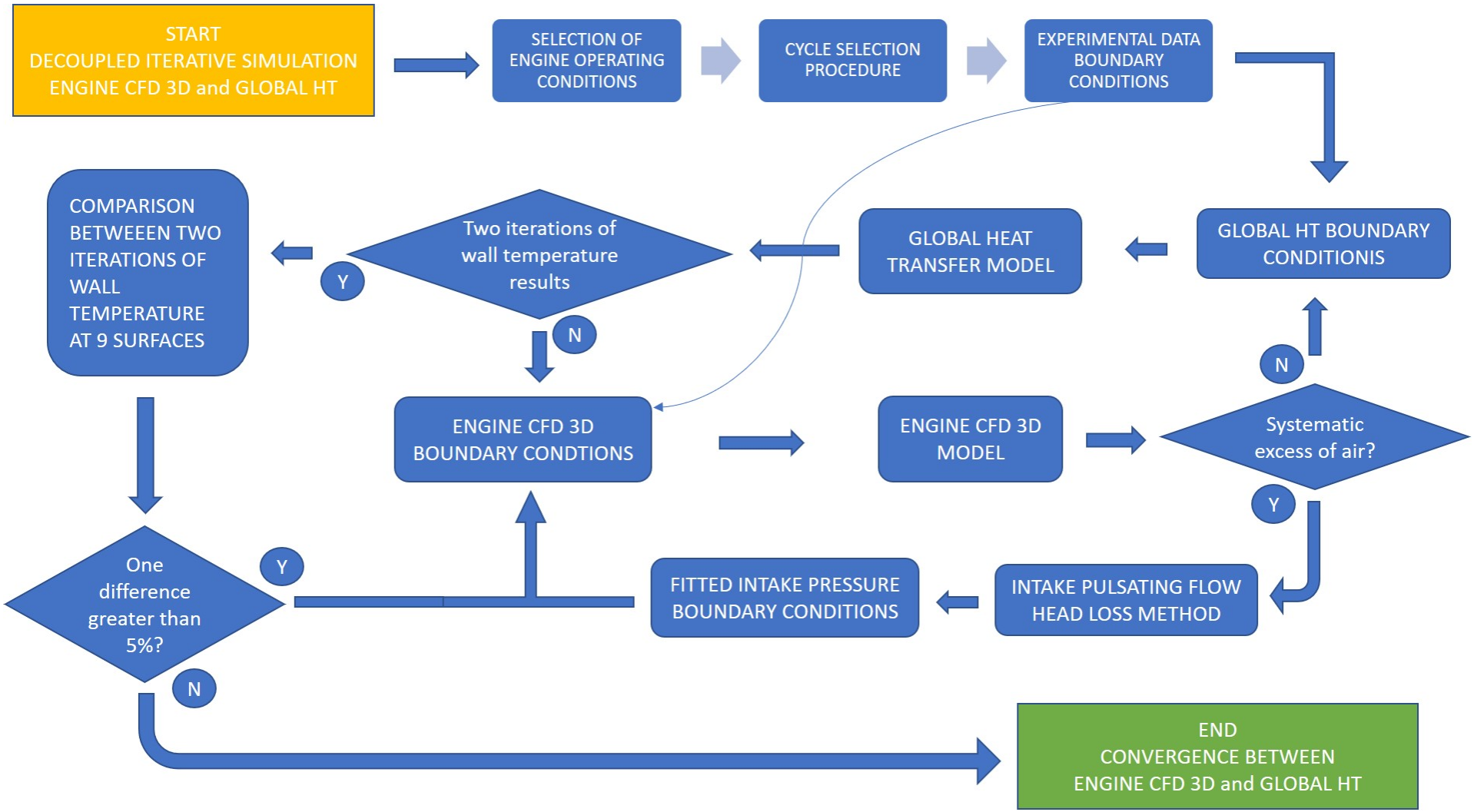

SOURCE: Elaborated by the author.

data. It is intended to describe the consequence of using experimental data as intake pressure boundary conditions at engine CFD 3D models using RANS approach for turbulence.

Just after the results obtained using experimental boundary conditions, it is presented the hypothesis proposed in this thesis to explain the systematic excess of air observed for all of the engine operating conditions evaluated. This hypothesis is the greatest contribution of this thesis to the state of the art concerning engine CFD 3D modelling, independently of the turbulence modelling approach. Along with this hypothesis, it is presented the methodology proposed in this thesis, which is unprecedented, to represent the effects of pulsating flow over volumetric efficiency calculating a pulsating flow head loss, based on the trapped mass of air calculated by the engine CFD 3D model.

Then, the results for pressure correction procedure are presented, for all of the engine operating conditions. The pressures calculated by the pressure correction procedure are named here fitted pressure, in order to difference experimental pressure intake boundary conditions from fitted pressure intake boundary conditions.

The results for the global heat transfer model are presented for first and second iterations for all of the engine operating conditions, and for second and third iterations for three selected engine conditions, namely 1000 rpm 3 bar, 2000 rpm 3 bar and 2000 rpm 8 bar. The presentation of third iteration global heat transfer results is performed for selected engine operating conditions due to lack of available time, once the implementation of this third iteration of global heat transfer model demands as input the results from engine CFD 3D model results using second iteration wall temperatures. The computational cost for each case made it only possible to run those engine CFD 3D results using second iteration wall temperatures for the selected engine operating conditions. The results for the global heat transfer model are presented along with the difference between iterations for each surface temperature calculated, in order to evaluate the convergence of the global heat transfer model.

After the results for the heat transfer model, the results obtained by the engine CFD 3D model using first iteration of wall temperature values are presented for all of the engine operating conditions evaluated, in terms of injected mass of fuel, trapped mass of air, lambda, IMEP and peak pressure. It is intended to describe the results obtained by the proposed methodology for pressure correction based on the pulsating flow head loss concept, for all of the evaluated engine operating conditions evaluated.

The results obtained by the engine CFD 3D model using second iteration of wall temperature values are presented for three selected engine operating conditions, due to the high computational cost associated to the simulation of six different engine operating conditions using an engine CFD 3D model. The results are presented in terms of injected mass of fuel, trapped mass of air, lambda, IMEP and peak pressure. It is intended to describe the results obtained by the proposed heat transfer model using second iteration wall temperatures.

After presenting all of the results for several engine operating conditions simultaneously, for different sets of boundary conditions, namely experimental and fitted

intake pressure, first and second iteration of global heat transfer model, comparing the different engine operating conditions, the results obtained at selected engine conditions are presented comparing the different sets of boundary conditions used.

The results for selected engine operating conditions are: in cylinder pressure traces obtained by the different boundary conditions compared to experimental results, considering four different presentations, one for the total engine cycle, on exclusive for the intake and compression strokes, another one for the expansion and exhaust strokes, and a last one for specific for the combustion analysis interval. In those four charts, a pressure envelope is presented for the in cylinder experimental pressure, which is obtained by the evaluation of the maximum and minimum in cylinder pressure values at each instant of the cycle, obtained by experimental values.

Also, results for the pressure volume diagram are presented, along with the diagram comparing pressure logarithm and volume logarithm. Finally, results for in cylinder temperature are presented. The main objective of all of the charts presented is to qualitatively compare the results obtained by the proposed methodology with the ones obtained by experimentally measured pressure boundary conditions, and this way to describe the increase in accuracy obtained by the use of the proposed methodology for each engine condition evaluated.

The presentation of the results is finished with a section highlighting the most important achievements of the methodology proposed, in comparison to the results obtained by the use of experimentally measured intake pressure boundary conditions. This way, it is proved the use of the proposed methodology to achieve the proposed objectives.

3.10 METHODOLOGY FINAL REMARKS

The proposed methodology contributes in an unprecedented manner to the state of the art concerning engine CFD 3D modelling on the following topics:

- Identification and declaration of systematic excess of air for six different engine operating conditions of a given naturally aspired engine, as a result of the engine CFD 3D model using experimental data for intake pressure boundary condition;
- Presentation of a hypothesis to justify the systematic excess of air observed, related to intake duct pulsating flow effect over engine volumetric efficiency;
- Proposition of a method to modify intake pressure, in order to meet experimental data for trapped mass of air, an thus to attend to experimental data for lambda;
- Proposition of a method to calculate iteratively decoupled wall temperatures to be used as boundary conditions of the engine CFD 3D model;

- Proposition of a simulation methodology to treat boundary conditions of intake pressure and wall temperature;
- Proposition of a simulation methodology to verify the effect of the proposed boundary conditions treatment on the accuracy of engine CFD 3D model, for different engine operating boundary conditions using the same values for sub model constants;
- Proposition of a simulation methodology to modify intake pressure boundary conditions, and calculate wall temperature boundary condition, in order to obtain accurate results from engine CFD 3D model at different engine operating conditions using the same values for sub models constants

The proposed simulation methodology should be capable of performing interpolation and extrapolation tasks, after the proposition and validation of interpolation and extrapolation methodologies, which is not possible for the actual models, which are in general validated for a single engine operating conditions, after tuning the constants of some sub model.

4 RESULTS AND DISCUSSION

The results are presented in the following sequence: the results obtained using experimental boundary conditions for intake pressure; the results for pressure correction procedure; the results obtained using fitted pressure boundary conditions for intake pressure. After presenting those results, the comparison between results using experimental boundary conditions and fitted boundary conditions, for selected engine operating conditions are presented for selected cases, in order to highlight the trends observed for all cases. Last result presented is a resume of the achievements of the methodology proposed for all cases.

The following topics are unprecedented:

- Presentation of results for six different engine operating conditions, obtained by engine CFD 3D model using RANS approach for turbulence (section 4.1, subsection 4.5.1, subsection 4.5.2);
- Statement that all of the results are obtained using the same values for all of the sub-models constants.
- Proposition of a hypothesis about systematic excess of air, associated to intake pulsating flow (section 4.2);
- Proposition of pulsating flow head loss method, to adjust intake pressure boundary condition based on trapped mass of air (subsection 4.2.1);

Once the model quality is verified for different operating conditions, it can also be used at intermediate conditions between the verified ones, along with a boundary condition interpolation methodology. This boundary condition interpolation methodology is unprecedented, out of the scope of this thesis, and is suggested for future works.

4.1 RESULTS FOR ENGINE CFD 3D MODEL USING EXPERIMENTAL INTAKE PRESSURE, COMPARED TO EXPERIMENTAL RESULTS

The results presented for engine CFD 3D model using experimental intake pressure are only those related to injected mass of fuel, lambda and trapped mass of air, for which it is observed a systematic excess of trapped mass of air for all cases. Those results are evidence that engine CFD 3D using RANS approach don't capture pulsating flow effects, and motivated the pressure correction procedure.

4.1.1 Trapped mass of air and lambda

The results calculated using engine CFD 3D model for injected mass of fuel, lambda and trapped mass of air are presented and compared to experimental correlated data in Table 4.1,

Table 4.2 and Table 4.3, respectively, at engine operating conditions of 1000 rpm 3 bar, 2000 rpm 3 bar, 2000 rpm 8 bar, 2500 rpm 3 bar, 2500 rpm 5 bar and 2500 rpm 8 bar.

Table 4.1 – Results for injected mass of fuel calculated by engine CFD 3D model at several cases, using measured intake pressure as intake boundary condition, in comparison with experimental data.

	1000 rpm 3 bar	2000 rpm 3 bar	2000 rpm 8 bar	2500 rpm 3 bar	2500 rpm 5 bar	2500 rpm 8 bar
Mass of fuel injected exp [mg]	19.2	18.0	40.7	17.2	26.5	39.7
Mass of fuel injected cfd [mg]	19.1	17.9	40.7	17.2	26.5	39.5
Error [%]	-0.4	-0.2	0.01	-0.2	-0.2	-0.3

SOURCE: Elaborated by the author.

The results for mass of fuel injected per cycle at engine CFD 3D model are presented in Table 4.1, in comparison to experimental based calculated results. The error presented in the same table is the relative difference between numerical and experimental data, referenced to the experimental data. It is observed that the absolute value of the error is smaller than 0.5% for all engine operating conditions, which means that the total mass of liquid fuel injected per cycle in the engine CFD 3D model is representing the experimental corresponding value for all of the cases evaluated in Table 4.1.

The results for in cylinder lambda factor calculated by engine CFD 3D model, in comparison to experimental value measured at exhaust manifold, are presented in Table 4.2. In this table, three different values for lambda, calculated by engine CFD 3D model, are presented: lambda for total evaporation, effective lambda and corrected lambda.

Table 4.2 – Results for lambda calculated by engine CFD 3D model at several cases, using measured intake pressure as intake boundary condition, in comparison with experimental data.

	1000 rpm 3 bar	2000 rpm 3 bar	2000 rpm 8 bar	2500 rpm 3 bar	2500 rpm 5 bar	2500 rpm 8 bar
Lambda exp [dim]	0.998	1.002	0.997	1.000	0.996	1.004
Lambda cfd for total evaporation	1.388	1.342	1.281	1.425	1.378	1.318
Effective lambda	1.483	1.535	1.611	1.643	1.682	1.749
Corrected lambda	1.418	1.458	1.557	1.581	1.629	1.704
Error [%]	42.1	45.5	56.2	58.1	63.6	69.7

SOURCE: Elaborated by the author.

Lambda for total evaporation is the lambda factor calculated by the injected mass of ethanol, trapped mass of air, and stoichiometric equivalence ratio, which consider that all of the injected fuel evaporates at the case. Effective lambda is the value of engine CFD 3D output variable in cylinder average lambda at the spark timing, and is important to note that this value of lambda takes into account the excess of nitrogen inside the cylinder. The experiment value for lambda is measured at the exhaust manifold, and is assumed for the in cylinder combustion process under the consideration that the effects of exhaust gas recirculation are negligible, this way it does not consider the in cylinder excess of nitrogen due to internal exhaust gas recirculation. The corrected lambda value is calculated for in cylinder results considering the ratio between nitrogen and oxygen at intake ducts(manifold, runner, port), and performed a reduction at in cylinder mass of nitrogen at spark timing. This way, in cylinder lambda is calculated along with an estimate for internal exhaust gas recirculation.

Table 4.3 – Results for trapped mass of air calculated by engine CFD 3D model at several cases, using measured intake pressure as intake boundary condition, in comparison with experimental data.

	1000 rpm 3 bar	2000 rpm 3 bar	2000 rpm 8 bar	2500 rpm 3 bar	2500 rpm 5 bar	2500 rpm 8 bar
Mass of air trapped exp [mg]	161.9	151.6	343.4	145.2	223.6	334.1
Mass of air trapped cfd [mg]	219.2	195.8	426.5	194.9	273.9	410.5
Excess of air cfd [mg]	57.7	43.9	84.3	49.6	51.2	74.9
Excess of air cfd [%]	35.7	28.9	24.6	34.1	23.0	22.3

SOURCE: Elaborated by the author.

The result for in cylinder trapped mass of air calculated by engine CFD 3D model, in comparison to experimental based calculated value, is presented in Table 4.3. Based on the comparison between experimental and numerical results for trapped mass of air, it is calculated the excess of air for engine CFD 3D results for all of the six engine operating conditions, and its relative value compared to the experimental trapped mass of air. The relative excess of air for all of the operating conditions presented is in the range between 20% and 40%, where the minimum excess of air in obtained for 2500 rpm 8 bar, which is 22.3%.

In Table 4.1 through Table 4.3, the most relevant results for engine CFD 3D model obtained using experimental measured intake pressure as intake flow boundary conditions are presented, in comparison to experimental data, measured for lambda factor and calculated for mass of fuel injected per cycle and trapped mass of air. The comparison is made for six different engine operating conditions, which is unprecedented, and the difference between numerical and experimental results are calculated for each value, especially for trapped mass of air, based on

Equation 1.1, which is attributed to the simulation error for each of the evaluated variables based on (ASME, 2009).

This is the first part of the verification and validation procedure, which is the calculation of the simulation error. The next step is the comparison of the uncertainty $U_{95\%}$ for a 95% confidence interval, which can't be calculated for engine CFD 3D model due to some missing steps in the procedure, an the sake of available time for the computational effort spent on this thesis. The evaluation of sensibility for boundary conditions is the most important next step in the procedure described at (ASME, 2009), and a lot of computational effort should be spent on this, in such a manner it is a propose for future work. This is the reason for not presenting neither experimental nor numerical $U_{95\%}$ values.

An interesting form of presenting engine CFD 3D results obtained for in cylinder excess of air is a map, what is performed at Table 4.4 with the obtained values of relative excess of air at given engine speeds and loads. It can be observed that for a given engine speed, the excess of air decrease with increase of engine load, what is observed for 2000 rpm and 2500 rpm. Otherwise, for a given load, considering the observed engine operating speeds, it can't be observed any clear trend in excess of air.

Table 4.4 – Engine CFD 3D model excess of air, using measured intake pressure as boundary condition, presented in the form of an engine map.

Excess of air map.				
Engine load BMEP [bar]	8.0	-	24.6%	22.3%
	5.0	-	-	23.0%
	3.0	35.7%	28.9%	34.1%
		1000	2000	2500
		Engine speed [rpm]		

SOURCE: Elaborated by the author.

4.2 PROPOSED HYPOTHESIS ABOUT SYSTEMATIC EXCESS OF AIR

Comparing the results presented in Table 4.1 through Table 4.3, the values for mass of fuel injected per cycle between experiment and model are almost equal for all engine conditions in Table 4.1, but the values of trapped mass of air per cycle in Table 4.3 are considerably different between experiment and model for each condition. Consequently, the lambda factor at engine CFD 3D model for total evaporation at Table 4.2 is considerably higher than experimental measured lambda value for all operating conditions. This means that for the single cylinder engine described at section 3.2, the engine CFD 3D model using RANS approach for turbulence cannot reproduce the average combustion *phenomena* for any of the described operating conditions, due to systematic excess of air calculated by the model.

It is unprecedented to describe explicitly this systematic excess of air, and to propose the hypothesis that the observed excess of air in Table 4.1 through Table 4.3 occurs due to

limitations of engine CFD 3D models using RANS approach for turbulence, in terms of describing the effects of pulsating flow at intake ducts over trapped mass of air.

As described in section 2.3, it has been published a long time by several authors that pulsating flow occurs at intake manifold of internal combustion engines, and also that one of the most important effects of this pulsating flow for naturally aspired engines is the reduction of volumetric efficiency for the intake induction process.

It is also known that engine CFD 3D models using RANS approach cannot capture the details of the flow field, but just calculate an average flow *phenomena*, although the average flow *phenomena* occuring at intake ducts includes pulsating flows, which needs adequate physical modelling, time and space discretization in order to capture its main effects.

It has been shown in section 2.5 that the most recent publications concerning engine CFD 3D model, including LES and DNS approaches for turbulence, don't pay attention to the intake pulsating flow *phenomena* effect, and whether actual engine CFD 3D models capture this effect or not. Indeed, it has not been found any publication concerning which intake pulsating flow frequencies must be captured by engine CFD 3D models in order to reproduce in cylinder trapped mass of air or lambda, in comparison to experimental results.

In this thesis, it is proposed the hypothesis that engine CFD 3D models using RANS approach for turbulence cannot reproduce the trapped mass of air inside the cylinder of naturally aspired engines, once this turbulence approach cannot capture the detailed effects of pulsating flow over volumetric efficiency verified by experimental publications in literature. This hypothesis is based on the obtained results for excess of trapped mass of air in Table 4.1 through Table 4.3, and on the discussion above concerning engine CFD 3D modelling limitations using RANS approach for turbulence and the effect of pulsating flow over engine volumetric efficiency.

The implication of this hypothesis is that engine CFD 3D models using RANS approach cannot reproduce average combustion *phenomena*, if no correction of the model is made in order to reproduce measured values for lambda and experimental based values for trapped mass of air. This is the motivation for the pressure correction procedure.

4.2.1 Pulsating flow head loss at intake ducts(manifold, runner, port)

The differences observed in section 4.1 concerning trapped mass of air in all cases makes it impossible for the engine CFD 3D model to reproduce lambda factor experimental data for each case, using experimental data intake pressure boundary conditions. This way, it is not possible, at the given engine, for any engine CFD 3D model to reproduce combustion results, pressure trace or IMEP from experiment, without changing spray sub model and combustion sub model parameters. This way, even if it was achieved the validation at one given engine operating condition, for other engine conditions the sub models would have different values for its constants, and the model could not be used for interpolated experimental data boundary conditions, and would be far from predicting engine combustion results.

Based on the hypothesis proposed at section 4.2 and on the results presented at section 4.1, the effects of pulsating flow at intake ducts of the engine described at section 3.2 over trapped mass of air cannot be captured by the engine CFD 3D model using RANS approach for turbulence proposed in this thesis, if the pressure experimental data is used. Once LES approach is not used in this thesis, and it has not been found any paper in literature evaluating the capabilities of engine CFD 3D models using LES approach in terms of capturing the effects of pulsating flow over volumetric efficiency, nothing is stated about engine CFD 3D model using LES approach for turbulence.

In this thesis, it is proposed a method for correction of experimental data pressure values at intake manifolds described in subsection 3.8.2, in such a manner that the engine CFD 3D model proposed using RANS approach for turbulence can reproduce experimental data values for lambda and trapped mass of air. The motivation for this procedure is that engine CFD 3D models using RANS approach for turbulence and the procedure described in subsection 3.8.2, can reproduce systematically engine combustion results for trapped mass of air, lambda and IMEP, and present good agreement with experimentally measured pressure trace, which is not posible using experimental data for intake pressure boundary condition. This should be done without changes at any sub model, this way the model can be used to interpolate and extrapolate results, once interpolation and extrapolation procedures are validated, which is far beyond the scope of this thesis, and is a propose of future work.

The engine CFD 3D model using RANS equations accounts for head loss due to viscosity effects of the fluid flow, and is able to capture this *phenomena*. The procedure described is named following this idea, as a procedure for pressure correction due to pulsating flow head losses at intake ducts. This doesn't mean that there is a head loss due to pulsating flow occurring at the experiment, which should be verified, indeed, the reduction of air mass flow can be seen as a reduction in the energy of the intake flow, which occurs due to pulsating flow effects. Instead of trying to prove this idea, which is far beyond the scope of this thesis, the pulsating flow head loss is defined here as a numerical procedure for engine CFD 3D simulation, in order to systematically predict correctly the trapped mass of air and lambda for the given engine, which is a naturally aspired engine. Any other application of the proposed hypothesis is considered a future work propose, for sake of available time and resources.

4.3 RESULTS FOR PRESSURE CORRECTION

The solution proposed in this thesis for the problem highlighted in section 4.2 is the pressure correction procedure, described in subsection 3.8.2. The results for the pressure correction procedure are presented in Table 4.5.

In Table 4.5, the trapped mass of air calculated based on experimental measurements is the main reference, along with intake pressure measured. The reduced intake pressure and correspondent trapped mass of air are presented, for knowledge. The main results from pressure

Table 4.5 – Results for the pressure correction procedure, for the given engine speed and load combinations.

	1000 rpm 3 bar	2000 rpm 3 bar	2000 rpm 8 bar	2500 rpm 3 bar	2500 rpm 5 bar	2500 rpm 8 bar
Mass of air trapped exp [mg]	161.5	151.9	342.2	145.3	222.7	335.6
Intake Pressure exp[bar]	0.500	0.468	0.913	0.459	0.630	0.897
Mass of air trapped cfd [mg]	219.2	195.8	426.5	194.9	273.9	410.5
Intake Pressure reduced [bar]	0.300	0.289	0.610	0.249	0.417	0.579
Mass of air trapped cfd - reduced pressure [mg]	123.4	110.2	274.4	100.0	221.2	266.0
Intake Pressure fitted [bar]	0.380	0.377	0.753	0.345	0.501	0.714
Intake Pressure correction [bar]	-0.119	-0.091	-0.160	-0.113	-0.129	-0.165
Intake Pressure correction %	-23.9	-19.4	-17.5	-24.7	-20.4	-18.8

SOURCE: Elaborated by the author.

correction procedure are the fitted values of intake pressure, along with the intake pressure correction, in units of [bar] and relative values based in the measured values.

The values calculated for intake pressure correction, in units of [bar], are considered pressure correction for head loss due to pulsating effects as described in section 4.2, and should be applied to intake pressure boundary condition in engine CFD 3D model using RANS approach, in order to reproduce pulsating flow effects at trapped mass of air.

The values for intake pressure correction can also be presented in the form of an engine map, as it is presented in Table 4.6 for relative pressure correction.

Table 4.6 – Results for pressure correction procedure, presented in the form of an engine map.

Pressure correction map.				
Engine load BMEP [bar]	8.0	-	-17.5%	-18.8%
	5.0	-	-	-20.4%
	3.0	-23.9%	-19.4%	-24.7%
		1000	2000	2500
		Engine speed [rpm]		

SOURCE: Elaborated by the author.

The behaviour of relative pressure correction in Table 4.6 is similar to the one observed for percent excess of air in Table 4.4. For example, as higher is the load for a given speed, smaller is the pressure correction, as it it can be seen for 2000 rpm and 2500 rpm.

4.4 RESULTS FOR GLOBAL HEAT TRANSFER MODEL

Results for wall surface temperature at all of the regions considered in the global heat transfer model are presented in Table 4.7 and Table 4.8, for all of the engine conditions simulated. The results of the global heat transfer model are presented for first (1st) and second (2nd) iterations at Table 4.7, along with the difference relative to first iteration.

Table 4.7 – Results for wall surface temperature at all surfaces of the global heat transfer model, for first (1st) and second (2nd) iteration.

		1000 rpm 3 bar	2000 rpm 3 bar	2000 rpm 8 bar	2500 rpm 3 bar	2500 rpm 5 bar	2500 rpm 8 bar
Piston [K]	1st	403.0	414.9	432.7	416.0	436.4	463.0
	2nd	420.5	428.7	452.6	439.7	443.7	455.4
	Dif	4.34%	3.33%	4.60%	5.70%	1.67%	-1.64%
Cylinder liner [K]	1st	369.4	374.6	379.8	376.1	380.8	386.7
	2nd	374.2	381.9	387.8	384.7	387.9	390.8
	Dif	1.30%	1.95%	2.11%	2.29%	1.86%	1.06%
Cylinder head [K]	1st	373.8	381.6	387.5	384.3	390.9	398.6
	2nd	383.2	396.3	403.9	400.3	402.4	405.8
	Dif	2.51%	3.85%	4.23%	4.16%	2.94%	1.81%
Intake valve face [K]	1st	391.8	415.7	433.9	424.0	446.4	475.2
	2nd	389.1	409.6	411.3	412.8	412.5	414.2
	Dif	-0.69%	-1.47%	-5.21%	-2.64%	-7.59%	-12.8
Exhaust valve face [K]	1st	415.8	448.0	466.5	458.5	481.0	500.7
	2nd	468.3	528.6	549.5	540.7	545.8	554.4
	Dif	12.6%	18.0%	17.8%	17.9%	13.5%	10.7%
Intake valve stem [K]	1st	382.9	400.3	413.4	406.4	422.4	422.6
	2nd	377.1	391.1	391.3	393.0	392.4	393.0
	Dif	-1.51%	-2.30%	-5.35%	-3.30%	-7.10%	-11.2%
Intake port [K]	1st	367.9	371.2	373.2	372.2	374.4	376.2
	2nd	373.4	380.8	383.8	382.5	383.6	385.0
	Dif	1.49%	2.59%	2.84%	2.77%	2.46%	2.34%
Exhaust valve stem [K]	1st	409.5	436.5	451.0	445.2	462.1	473.8
	2nd	463.5	520.6	537.9	530.5	534.7	541.8
	Dif	13.2%	19.3%	19.3%	19.2%	15.7%	14.4%
Exhaust port [K]	1st	369.3	373.2	375.4	374.3	376.7	378.2
	2nd	377.3	386.8	390.4	388.8	390.4	392.0
	Dif	2.17%	3.64%	4.00%	3.87%	3.64%	3.65%

SOURCE: Elaborated by the author.

The results calculated by second iteration are quite close to the ones calculated by the first iteration for all surface temperature calculated except for exhaust valve face and exhaust valve stem, as it can be seen at Table 4.7 for every engine operating conditions. An example is engine condition of 1000 rpm 3 bar, for which the absolute value of the relative difference is smaller than 5.0% at every surface temperature, except for exhaust valve face and exhaust valve stem. The same trend occurs for 2000 rpm 3 bar, in case, the absolute values of the relative

differences are always smaller than 5.0%, and at this point it is important to highlight that the convergence criteria defined at subsection 3.8.3 is 5%. At engine condition of 2000 rpm 8 bar, the absolute value of the relative difference for intake valve face and intake valve stem are 5.2% and 5.3%, which do not attend to a convergence criteria of 5%, but is quite close to this criteria.

It is also interesting to note that intake valve face and stem surface temperatures decrease from first to second iterations for all engine operating conditions evaluated, along with the great increase in exhaust valve face and stem surface temperatures. The methodology for implementation of the global heat transfer model described in subsection 3.8.3, considers for the first iteration heat transfer coefficients from literature and in cylinder gas temperature combined between experimental calculated values and previous simulation values. For the second iteration, heat transfer coefficients and in cylinder temperature are used from engine CFD 3D third cycle results. This way, the differences between surface temperature values occurs due to two different changes: the mean value of in cylinder temperature and the mean value of heat transfer coefficient for each surface.

Although those two effects occurs simultaneously, only exhaust valve surface temperatures present considerable difference from first to second iteration. In this thesis, using a 5% convergence criteria, it is necessary a third iteration between global heat transfer model and engine CFD 3D model.

Considering applications where a 10% convergence criteria is accepted, the semi empirical heat transfer model would be nearly accepted, and only the exhaust valve heat transfer correlations would need to be revised, in order to attend to the 10% convergence criteria. In such application, it would not be necessary to solve decoupled iteratively engine CFD 3D and global heat transfer models. Nevertheless, the reason for the difference observed in the exhaust valve surface temperatures between first and second iteration is unknown, and could be due to all of the equations that compose the heat transfer through valves modelling approach in section 3.7. This way, the assessment of the explanation for the difference observed in the exhaust valve surface temperatures between first and second iteration is left as a future work proposal.

Once the relative differences between first and second iterations for a few surface temperatures are greater than 5%, it is necessary to run a third iteration of global heat transfer model. This third iteration requires boundary conditions from the engine CFD 3D model using second iteration wall temperatures, which demands a great computational effort. Due to lack of available time, the engine operating conditions of 1000 rpm 3 bar, 2000 rpm 3 bar and 2000 rpm 8 bar are selected for running engine CFD 3D model using second iteration wall temperatures. This way, the third iteration of global heat transfer model is not evaluated for engine operating conditions associated to 2500 rpm.

The results for wall surface temperature at all of the regions considered in the global heat transfer model for second (2nd) and third (3rd) iterations are presented in Table 4.8, for the selected engine operating conditions above mentioned. Considering the selected engine

operating conditions in Table 4.8, all of the relative differences between second and third iteration values present the absolute value smaller than 5%.

Table 4.8 – Results for wall surface temperature at all surfaces of the global heat transfer model, for second (2nd) and third (3rd) iteration.

		1000 rpm 3 bar	2000 rpm 3 bar	2000 rpm 8 bar
Piston [K]	2nd	420.5	428.7	452.6
	3rd	434.8	431.7	459.2
	Dif	3.40%	0.70%	1.46%
Cylinder liner [K]	2nd	374.2	381.9	387.8
	3rd	378.6	382.2	388.8
	Dif	1.18%	0.08%	0.26%
Cylinder head [K]	2nd	383.2	396.3	403.9
	3rd	386.4	397.1	404.1
	Dif	0.84%	0.20%	0.05%
Intake valve face [K]	2nd	389.1	409.6	411.3
	3rd	399.3	409.1	411.6
	Dif	2.62%	-0.12%	0.07%
Exhaust valve face [K]	2nd	468.3	528.6	549.5
	3rd	480.8	531.6	551.4
	Dif	2.67%	0.57%	0.35%
Intake valve stem [K]	2nd	377.1	391.1	391.3
	3rd	384.0	390.8	391.3
	Dif	1.83%	-0.08%	0.00%
Intake port [K]	2nd	373.4	380.8	383.8
	3rd	374.2	381.1	383.1
	Dif	0.21%	0.08%	-0.18%
Exhaust valve stem [K]	2nd	463.5	520.6	537.9
	3rd	471.4	523.0	539.2
	Dif	1.70%	0.46%	0.24%
Exhaust port [K]	2nd	377.3	386.8	390.4
	3rd	378.1	387.1	389.4
	Dif	0.21%	0.08%	-0.26%

SOURCE: Elaborated by the author.

Once that for the selected engine operating conditions, the maximum temperature relative differences between second and third iterations are smaller than 5%, the decoupled iterative process between global heat transfer and engine CFD 3D models is considered converged. The convergence is obtained for wall surface temperatures at third iteration of global heat transfer model, and the results at second iteration of the same model are presented as the cycle average wall surface temperatures at the surfaces evaluated. Then, the results of the global heat transfer model at second iteration are presented in Table 4.9 for all of the surfaces evaluated at each engine operating condition, including the conditions for those the third iteration of global heat transfer model is not performed. This is done by considering that, if the model converges for the selected conditions, it would converge for the other engine

operating conditions.

Table 4.9 – Surface temperature calculated by the global heat transfer model at second iteration, for all regions considered at all of the engine operating conditions evaluated.

	1000 rpm 3 bar	2000 rpm 3 bar	2000 rpm 8 bar	2500 rpm 3 bar	2500 rpm 5 bar	2500 rpm 8 bar
Piston	420.5	428.7	452.6	439.7	443.7	455.4
Cylinder liner	374.2	381.9	387.8	384.7	387.9	390.8
Cylinder head	383.2	396.3	403.9	400.3	402.4	405.8
Intake valve face	389.1	409.6	411.3	412.8	412.5	414.2
Exhaust valve face	468.3	528.6	549.5	540.7	545.8	554.4
Intake valve stem	377.1	391.1	391.3	393.0	392.4	393.0
Intake port	373.4	380.8	383.8	382.5	383.6	385.0
Exhaust valve stem	463.5	520.6	537.9	530.5	534.7	541.8
Exhaust port	377.3	386.8	390.4	388.8	390.4	392.0

SOURCE: Elaborated by the author.

The values calculated by the global heat transfer model presented in Table 4.9 for surface temperature at all of the surfaces present two clear trends. The surface temperature of each surface increases with engine speed, for a given engine load. The surface temperature of each surface increases with load, for a given engine speed. The trends in the global heat transfer model are due to the fact that the heat flux also increases for both increasing load and speed.

4.5 RESULTS FOR ENGINE CFD 3D MODEL USING FITTED INTAKE PRESSURE BOUNDARY CONDITIONS, COMPARED TO EXPERIMENTAL RESULTS

The results obtained by the engine CFD 3D model using fitted intake pressure in Table 4.5 as intake pressure boundary condition are presented for different engine operating conditions in subsection 4.5.1 and subsection 4.5.2. The results presented in subsection 4.5.1 are obtained by the engine CFD 3D model using first iteration of wall temperature boundary conditions in Table 4.7, for all of the evaluated engine operating conditions. In a similar manner, the results presented in subsection 4.5.2 are obtained by the engine CFD 3D model using second iteration of wall temperature boundary conditions in Table 4.8, specifically for the selected engine operating conditions of 1000 rpm 3 bar, 2000 rpm 3 bar and 2000 rpm 8 bar.

4.5.1 First iteration of global heat transfer model

The results obtained by the engine CFD 3D model for mass of fuel injected are presented in Table 4.10, in comparison with experimental based calculated results. The values in Table 4.10 are practically the same as the ones in Table 4.1, this way no change is made at injected mass of fuel inside the cylinder for engine CFD 3D model after pressure correction procedure.

Table 4.10 – Results for injected mass of fuel calculated by engine CFD 3D model at several cases, using fitted intake pressure as intake boundary condition and first iteration heat transfer model results as wall temperature boundary condition, in comparison with experimental data.

	1000 rpm 3 bar	2000 rpm 3 bar	2000 rpm 8 bar	2500 rpm 3 bar	2500 rpm 5 bar	2500 rpm 8 bar
Mass of fuel injected exp [mg]	19.2	18.0	40.7	17.2	26.5	39.7
Mass of fuel injected cfd [mg]	19.1	18.0	40.7	17.2	26.4	39.6
Error [%]	-0.4	-0.01	0.01	-0.2	-0.5	-0.2

SOURCE: Elaborated by the author.

The results calculated by the engine CFD 3D model for the trapped mass of air inside the cylinder are presented in Table 4.11, in comparison with experimental based calculated results. The comparison between the results for excess of air in Table 4.11, using as intake pressure boundary condition the fitted pressure calculated by the pressure correction procedure, and in Table 4.3, using experimental data for intake pressure boundary condition, shows a clear reduction for in cylinder excess of air. The use of intake pressure boundary condition treated by the pressure correction procedure at the engine CFD 3D model reduces the excess of air inside the cylinder for all of the engine operating conditions evaluated, and the maximum excess of air is 6.4% at 2500 rpm 3 bar.

Table 4.11 – Results for trapped mass of air calculated by engine CFD 3D model at several cases, using fitted intake pressure as intake boundary condition and first iteration heat transfer model results as wall temperature boundary condition, in comparison with experimental data.

	1000 rpm 3 bar	2000 rpm 3 bar	2000 rpm 8 bar	2500 rpm 3 bar	2500 rpm 5 bar	2500 rpm 8 bar
Mass of air trapped exp [mg]	161.9	151.6	343.4	145.2	223.6	334.1
Mass of air trapped cfd [mg]	162.2	154.9	356.2	154.5	236.8	350.9
Excess of air cfd [mg]	0.35	3.30	12.8	9.26	13.3	16.8
Excess of air cfd [%]	0.21	2.18	3.73	6.37	5.93	5.02

SOURCE: Elaborated by the author.

The results calculated by engine CFD 3D model for lambda, using fitted intake pressure boundary conditions, are presented in Table 4.12 in comparison to experimental correlated data. The comparison between engine CFD 3D results for in cylinder lambda using fitted intake

pressure boundary conditions in Table 4.12 and experimental data intake pressure boundary conditions in Table 4.2, shows a clear reduction in the relative difference between numerical and experimental results. This way, the engine CFD 3D model results for in cylinder lambda are much closer to experimental data by the use of fitted intake pressure boundary conditions.

The mass of fuel in Table 4.10 did not change in comparison to Table 4.1, and the trapped mass of air in Table 4.11 is considerably reduced from Table 4.3, as a consequence of the pressure correction procedure. This way, the results for lambda in Table 4.12 and their differences from Table 4.2 are also a consequence from pressure correction procedure.

Table 4.12 – Results for lambda calculated by engine CFD 3D model at several cases, using fitted intake pressure as intake boundary condition and first iteration heat transfer model results as wall temperature boundary condition, in comparison with experimental data.

	1000 rpm 3 bar	2000 rpm 3 bar	2000 rpm 8 bar	2500 rpm 3 bar	2500 rpm 5 bar	2500 rpm 8 bar
Lambda exp [dim]	0.998	1.002	0.997	1.000	0.996	1.004
Lambda cfd for total evaporation	1.006	1.022	1.037	1.066	1.065	1.052
Effective lambda	1.109	1.249	1.301	1.304	1.353	1.424
Corrected lambda	1.034	1.150	1.245	1.216	1.290	1.376
Error [%]	3.65	15.3	24.8	21.9	29.3	37.0

SOURCE: Elaborated by the author.

The results presented in Table 4.10 through Table 4.12 are unprecedented, in terms of reduction in difference between numerical and experimental results for trapped mass of air and in cylinder lambda obtained for six different engine operating conditions, and are also a direct consequence of pressure correction procedure. In fact, it is only possible to obtain similar results by two means: one is resolving pulsating flow at intake ducts until the effect of reduction into trapped mass of air is captured; the other one is modelling the reduction in trapped mass of air. The pressure correction procedure is the proposal for modelling this reduction in trapped mass of air due to pulsating flow effects, which is implemented in this thesis.

The comparison between Table 4.10 through Table 4.12 and Table 4.1 through Table 4.3 is an assessment of the increase in quality of results obtained by the engine CFD 3D model, considering the use of fitted intake pressure boundary conditions compared to the direct use of experimental data intake pressure boundary conditions. Moreover, considering the simulation error calculated by Equation 1.1 as a reference for estimation of model accuracy, the above mentioned comparison is also an assessment of the reduction in simulation error and increase in accuracy of the engine CFD 3D model results obtained for six different engine operating conditions, without changing any constant from any sub-model. The increase in

quality observed by the comparison between Table 4.10 through Table 4.12 and Table 4.1 through Table 4.3 is only observed for trapped mass of air and in cylinder lambda.

One thing that has not been accessed not only by lack of time, but also by lack of experimental results, is the impact of the pressure correction procedure in the quality of the results in terms of flow field variables. The above mentioned variables are the average velocities associated to the in cylinder flow field, and their quality can be assessed by the accuracy of those results in comparison to experimental correlated data. Indeed, engine CFD 3D model using RANS approach can only calculate information about an average behaviour of the flow field, nevertheless it can be useful for some means, this way it is suggested as a future work to consider the implication of the procedure proposed in this thesis over the flow field results.

The results for indicated mean effective pressure (IMEP) obtained by engine CFD 3D model are presented in Table 4.13, along with experimentally based calculated results and simulation error for IMEP, calculated using Equation 1.1, relative to the experimental value.

Table 4.13 – Results for indicated mean effective pressure (IMEP) calculated by engine CFD 3D model at several cases, using fitted intake pressure as intake boundary condition and first iteration heat transfer model results as wall temperature boundary condition, in comparison with experimental data.

	1000 rpm 3 bar	2000 rpm 3 bar	2000 rpm 8 bar	2500 rpm 3 bar	2500 rpm 5 bar	2500 rpm 8 bar
IMEP exp [bar]	2.99	3.05	7.95	2.99	5.09	7.91
IMEP cfd [bar]	2.70	2.78	8.39	2.79	4.75	8.07
Error [%]	-9.70	-8.87	5.57	-6.85	-6.76	-2.02

SOURCE: Elaborated by the author.

The results for peak pressure obtained by engine CFD 3D model are presented in Table 4.14, along with experimental data.

Table 4.14 – Results for peak pressure calculated by engine CFD 3D model at several cases, using fitted intake pressure as intake boundary condition and first iteration heat transfer model results as wall temperature boundary condition, in comparison with experimental data.

	1000 rpm 3 bar	2000 rpm 3 bar	2000 rpm 8 bar	2500 rpm 3 bar	2500 rpm 5 bar	2500 rpm 8 bar
Peak Pressure exp [bar]	22.9	21.2	47.4	21.3	30.2	45.6
Peak Pressure cfd [bar]	17.2	16.5	47.4	18.5	23.3	38.2
Error [%]	-25.0	-22.1	-0.10	-13.2	-22.7	-16.2

SOURCE: Elaborated by the author.

It is clear from the results in Table 4.13 and Table 4.14 that the engine CFD 3D model, using fitted intake pressure boundary conditions and first iteration of global heat transfer model

as wall temperature boundary conditions, presented results with considerable difference to their respective experimental data, for both IMEP and peak pressure. For 1000 rpm 3 bar, the relative difference between cfd and exp IMEP is almost 10%, meanwhile the relative difference in peak pressure is higher than 20%. This means that IMEP is much closer to experimental values than peak pressure, and for this to occur, the rest of the in cylinder pressure trace must agree between cfd and exp. For 2000 rpm 3 bar, the relative difference for IMEP between cfd and exp is also close to 10%, although the relative difference for peak pressure is greater than 20%. Once again, the entire pressure trace is closer between exp and cfd, in order that a great difference for peak pressure occur simultaneously to a much closer IMEP. For 2000 rpm, 8 bar, the IMEP relative difference is close to 5%, meanwhile the difference in the peak pressure is smaller than 1%. In this case, a negligible difference in peak pressure occurred at the same case that a small but considerable difference in IMEP.

The results for IMEP and peak pressure in Table 4.13 and Table 4.14 indicate that the relative difference for IMEP and peak pressure between engine CFD 3D model and engine experiments don't follow the same trend. Although different behaviours are present, it is observed for all cases that the difference in IMEP don't follow the same trend that the difference in peak pressure.

Once the IMEP should be the most important parameter for validation, there is an important correction for the cycle selection procedure described in section 3.8. The three parameters already mentioned are important for cycle selection, but absolute value of the difference between one given cycle IMEP and average IMEP for the measured number of cycles should also be considered in order to define the best cycle for simulation. This way, the selected cycle not only has the pressure trace closer to the average cycle, but also the IMEP.

4.5.2 Second iteration of global heat transfer model

The results obtained by the engine CFD 3D model for mass of fuel injected are presented in Table 4.15, in comparison with experimentally based calculated results. The results in Table 4.15 are obtained using fitted pressure as intake boundary condition and second iteration of global heat transfer calculations for wall temperature boundary conditions. The engine CFD 3D results are presented for the selected engine operating conditions of 1000 rpm 3 bar, 2000 rpm 3 bar and 2000 rpm 8 bar, due to lack of available time and high computational cost associated to engine CFD 3D model, as previously explained.

The values in Table 4.15 are practically the same as the ones in Table 4.1 and Table 4.10, this way no change is made at injected mass of fuel inside the cylinder for engine CFD 3D model after changing the wall temperature boundary conditions. Similar to the previous results for injected mass of fuel, the difference between numerical and experimental results are smaller than 0.5% for all of the engine conditions evaluated, this way the model reproduces the mass of liquid fuel injected, in comparison with experimental data.

The results obtained by the engine CFD 3D model for the trapped mass of air inside

Table 4.15 – Results for injected mass of fuel calculated by engine CFD 3D model at selected cases, using fitted intake pressure as intake boundary condition and second iteration heat transfer model results as wall temperature boundary condition, in comparison with experimental data.

	1000 rpm 3 bar	2000 rpm 3 bar	2000 rpm 8 bar
Mass of fuel injected exp [mg]	19.2	18.0	40.7
Mass of fuel injected cfd [mg]	19.1	17.9	40.8
Error [%]	-0.40	-0.21	0.12

SOURCE: Elaborated by the author.

the cylinder, using fitted pressure as intake boundary condition and second iteration of wall temperature values, are presented in Table 4.16. The engine CFD 3D results are presented for the selected engine operating conditions of 1000 rpm 3 bar, 2000 rpm 3 bar and 2000 rpm 8 bar, and also in comparison to experimental data for all of the selected engine conditions.

Table 4.16 – Results for trapped mass of air calculated by engine CFD 3D model at selected cases, using fitted intake pressure as intake boundary condition and second iteration heat transfer model results as wall temperature boundary condition, in comparison with experimental data.

	1000 rpm 3 bar	2000 rpm 3 bar	2000 rpm 8 bar
Mass of air trapped exp [mg]	161.9	151.6	343.4
Mass of air trapped cfd [mg]	163.2	155.5	354.4
Excess of air cfd [mg]	1.27	3.94	11.0
Excess of air cfd [%]	0.79	2.60	3.20

SOURCE: Elaborated by the author.

The results of the engine CFD 3D model for excess of air inside the cylinder in Table 4.16 show that the maximum excess of air is 3.2% at 2000 rpm 8 bar, which indicates that the numerical results for trapped mass of air are much closer to the experimental based calculated values after performing the proposed methodology. In comparison with Table 4.11, the results for the selected engine operating conditions in Table 4.16 are practically the same, which indicates that the results of the engine CFD 3D model for trapped mass of air almost do not change between first and second iteration of wall temperature values.

The results obtained by the engine CFD 3D model for lambda inside the cylinder, using

fitted pressure as intake boundary condition and second iteration of wall temperature values, are presented in Table 4.17. The engine CFD 3D results are presented for the selected engine operating conditions of 1000 rpm 3 bar, 2000 rpm 3 bar and 2000 rpm 8 bar, and also in comparison to experimental data for all of the selected engine conditions.

Table 4.17 – Results for lambda calculated by engine CFD 3D model at selected cases, using fitted intake pressure as intake boundary condition and second iteration heat transfer model results as wall temperature boundary condition, in comparison with experimental data.

	1000 rpm 3 bar	2000 rpm 3 bar	2000 rpm 8 bar
Lambda exp [dim]	0.998	1.002	0.997
Lambda cfd for total evaporation	1.012	1.028	1.031
Effective lambda	1.097	1.205	1.249
Corrected lambda	1.020	1.118	1.195
Error [%]	2.28	11.6	19.9

SOURCE: Elaborated by the author.

The results for lambda in Table 4.17 are similar to the ones for corresponding engine operating conditions at Table 4.12, in terms of lambda for total evaporation, although effective lambda and corrected lambda change considerably. This indicates that the wall temperature boundary conditions had a positive effect at the fuel evaporation, which is observed for the increase in wall temperature between first and second iteration. This way, difference between in cylinder lambda calculated by engine CFD 3D model and experimental data is smaller using second iteration wall temperature boundary conditions than first iteration ones, for the three selected engine operating conditions.

The results obtained by engine CFD 3D model for indicated mean effective pressure (IMEP), using fitted pressure as intake boundary condition and second iteration of wall temperature values, are presented in Table 4.18. The engine CFD 3D results are presented for the selected engine operating conditions of 1000 rpm 3 bar, 2000 rpm 3 bar and 2000 rpm 8 bar, and also in comparison to experimental data for all of the selected engine conditions.

It is observed an increase of the IMEP value for the three selected engine operating conditions, comparing the results obtained by the engine CFD 3D model for IMEP using first and second iteration of wall temperature boundary conditions, respectively at Table 4.13 and Table 4.18. For 1000 rpm 3 bar and 2000 rpm 3 bar, the absolute value of the negative error is reduced, meanwhile for 2000 rpm 8 bar the value of the error increase. The increase in wall temperature boundary conditions increase the value of IMEP, which is positive for the cases where the difference to experimental data is negative, and negative for the one which difference to experimental value is positive.

Table 4.18 – Results for indicated mean effective pressure (IMEP) calculated by engine CFD 3D model at selected cases, using fitted intake pressure as intake boundary condition and second iteration heat transfer model results as wall temperature boundary condition, in comparison with experimental data.

	1000 rpm 3 bar	2000 rpm 3 bar	2000 rpm 8 bar
IMEP exp [bar]	2.99	3.05	7.95
IMEP cfd [bar]	2.77	2.94	8.72
Error [%]	-7.46	-3.55	9.64

SOURCE: Elaborated by the author.

The results obtained by engine CFD 3D model for peak pressure (P_{MAX}), using fitted pressure as intake boundary condition and second iteration of wall temperature values, are presented in Table 4.19. The engine CFD 3D results are presented for the selected engine operating conditions of 1000 rpm 3 bar, 2000 rpm 3 bar and 2000 rpm 8 bar, and also in comparison to experimental data for all of the selected engine conditions.

Table 4.19 – Results for peak pressure (P_{MAX}) calculated by engine CFD 3D model at selected cases, using fitted intake pressure as intake boundary condition and second iteration heat transfer model results as wall temperature boundary condition, in comparison with experimental data.

	1000 rpm 3 bar	2000 rpm 3 bar	2000 rpm 8 bar
P_{MAX} exp [bar]	22.9	21.2	47.4
P_{MAX} cfd [bar]	17.8	18.2	52.7
Error [%]	-22.1	-14.1	11.0

SOURCE: Elaborated by the author.

The trends concerning P_{MAX} are similar to the ones in IMEP, which means the values of peak pressure increased by the use of second iteration of wall temperature boundary conditions, for the three engine selected operating conditions.

The comparison between the results obtained by the engine CFD 3D model using first and second iterations of wall temperatures shows that the differences to experimental results for corrected lambda are reduced, and the values of IMEP and P_{MAX} are increased, for the selected engine operating conditions of 1000 rpm 3 bar, 2000 rpm 3 bar and 2000 rpm 8 bar. The simultaneous occurrence of such results indicates that the most important effect of the second iteration of wall temperatures is related to the increase in the gas temperatures inside the cylinder, which has consequences of increasing the amount of evaporated fuel and reducing lambda, and reducing the heat losses to walls and thus increase IMEP and P_{MAX}. This may be an important change in the engine CFD 3D model, although there may be problems, similar to the one observed at 2000 rpm 8 bar, which is the increase in the difference between model and experiment IMEP from first to second iteration of wall temperature boundary conditions.

4.6 RESULTS FOR SELECTED ENGINE OPERATING CONDITIONS

The results presented so far are related to the simultaneous presentation of engine CFD 3D results for different engine operating conditions, considering separately each of the sets of boundary conditions used in this thesis. These sets are experimental intake pressure and first iteration wall temperature, fitted intake pressure and first iteration wall temperature and fitted intake pressure and second iteration wall temperature.

In this section, the engine CFD 3D results for selected engine operating conditions are presented along with experimental data, comparing the agreement to experimental data for different boundary conditions approaches, in terms of in cylinder pressure trace, pressure volume diagrams, in cylinder temperature trace and global values. The selected engine conditions are 2000 rpm 3 bar and 2000 rpm 8 bar, because the trends in the comparison of the engine CFD 3D model results using different sets of boundary conditions to experimental data in the selected conditions is repeated by the other engine operating conditions.

4.6.1 2000 rpm, 3 bar

The results obtained by the engine CFD 3D model for in cylinder pressure trace at 2000 rpm 3 bar are presented in Figure 4.1, compared to the correlated experimental data for the same engine condition.

Figure 4.1 – Results for in cylinder pressure trace obtained by engine CFD 3D model using different sets of boundary conditions, in comparison to experimental correlated data. Engine operating condition is 2000 rpm 3 bar, domain between -360 CAD and 360 CAD, range from 0 bar to 30 bar.

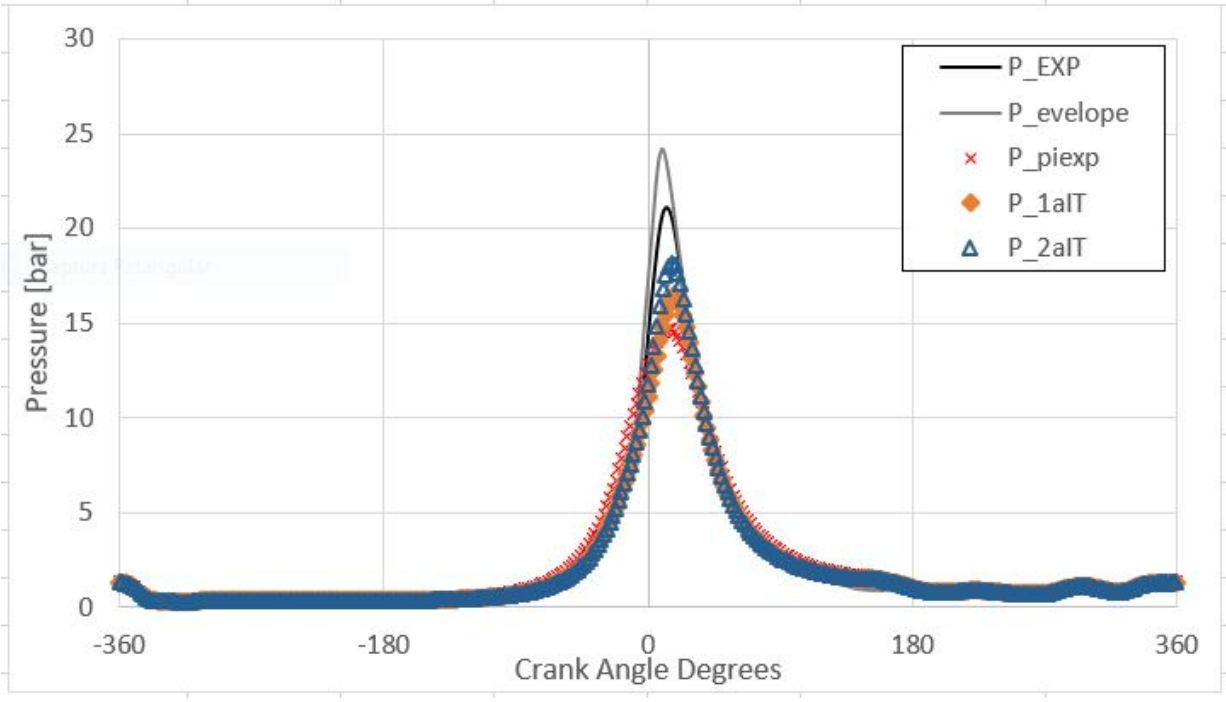

SOURCE: Elaborated by the author.

The engine CFD 3D results are presented using experimental intake pressure boundary conditions (P_piexp), which are correlated to section 4.1, fitted intake pressure boundary condition using first iteration wall temperatures (P_1aIT), correlated to subsection 4.5.1, and fitted intake pressure boundary condition using second iteration wall temperatures (P_2aIT), correlated to subsection 4.5.2. The experimental data in Figure 4.1 are the measured in cylinder pressure trace (P_EXP) for the cycle selected by the cycle selection procedure described in subsection 3.8.1, along with two representative traces for pressure envelope (P_envelope). The qualitative comparison between numerical and experimental results for in cylinder pressure in Figure 4.1, shows visual agreement during almost the whole cycle, except for the peak pressure region, where small discrepancies are observed.

Diagrams similar to Figure 4.1 are several times used in literature for qualitative validation analysis which don't follow or don't propose a validation procedure. The results for pressure trace may or may not show good agreement, but the diagram in Figure 4.1 hides several discrepancies between numerical and experimental results, due to the scales used for both pressure and crank angle degrees. In order to better observe those trends, three diagram analysis is presented in this thesis, first one for the intake and start of compression strokes, second one for end of expansion and exhaust strokes, and the third one for the combustion analysis interval, which in this thesis is comprised between -30 CAD and 90 CAD.

The first chart to compare in cylinder pressure results for 2000 rpm 3 bar is presented in Figure 4.2, where the same results in Figure 4.1 are presented for the domain between -360 CAD and 0 CAD, and for the range between 0.2 bar and 1.2 bar, for which absolute pressures are presented and the atmospheric pressure is close to 0.9 bar.

In Figure 4.2, the engine CFD 3D results for in cylinder pressure trace are presented using experimental intake pressure boundary conditions (P_piexp), which are correlated to section 4.1, fitted intake pressure boundary condition using first iteration wall temperatures (P_1aIT), correlated to subsection 4.5.1, and fitted intake pressure boundary condition using second iteration wall temperatures (P_2aIT), correlated to subsection 4.5.2. Experimental data is presented for in cylinder pressure (P_EXP) for the cycle selected by the cycle selection procedure described in subsection 3.8.1, along with two representative traces for pressure envelope (P_envelope).

The comparison between engine CFD 3D results using P_piexp as boundary conditions and P_EXP shows visual agreement between -360 CAD and -180 CAD, where numerical results present the same trends that experimental data and are also inside pressure envelope curves. Few crank angle degrees before -90 CAD, numerical results for P_piexp start to increase their difference to P_EXP, and become out of the pressure envelope.

On the other hand, all of the results using fitted pressure as intake boundary conditions, P_1aIT and P_2aIT, do not present visual agreement with P_EXP, and also are considerably out of the pressure envelope, from few crank angle degrees after -360 CAD until few crank angle degrees after -90 CAD, where all of the in cylinder pressure traces become out of the range

Figure 4.2 – Results for in cylinder pressure trace obtained by engine CFD 3D model using different sets of boundary conditions, in comparison to experimental correlated data. Engine operating condition is 2000 rpm 3 bar, domain between -360 CAD and 0 CAD, range from 0.2 bar to 1.2 bar.

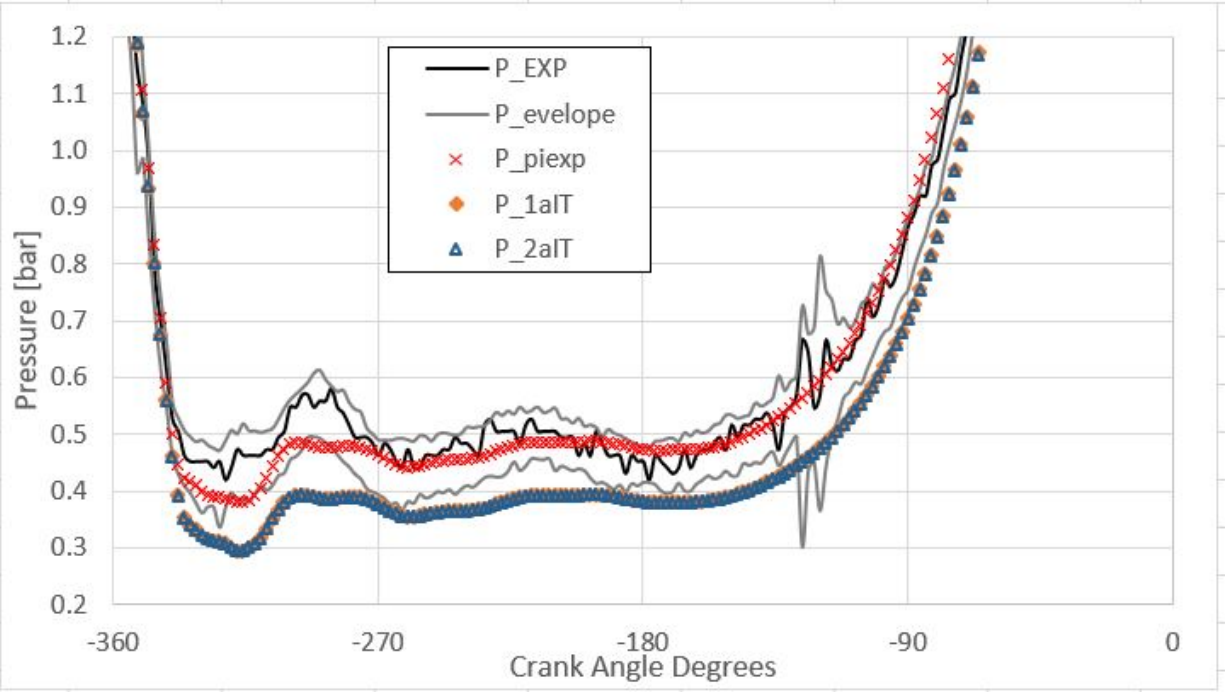

SOURCE: Elaborated by the author.

defined for the chart. From the interval comprised between -90 CAD and 0 CAD, the results for all of the variables evaluated in Figure 4.2 become out of range, once maximum pressure in this diagram is 1.2 bar, and the peak pressure for this engine operating condition is close to 20 bar.

The results presented in Figure 4.2 show that during intake stoke, engine CFD 3D model using experimental boundary conditions present visually better agreement to experimental data for in cylinder pressure trace than using fitted pressure boundary conditions. This is due to the pressure correction procedure, which makes the in cylinder pressure calculated values systematically smaller than experimental measured values for fitted pressure boundary conditions.

The second chart to compare in cylinder pressure results for 2000 rpm 3 bar is presented in Figure 4.3, where the same results in Figure 4.1 are presented for the domain between 0 CAD and 360 CAD, and for the range between 0.5 bar and 2.5 bar, for which absolute pressures are presented and the atmospheric pressure is close to 0.9 bar.

In Figure 4.3, engine CFD 3D results are presented using experimental intake pressure boundary conditions (P_piexp), which are correlated to section 4.1, fitted intake pressure boundary condition using first iteration wall temperatures (P_1aIT), correlated to subsection 4.5.1, and fitted intake pressure boundary condition using second iteration wall temperatures (P_2aIT), correlated to subsection 4.5.2. Experimental results are presented for

Figure 4.3 – Results for in cylinder pressure trace obtained by engine CFD 3D model using different sets of boundary conditions, in comparison to experimental correlated data. Engine operating condition is 2000 rpm 3 bar, domain between 0 CAD and 360 CAD, range from 0.5 bar to 2.5 bar.

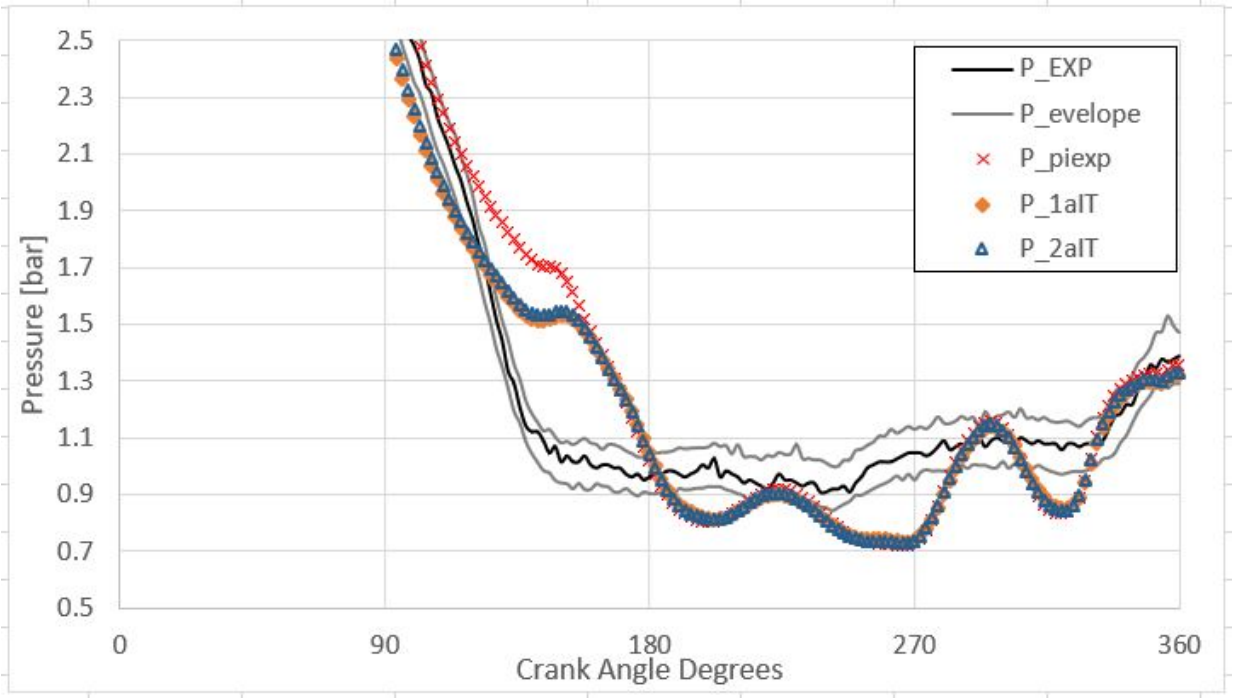

SOURCE: Elaborated by the author.

measured in cylinder pressure (P_EXP) for the cycle selected by the cycle selection procedure described in subsection 3.8.1, along with two representative traces for pressure envelope (P_envelope).

In Figure 4.3, few CAD before 180 CAD until the end of the cycle, all of the engine CFD 3D results ((P_piexp), (P_1aIT) and (P_2aIT)) are in very similar trends to each other, and in completely different trend in comparison to (P_EXP). The numerical results alternate between instants inside and outside pressure envelope, for all of the boundary conditions sets, which means no visual agreement is achieved from 0 CAD to 360 CAD, for 2000 rpm 3 bar.

The last chart to compare in cylinder pressure results for 2000 rpm 3 bar is presented in Figure 4.4, where the same results in Figure 4.1 are presented for the domain between -30 CAD and 90 CAD, and for the range between 0 bar and 30 bar, for which absolute pressures are presented.

In Figure 4.4, engine CFD 3D results are presented using experimental intake pressure boundary conditions (P_piexp), which are correlated to section 4.1, fitted intake pressure boundary condition using first iteration wall temperatures (P_1aIT), correlated to subsection 4.5.1, and fitted intake pressure boundary condition using second iteration wall temperatures (P_2aIT), correlated to subsection 4.5.2. Experimental results are presented for measured in cylinder pressure (P_EXP) for the cycle selected by the cycle selection procedure described in subsection 3.8.1, along with two representative traces for pressure envelope

Figure 4.4 – Results for in cylinder pressure trace obtained by engine CFD 3D model using different sets of boundary conditions, in comparison to experimental correlated data. Engine operating condition is 2000 rpm 3 bar, domain between -30 CAD and 90 CAD, range from 0 bar to 30 bar.

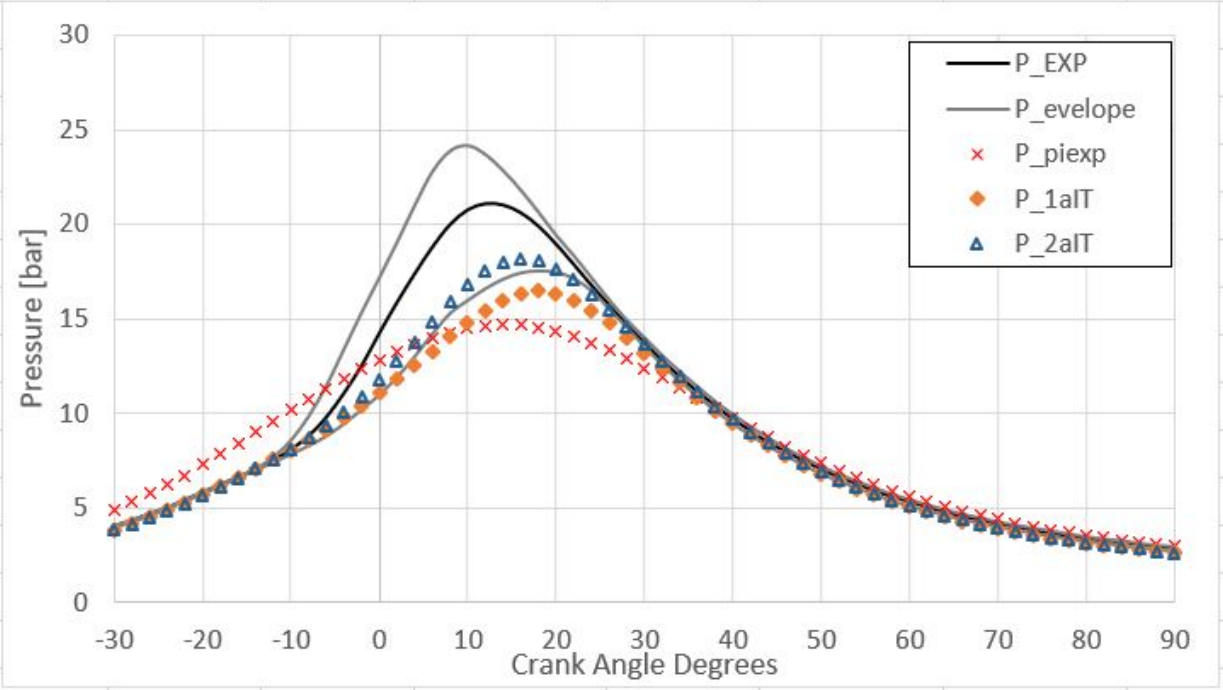

SOURCE: Elaborated by the author.

(P_envelope).

In Figure 4.4, engine CFD 3D results P_1aIT and P_2aIT present similar trends to P_EXP, including P_2aIT is inside the pressure envelope during peak pressure, meanwhile P_piexp is completely out of trends in comparison to P_EXP. The results for P_2aIT indicates that it presents the trends which could be similar to one of the 200 cycle experimental data for engine operating condition of 2000 rpm 3 bar.

Although there are visually considerable differences between P_2aIT and P_EXP in Figure 4.4, the numerical results are inside pressure envelope from -30 CAD to 90 CAD, this way it is considered in good agreement with experimental results. The trends for P_1aIT are very similar, although close to peak pressure between 10 CAD and 20 CAD these numerical results become out of the pressure envelope, and for this interval these results are not considered in good agreement. The results for P_piexp are completely out of trends in comparison with P_EXP, until few degrees after 30 CAD.

The results for in cylinder pressure can also be observed in a pressure volume diagram, similar to the one in Figure 4.5, for which numerical and experimental results are compared.

In Figure 4.5, engine CFD 3D results are presented using experimental intake pressure boundary conditions (P_piexp), which are correlated to section 4.1, fitted intake pressure boundary condition using first iteration wall temperatures (P_1aIT), correlated to subsection 4.5.1, and fitted intake pressure boundary condition using second iteration wall

Figure 4.5 – Pressure volume diagram for in cylinder pressure trace obtained by engine CFD 3D model using different sets of boundary conditions, in comparison to experimental correlated data. Engine operating condition is 2000 rpm 3 bar.

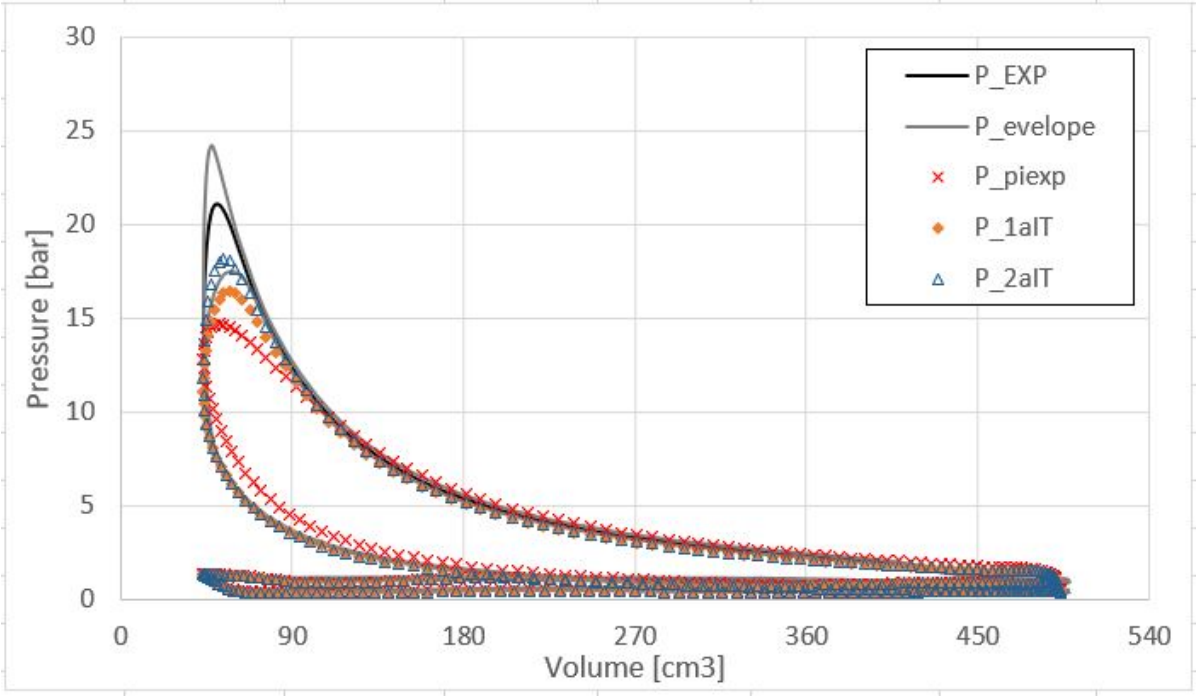

SOURCE: Elaborated by the author.

temperatures (P_2aIT), correlated to subsection 4.5.2. Experimental results (P_EXP) are presented for measured in cylinder pressure for the cycle selected by the cycle selection procedure described in subsection 3.8.1, along with two representative traces for pressure envelope (P_envelope).

The comparison between P_EXP and P_piexp is highlighted at the end of compression stroke, for which there is a clear discrepancy concerning numerical result. During the peak pressure, numerical results for P_2aIT is inside pressure envelope, which is a trend already highlighted in Figure 4.4, and the other numerical results show is out of the pressure envelope.

The comparison between trends of numerical and experimental results are better observed in a logarithm diagram, similar to the one in Figure 4.6.

In Figure 4.6, engine CFD 3D results are presented using experimental intake pressure boundary conditions (P_piexp), which are correlated to section 4.1, fitted intake pressure boundary condition using first iteration wall temperatures (P_1aIT), correlated to subsection 4.5.1, and fitted intake pressure boundary condition using second iteration wall temperatures (P_2aIT), correlated to subsection 4.5.2. Experimental results (P_EXP) are presented for measured in cylinder pressure for the cycle selected by the cycle selection procedure described in subsection 3.8.1, along with two representative traces for pressure envelope (P_envelope).

In Figure 4.6, during the intake stroke, the results for P_piexp are in better agreement with P_EXP than P_1aIT and P_2aIT, and are within pressure envelope, which is a trend

Figure 4.6 – Pressure logarithm versus volume logarithm diagram for in cylinder pressure trace obtained by engine CFD 3D model using different sets of boundary conditions, in comparison to experimental correlated data. Engine operating condition is 2000 rpm 3 bar.

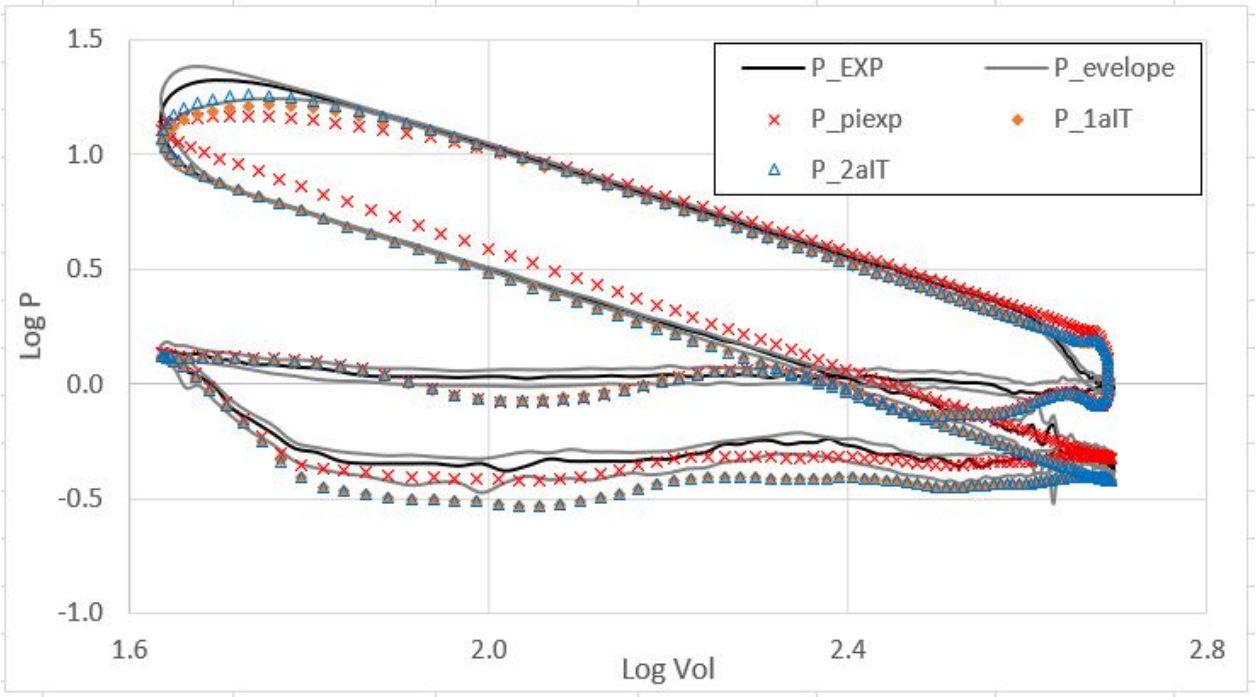

SOURCE: Elaborated by the author.

observed in Figure 4.2. During the compression stroke, the trends are changed, and P_1aIT and P_2aIT present a better agreement to P_EXP, in such a manner that both become inside pressure envelope, meanwhile P_piexp becomes considerably different then P_EXP. During peak pressure, only P_2aIT is inside pressure envelope, and during expansion stroke all of the numerical results present similar trends to P_EXP. During expansion stroke, as shown in Figure 4.3, all of the numerical results show different trends then P_EXP.

The last chart for 2000 rpm 3 bar is related to the in cylinder temperature evolution during -30 CAD and 90 CAD, in Figure 4.7.

In Figure 4.7, engine CFD 3D results are presented using experimental intake pressure boundary conditions (T_piexp), which are correlated to section 4.1, fitted intake pressure boundary condition using first iteration wall temperatures (T_1aIT), correlated to subsection 4.5.1, and fitted intake pressure boundary condition using second iteration wall temperatures (T_2aIT), correlated to subsection 4.5.2. Experimental results (T_EXP) are presented for calculated in cylinder temperature for the cycle selected by the cycle selection procedure described in subsection 3.8.1.

In Figure 4.7, between -30 CAD andn -10 CAD, all of the engine CFD 3D results are in good agreement to each other are considerably higher than T_EXP. A few degrees after -10 CAD, T_1aIT and T_2aIT present similar trends to T_EXP, meanwhile T_piexp present completely different trends until 90 CAD. It is also noticeable that the rise in temperature for

Figure 4.7 – Results for in cylinder temperature trace obtained by engine CFD 3D model using different sets of boundary conditions, in comparison to experimental correlated data. Engine operating condition is 2000 rpm 3 bar, domain between -30 CAD and 90 CAD, range from 300 K to 2100 K.

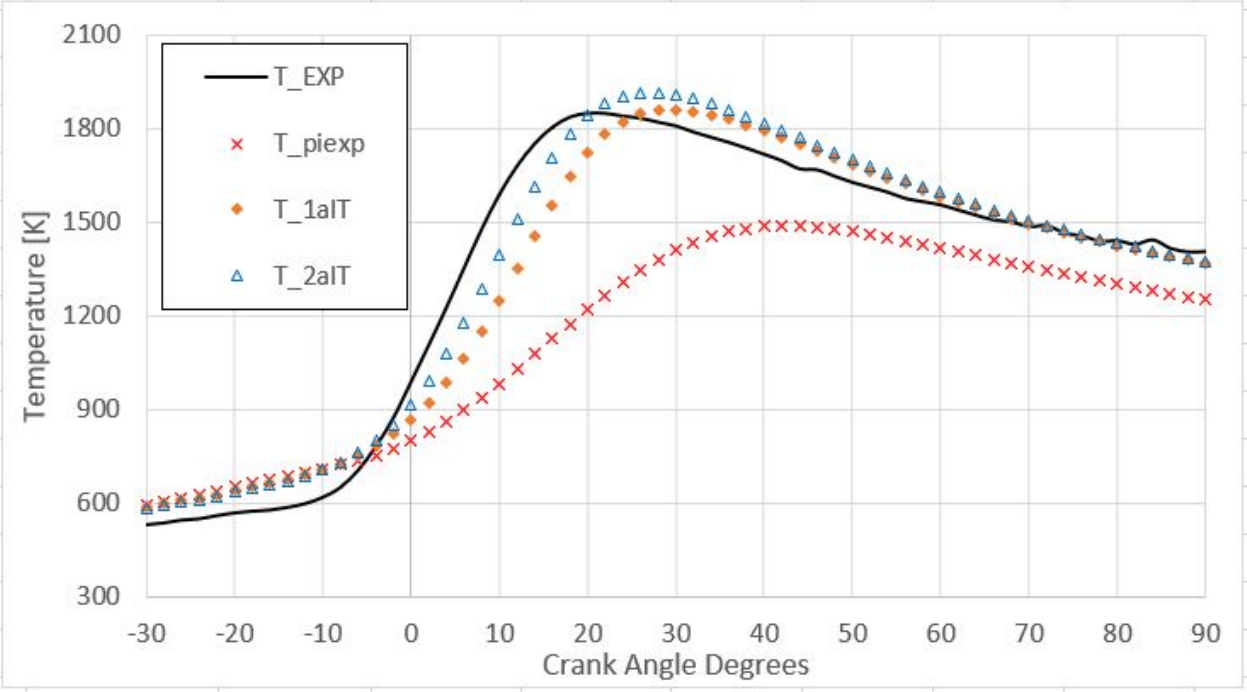

SOURCE: Elaborated by the author.

T_EXP starts and finishes earlier than T_1aIT and T_2aIT, which indicates differences in the combustion evolution process. Nevertheless, the peak temperature calculated is similar to T_EXP, T_1aIT and T_2aIT, with considerable difference in peak temperature angle.

The trends observed in Figure 4.1 through Figure 4.7 for engine operating conditions of 2000 rpm 3 bar, show that for this engine operating condition the proposed methodology for intake pressure treatment increase the accuracy of the engine CFD 3D model. This is clear for all of the results, once the trends for both in cylinder pressure and temperature are better captured using fitted intake pressure boundary conditions than experimental intake pressure boundary conditions. Moreover, the second iteration of wall temperatures perform also a considerable contribution in comparison to first iteration, once only P_2aIT is inside pressure envelope during peak pressure, and this way is considered in good agreement with experimental in cylinder pressure. Wall temperature boundary conditions plays a key role in this results in terms of changing peak pressure and temperature, once no change is performed in any sub model constant.

The increase in accuracy for 2000 rpm 3 bar can also be highlighted by the comparison of results for injected mass of fuel, trapped mass of air, lambda, IMEP and peak pressure, performed in Table 4.20.

In Table 4.20, the increase in accuracy provided by the proposed methodology, both in terms of intake pressure and wall temperature boundary conditions, is observed in all of

Table 4.20 – Results calculated by engine CFD 3D model using different sets of boundary conditions, in comparison to experimental correlated data, for 2000 rpm 3 bar.

	Experiment	Engine CFD 3D		
Intake pressure boundary condition	-	Experiment	Fitted	Fitted
Iteration of the global HT model	-	-	1st	2nd
Injected mass of fuel [mg]	18.0	18.0	18.0	17.9
Trapped mass of air [mg]	151.6	195.8	154.9	155.5
Lambda [dim]	0.998	1.458	1.150	1.118
IMEP [bar]	3.05	2.66	2.78	2.94
P max [bar]	21.2	14.7	16.5	18.2

SOURCE: Elaborated by the author.

the evaluated variables. The increase in accuracy is observed in terms of the reduction of the difference between numerical and experimental results for a given numerical result, calculated by Equation 1.1.

Based in Figure 4.1 through Figure 4.7 and in Table 4.20, it is shown that the proposed methodology increases the accuracy of the engine CFD 3D model concerning the selected engine operating at 2000 rpm 3 bar, both qualitatively in terms of in cylinder pressure and temperature traces, and quantitatively in terms of trapped mass of air, lambda, IMEP and peak pressure.

4.6.2 2000 rpm, 8 bar

The results obtained by the engine CFD 3D model for in cylinder pressure trace at 2000 rpm 8 bar are presented in Figure 4.8, compared to the correlated experimental results for the same engine condition. The engine CFD 3D results are presented using experimental intake pressure boundary conditions (P_piexp), which are correlated to section 4.1, fitted intake pressure boundary condition using first iteration wall temperatures (P_1aIT), correlated to subsection 4.5.1, and fitted intake pressure boundary condition using second iteration wall temperatures (P_2aIT), correlated to subsection 4.5.2.

The experimental results in Figure 4.8 are the measured in cylinder pressure trace (P_EXP) for the cycle selected by the cycle selection procedure described in subsection 3.8.1, along with two representative traces for pressure envelope (P_envelope). The qualitatively comparison from P_1aIT and P_2aIT to P_EXP shows good agreement including in the peak pressure, meanwhile for P_piexp the comparison to P_EXP show slight discrepancies during the peak pressure.

Diagrams similar to Figure 4.8 are several times used in literature for qualitative validation analysis which don't follow or don't propose a validation procedure. The results for

Figure 4.8 – Results for in cylinder pressure trace obtained by engine CFD 3D model using different sets of boundary conditions, in comparison to experimental correlated data. Engine operating condition is 2000 rpm 8 bar, domain between -360 CAD and 360 CAD, range from 0 bar to 60 bar.

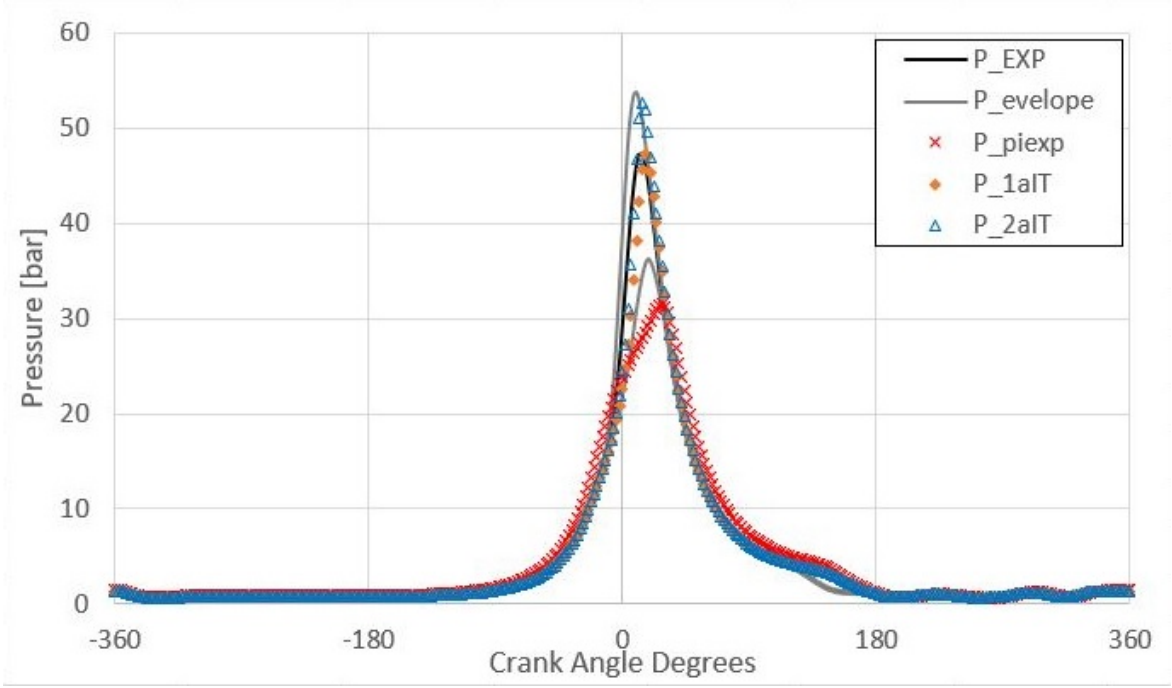

SOURCE: Elaborated by the author.

pressure trace may or may not show good agreement, but the diagram in Figure 4.8 hides several discrepancies between numerical and experimental results, due to the scales used for both pressure and crank angle degrees. In order to better observe those trends, three diagram analysis is presented in this thesis, first one for the intake and start of compression strokes, second one for end of expansion and exhaust strokes, and the third one for the combustion analysis interval, which in this thesis is comprised between -30 CAD and 90 CAD.

Similar to the results for 1000 rpm 3 bar and 2000 rpm 3 bar, the first chart to compare in cylinder pressure results for 2000 rpm 8 bar is presented in Figure 4.9, where the same results in Figure 4.8 are presented for the domain between -360 CAD and 0 CAD, and for the range between 0.6 bar and 1.6 bar, for which absolute pressures are presented and the atmospheric pressure is close to 0.9 bar.

In Figure 4.9, the engine CFD 3D results for in cylinder pressure trace are presented using experimental intake pressure boundary conditions (P_piexp), which are correlated to section 4.1, fitted intake pressure boundary condition using first iteration wall temperatures (P_1aIT), correlated to subsection 4.5.1, and fitted intake pressure boundary condition using second iteration wall temperatures (P_2aIT), correlated to subsection 4.5.2. Experimental results are presented for measured in cylinder pressure (P_EXP) for the cycle selected by the cycle selection procedure described in subsection 3.8.1, along with two representative traces for pressure envelope (P_envelope).

Figure 4.9 – Results for in cylinder pressure trace obtained by engine CFD 3D model using different sets of boundary conditions, in comparison to experimental correlated data. Engine operating condition is 2000 rpm 8 bar, domain between -360 CAD and 0 CAD, range from 0.6 bar to 1.6 bar.

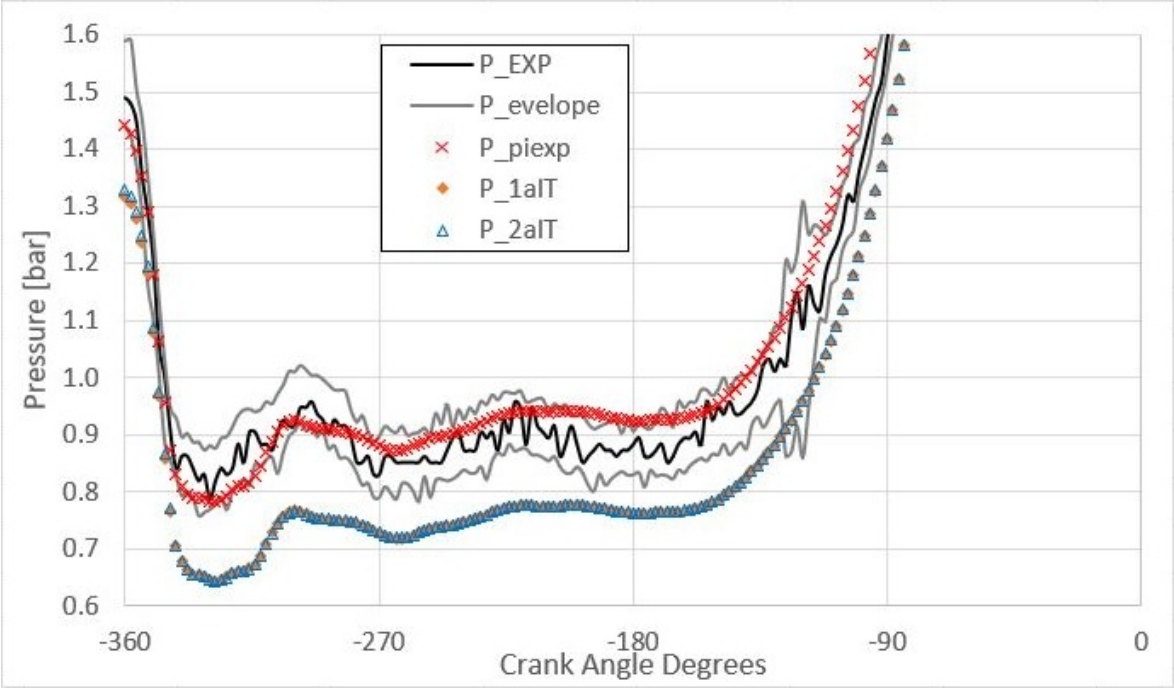

SOURCE: Elaborated by the author.

The comparison between P_piexp and P_EXP shows good agreement between -360 CAD and -180 CAD, where numerical results are close to the experimental results and are also inside pressure envelope curves, except for some instants close to -180 CAD. A few crank angle degrees before -90 CAD, results for _piexp start to increase their difference to P_EXP, and become out of the pressure envelope.

On the other hand, all of the results using fitted pressure as intake boundary conditions, P_1aIT and P_2aIT, are not in good agreement with P_EXP, and also are considerably out of the pressure envelope, from few crank angle degrees after -360 CAD until few crank angle degrees after -90 CAD, where all of the in cylinder pressure become out of the range defined for the chart.

The results presented in Figure 4.9 show that during intake stoke, engine CFD 3D model using experimental boundary conditions present better agreement to experimental results for in cylinder pressure trace than using fitted pressure boundary conditions. This is due to the pressure correction procedure, which makes the in cylinder pressure calculated values systematically smaller than experimental measured values for fitted pressure boundary conditions.

The second chart to compare in cylinder pressure results for 2000 rpm 8 bar is presented in Figure 4.10, where the same results in Figure 4.8 are presented for the domain between 0 CAD and 360 CAD, and for the range between 0.5 bar and 5.5 bar, for which absolute pressures

are presented and the atmospheric pressure is close to 0.9 bar.

Figure 4.10 – Results for in cylinder pressure trace obtained by engine CFD 3D model using different sets of boundary conditions, in comparison to experimental correlated data. Engine operating condition is 2000 rpm 8 bar, domain between 0 CAD and 360 CAD, range from 0.5 bar to 5.5 bar.

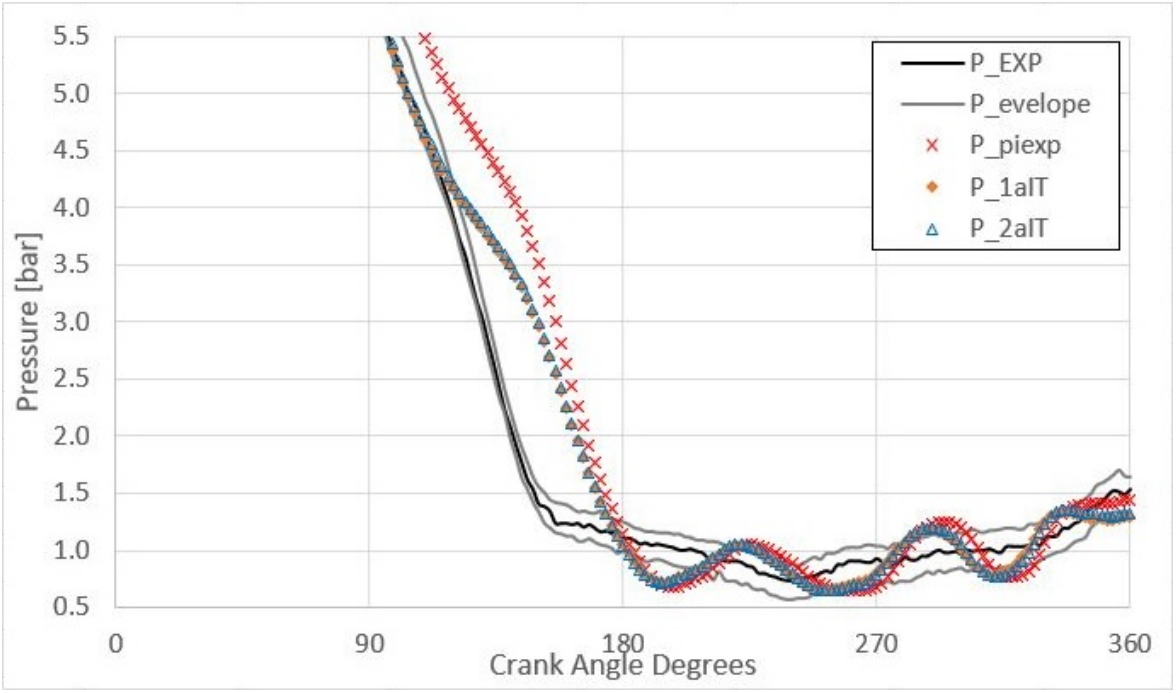

SOURCE: Elaborated by the author.

In Figure 4.10, engine CFD 3D results are presented using experimental intake pressure boundary conditions (P_piexp), which are correlated to section 4.1, fitted intake pressure boundary condition using first iteration wall temperatures (P_1aIT), correlated to subsection 4.5.1, and fitted intake pressure boundary condition using second iteration wall temperatures (P_2aIT), correlated to subsection 4.5.2. Experimental results are presented for measured in cylinder pressure (P_EXP) for the cycle selected by the cycle selection procedure described in subsection 3.8.1, along with two representative traces for pressure envelope (P_envelope).

In Figure 4.10, few CAD before 180 CAD until the end of the cycle, all of the engine CFD 3D results ((P_piexp), (P_1aIT) and (P_2aIT)) are in very similar trends to each other, and also in similar trend in comparison to (P_EXP). The numerical results present considerable oscillation, although the trends of (P_EXP) are nearly captured by all of the numerical results. Although, two important discrepancies are observed between numerical and experimental results, first one between 90 CAD and 180 CAD, second one few CAD before 360 CAD. The first difference observed is that numerical results are quite higher than experimental ones for some instant close to exhaust valve open, and the second difference observed is that numerical results are smaller than experimental ones close to exhaust valve closing, this way both differences indicate a small difference in exhaust valve timing between engine CFD 3D model

and experiment.

The last chart to compare in cylinder pressure results for 2000 rpm 8 bar is presented in Figure 4.11, where the same results in Figure 4.8 are presented for the domain between -30 CAD and 90 CAD, and for the range between 0 bar and 60 bar, for which absolute pressures are presented.

Figure 4.11 – Results for in cylinder pressure trace obtained by engine CFD 3D model using different sets of boundary conditions, in comparison to experimental correlated data. Engine operating condition is 2000 rpm 8 bar, domain between -30 CAD and 90 CAD, range from 0 bar to 60 bar.

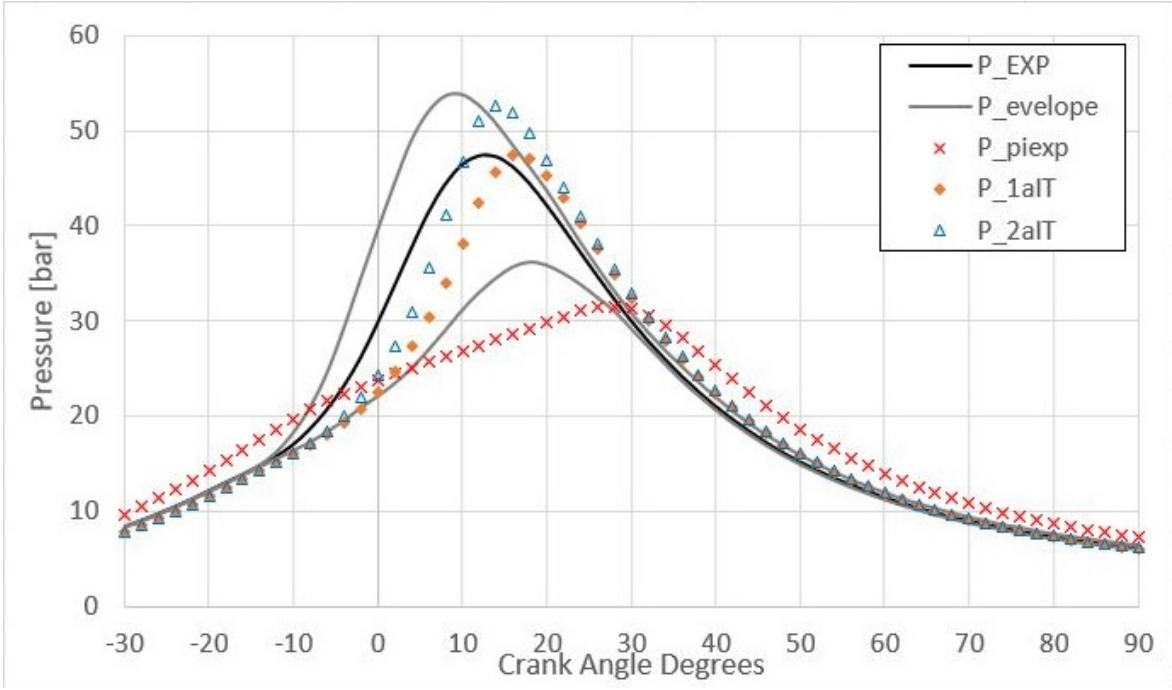

SOURCE: Elaborated by the author.

In Figure 4.11, engine CFD 3D results are presented using experimental intake pressure boundary conditions (P_piexp), which are correlated to section 4.1, fitted intake pressure boundary condition using first iteration wall temperatures (P_1aIT), correlated to subsection 4.5.1, and fitted intake pressure boundary condition using second iteration wall temperatures (P_2aIT), correlated to subsection 4.5.2. Experimental results are presented for measured in cylinder pressure (P_EXP) for the cycle selected by the cycle selection procedure described in subsection 3.8.1, along with two representative traces for pressure envelope (P_envelope).

In Figure 4.11, engine CFD 3D results P_1aIT and P_2aIT present similar trends to P_EXP, in such a manner both mentioned numerical results are inside the pressure envelope until 10 CAD, and even after becoming out of the pressure envelope, both keep following the trends presented by P_EXP. Meanwhile P_piexp is completely out of trends in comparison to P_EXP, from -30 CAD until 90 CAD.

The numerical results obtained for in cylinder pressure for P_1aIT and P_2aIT follow

the trends presented by P_EXP, although the pressure rise, the peak pressure and the pressure fall are considerably out of phase for 2000 rpm 8 bar. The peak pressure values are for P_1aIT and P_2aIT attend to the pressure envelope, nevertheless the phase shift makes it not possible to state that both of them are in good agreement to P_EXP. The numerical results for P_piexp shows higher pressure than P_EXP from -30 CAD until -10 CAD, completely different pressure rise, peak pressure and pressure fall, in such a manner after 30 CAD until 90 CAD P_piexp keep presenting higher pressure than P_EXP.

The results for in cylinder pressure can also be observed in a pressure volume diagram, similar to the one in Figure 4.12, for which numerical and experimental results are compared.

Figure 4.12 – Pressure volume diagram for in cylinder pressure trace obtained by engine CFD 3D model using different sets of boundary conditions, in comparison to experimental correlated data. Engine operating condition is 2000 rpm 8 bar.

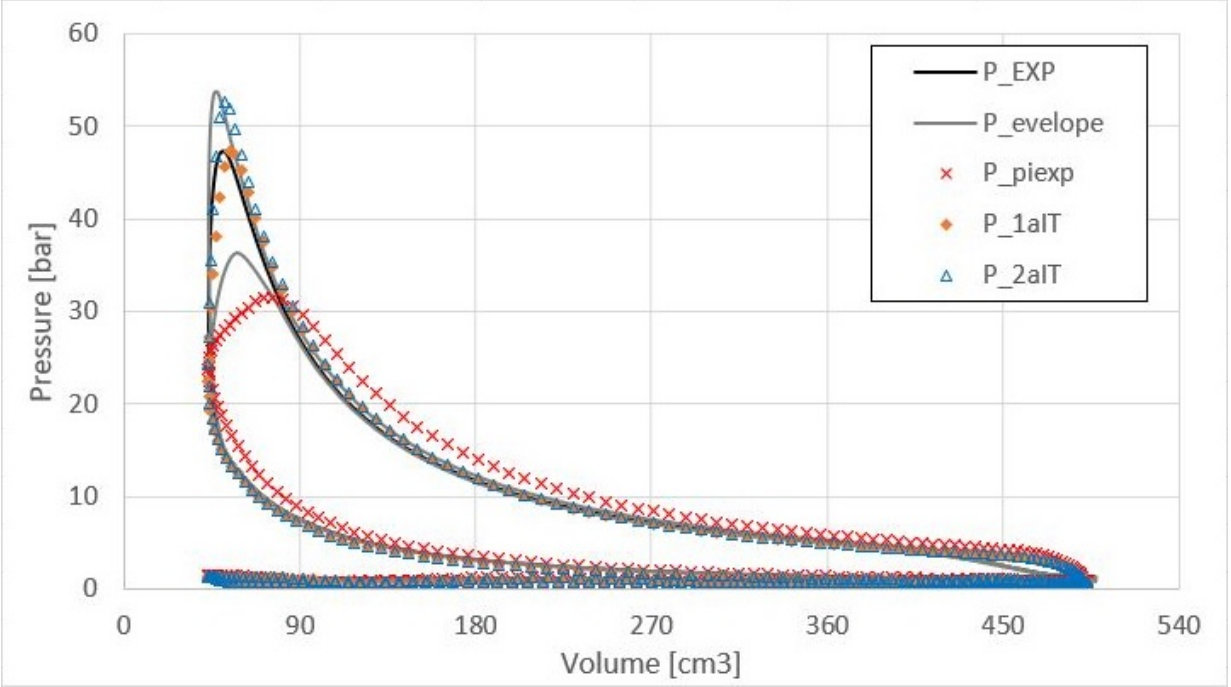

SOURCE: Elaborated by the author.

In Figure 4.12, engine CFD 3D results are presented using experimental intake pressure boundary conditions (P_piexp), which are correlated to section 4.1, fitted intake pressure boundary condition using first iteration wall temperatures (P_1aIT), correlated to subsection 4.5.1, and fitted intake pressure boundary condition using second iteration wall temperatures (P_2aIT), correlated to subsection 4.5.2. Experimental results (P_EXP) are presented for measured in cylinder pressure for the cycle selected by the cycle selection procedure described in subsection 3.8.1, along with two representative traces for pressure envelope (P_envelope).

The comparison between P_EXP and P_piexp is highlighted at the end of compression stroke, at the peak pressure and during the whole expansion stroke, in such a manner for all of those intervals there are clear discrepancies concerning numerical result. During the peak

pressure, numerical results for P_1aIT and P_2aIT are inside pressure envelope until the end of peak pressure, when both numerical results become out of pressure envelope, which is a trend already highlighted in Figure 4.11.

The comparison between trends of numerical and experimental results are better observed in a logarithm diagram, similar to the one in Figure 4.13.

Figure 4.13 – Pressure logarithm versus volume logarithm diagram for in cylinder pressure trace obtained by engine CFD 3D model using different sets of boundary conditions, in comparison to experimental correlated data. Engine operating condition is 2000 rpm 8 bar.

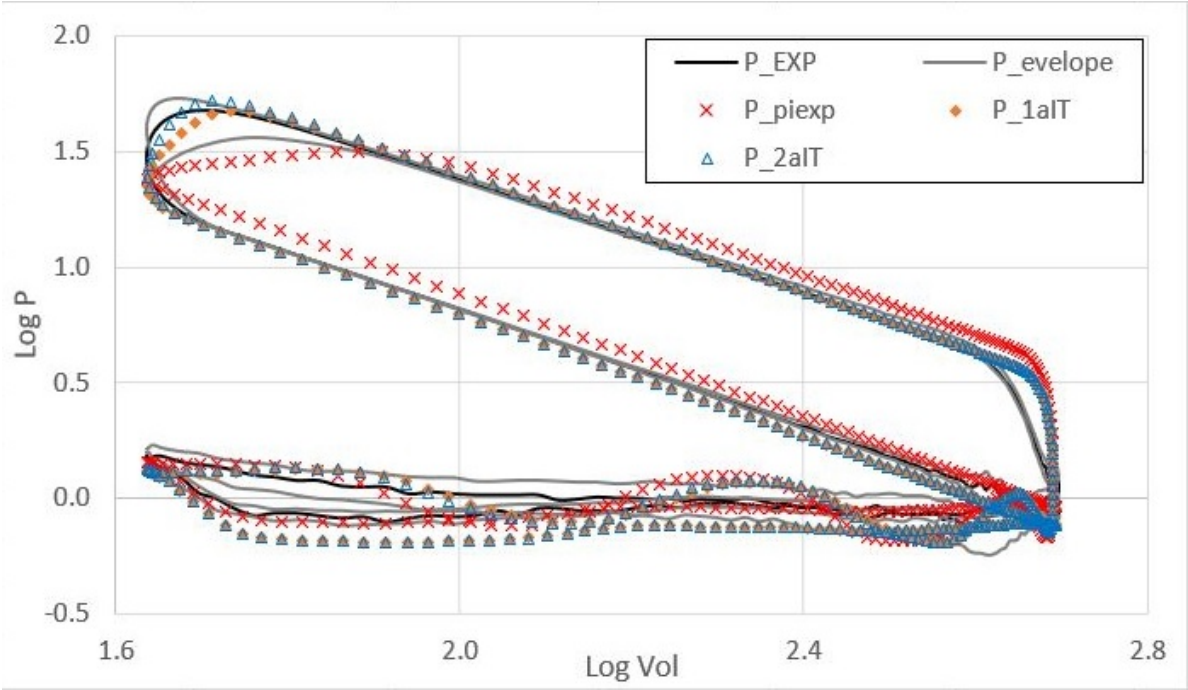

SOURCE: Elaborated by the author.

In Figure 4.13, engine CFD 3D results are presented using experimental intake pressure boundary conditions (P_piexp), which are correlated to section 4.1, fitted intake pressure boundary condition using first iteration wall temperatures (P_1aIT), correlated to subsection 4.5.1, and fitted intake pressure boundary condition using second iteration wall temperatures (P_2aIT), correlated to subsection 4.5.2. Experimental results (P_EXP) are presented for measured in cylinder pressure for the cycle selected by the cycle selection procedure described in subsection 3.8.1, along with two representative traces for pressure envelope (P_envelope).

In Figure 4.13, it is difficult to identify any trends during intake and exhaust strokes, once both of them are superimposed. During compression stroke, it is possible to identify P_piexp increasing its difference to P_EXP, meanwhile the difference from P_1aIT and P_2aIT to P_EXP is reduced during the entire compression stroke. During peak pressure, P_1aIT and P_2aIT are inside pressure envelope, meanwhile P_piexp is outside pressure envelope. During exhaust cycle, P_1aIT and P_2aIT present a better trend in comparison to P_EXP than P_piexp.

The trends observed in Figure 4.13 for compression and expansion strokes couldn't be seen at any of the previous diagrams.

The last chart for 2000 rpm 8 bar is related to the in cylinder temperature evolution during -30 CAD and 90 CAD, in Figure 4.14.

Figure 4.14 – Results for in cylinder temperature trace obtained by engine CFD 3D model using different sets of boundary conditions, in comparison to experimental correlated data. Engine operating condition is 2000 rpm 3 bar, domain between -30 CAD and 90 CAD, range from 500 K to 2500 K.

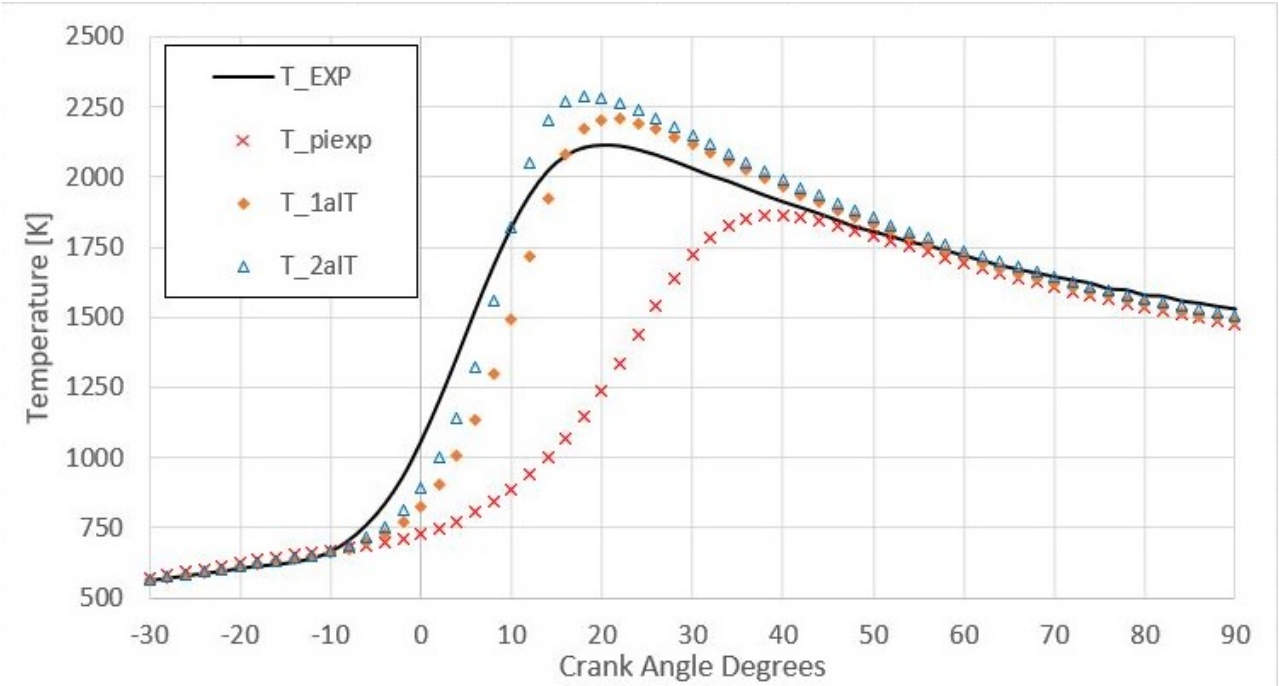

SOURCE: Elaborated by the author.

In Figure 4.14, engine CFD 3D results are presented using experimental intake pressure boundary conditions (T_piexp), which are correlated to section 4.1, fitted intake pressure boundary condition using first iteration wall temperatures (T_1aIT), correlated to subsection 4.5.1, and fitted intake pressure boundary condition using second iteration wall temperatures (T_2aIT), correlated to subsection 4.5.2. Experimental results (T_EXP) are presented for calculated in cylinder temperature for the cycle selected by the cycle selection procedure described in subsection 3.8.1.

In Figure 4.14, between -30 CAD and -10 CAD, all of the engine CFD 3D results are in good agreement to each other and also in good agreement with T_EXP. A few degrees after -10 CAD, T_1aIT and T_2aIT present similar trends to T_EXP, meanwhile T_piexp present completely different trends until 40 CAD. It is also noticeable that the rise in temperature for T_EXP starts and finishes earlier than T_1aIT and T_2aIT, which indicates differences in the combustion evolution process. Nevertheless, the peak temperature calculated is similar to T_EXP, T_1aIT and T_2aIT, and the angle for peak temperature is also similar between experimental calculated data and numerical results using fitted pressure as intake boundary

conditions.

The trends observed in Figure 4.8 through Figure 4.14 for engine operating conditions of 2000 rpm 8 bar, show that for this engine operating condition the proposed methodology for intake pressure treatment increase the accuracy of the engine CFD 3D model. This is clear for all of the results, once the trends for both in cylinder pressure and temperature are better captured using fitted intake pressure boundary conditions than experimental intake pressure boundary conditions. For 2000 rpm 8 bar, it can be seen a noticeable difference between first and second iteration wall temperature results, nevertheless this difference doesn't show a clear increase in accuracy for second iteration in comparison to first iteration, what is observed for engine operating condition of 2000 rpm 8 bar.

The increase in accuracy for 2000 rpm 8 bar can also be highlighted by the comparison of results for injected mass of fuel, trapped mass of air, lambda, IMEP and peak pressure, performed in Table 4.21.

Table 4.21 – Results calculated by engine CFD 3D model using different sets of boundary conditions, in comparison to experimental correlated data, for 2000 rpm 8 bar.

	Experiment	Engine CFD 3D		
Intake pressure boundary condition	-	Experiment	Fitted	Fitted
Iteration of the global HT model	-	-	1st	2nd
Injected mass of fuel [mg]	40.7	40.7	40.7	40.8
Trapped mass of air [mg]	343.4	439.9	356.2	354.4
Lambda [dim]	0.997	1.557	1.245	1.195
IMEP [bar]	7.95	8.28	8.39	8.72
P max [bar]	47.4	31.5	47.4	52.7

SOURCE: Elaborated by the author.

In Table 4.21, the increase in accuracy provided by the proposed methodology is clearly observed for results of trapped mass of air, lambda and P_max, meanwhile it cannot be clearly observed in terms of IMEP. Indeed, the proposed methodology reduce the accuracy of the engine CFD 3D model in terms of IMEP.

Based in Figure 4.8 through Figure 4.14 and in Table 4.21, it has been shown that the proposed methodology increased the accuracy of the engine CFD 3D model concerning the selected engine operating at 2000 rpm 8 bar, both qualitatively in terms of in cylinder pressure and temperature traces, and quantitatively in terms of trapped mass of air, lambda and peak pressure.

4.7 SUMMARIZE OF THE RESULTS

It is observed in the results presented from section 4.1 until subsection 4.6.2 that the engine CFD 3D model using the proposed methodology for analysis and treatment of intake pressure boundary conditions present results with better agreement to experimental correlated data than the direct use of experimental data as boundary condition.

These trends are observed quantitatively by the comparison of results in section 4.1 and subsection 4.5.1, in terms of trapped mass of air and lambda, for all of the engine operating conditions evaluated (1000 rpm 3 bar, 2000 rpm 3 bar, 2000 rpm 8 bar, 2500 3 bar, 2500 rpm 5 bar and 2500 rpm 8 bar). These trends are also observed qualitatively for 2000 rpm 3 bar and 2000 rpm 8 bar, for in cylinder pressure traces, pressure volume diagrams and in cylinder temperature. The trends observed for the selected engine operating conditions can also be observed for the other engine operating conditions, in such a manner that the proposed methodology systematically increases the agreement between engine CFD 3D results and experimental correlated data.

This way, it is observed that the proposed methodology for analysis of intake pressure boundary condition increases the accuracy of the engine CFD 3D model using RANS approach for all of the evaluated cases (1000 rpm 3 bar, 2000 rpm 3 bar, 2000 rpm 8 bar, 2500 rpm 3bar, 2500 rpm 5 bar, 2500 rpm 8 bar), as show in section 4.1 and subsection 4.5.1, in comparison to the direct use of experimental data for intake pressure boundary condition.

The charts for in cylinder pressure during intake stroke, for the selected engine operating conditions, show better agreement between experimental data and engine CFD 3D model using experimental intake pressure boundary condition. Nevertheless, considering engine CFD 3D model using experimental data for intake pressure boundary condition, this visual agreement is associated to what makes the charts for in cylinder pressure during combustion analysis interval or pressure volume diagrams so different, which is the systematic excess of air. The effect of pulsating flow at intake ducts of experimental test bench is the reduction of trapped mass of air, as a consequence of the reduction at volumetric efficiency, which cannot be captured by the engine CFD 3D model using RANS approach, when directly using experimental data for intake pressure boundary conditions.

The difference of in cylinder pressure between engine CFD 3D model using fitted pressure boundary conditions and experimental data observed at intake stroke charts is directly related to the proposed method to correct in cylinder trapped mass of air. The increase in the accuracy of the engine CFD 3D model observed in this thesis is only possible by two means: either resolving the pulsating flow and its effect at reducing trapped mass of air, or performing the pressure correction procedure proposed in this thesis. This way, the accuracy for in cylinder pressure during intake stroke is a trade off to increase accuracy at in cylinder pressure during combustion, and also to increase accuracy at trapped mass of air, lambda and P_max.

The reduction of the accuracy of the model observed for IMEP at 2000 rpm 8 bar, is an

extremely important result for future works, in terms of the improvement of the proposed methodology. Comparing Table 4.20 and Table 4.21, it is possible to observe that between first and second iteration wall temperatures, the IMEP values are always increased. Also, for 2000 rpm 3 bar and 2000 rpm 8 bar, the tendency for IMEP is always increasing, from experimental intake pressure boundary conditions to fitted pressure boundary conditions with first iteration wall temperatures, and from fitted pressure boundary conditions with first iteration wall temperatures to second iteration wall temperatures. Those trends indicate important situations on the combustion sub model used, which could be related to several parts of the referred sub model, and should be evaluated in future works.

It is important to highlight, at this point, that no validation procedure should be defined based exclusively in a single variable or a single analysis, once it can hide discrepancies between the proposed model results and the correlated experimental data. The comparison between engine CFD 3D results using intake pressure experimental boundary conditions and fitted pressure boundary conditions, considering engine operating condition of 2000 rpm 8 bar, shows clearly that fitted pressure boundary conditions increase the accuracy of the engine CFD 3D model, for all of the evaluated charts from Figure 4.1 to Figure 4.7, and also for 3 of the 4 cycle representative results at Table 4.21. The only result which don't follow this trend is the IMEP, and for a simple reason: the in cylinder pressure of the engine CFD 3D model using intake experimental boundary conditions is higher than experimental in cylinder pressure during compression and expansion strokes, and only during combustion the experimental pressure becomes higher. The cumulative result of those trends is observed at the IMEP values in Table 4.21.

The increase in the accuracy of an engine CFD 3D model in comparison to experimental results, systematically obtained for six different engine operating conditions, is the greatest achievement of this thesis. It is mandatory to highlight that the values of constants for adjustments of sub models, are not tuned for any case. It is unprecedented to present and evaluate simultaneously six different engine operating conditions, what is performed in this thesis, using engine CFD 3D model with the same values for all of the constants at each sub model.

The fact that engine CFD 3D model using the pressure correction procedure is performed with the same values for sub models constants, allows this model to, once it is validated using a standard verification and validation procedure, be used for interpolation or extrapolation demands, along with validated interpolation or extrapolation procedure.

The validation of the proposed methodology on the basis of a well established CFD 3D validation procedure is a proposal for future work which should be implemented as fast as possible. For this purpose, some intermediate tasks are needed, for example the verification of physical models for laminar flame speed, the implementation of the proposed methodology for the same engine with different intake duct geometry and for different engine, in order to confirm or deny the general application of the proposed hypothesis. Also, the pressure

correction procedure should be optimized, in order to reduce its computational cost. Another important task is to verify the sensibility of the engine CFD 3D model to different boundary conditions, which is a mandatory task on the trends of the ASME V&V 20 procedure. The procedures for interpolation and extrapolation of engine CFD 3D results, and their validations, are long term proposals for future work, and for such purposes, reliable procedures for interpolation or extrapolation of boundary conditions should be proposed and evaluated.

5 CONCLUSIONS

It is concluded based on the literature review that engine CFD 3D modelling state of the art shows trends of LES engine CFD 3D modelling at academy for several applications, although several of those applications are restricted to engine like or simplified geometries. Among the papers that present full geometry modelling, which includes from intake to exhaust flow boundaries, some of them use LES approach for turbulence, but many of them use RANS approach for turbulence. This way, RANS engine CFD 3D modelling is going to be used for some more years, still in academic research, specially with trends of verification and validation becoming more and more important for engine 3D modelling.

Other important trend in engine CFD 3D modelling is the CHT approach, which solves wall temperatures along with in cylinder reactive flow field. In this thesis, due to limited computational resources, a decoupled iterative CHT approach using a global heat transfer model is proposed, as a low cost alternative, although in literature most of the papers uses finite element approach to solve temperature distribution at combustion chamber, even if it means to work with simplified geometries or closed cycle simulations.

Probably the most important trend in engine CFD 3D modelling which is not so clear in literature is the verification and validation necessity. As engine CFD 3D results become more and more important, it is of vital importance to implement verification and validation procedures in order to offer not only results, but also quality of results. In this thesis, a method is proposed to increase the accuracy of an engine CFD 3D model using RANS approach, which is an important step towards standard verification and validation procedure.

It is concluded from the proposed methodology that, concerning the trends of engine CFD 3D verification and validation, the experimental information which is required by engine CFD 3D engineer or researcher must be defined before the start of the procedure, in order to define which engine CFD 3D results are going to be used for validation, and whether these values are available in the experiment. Most of this work depends on previous experience, in such a manner that the results obtained by this thesis are of vital importance for this task, and are a great contribution from this thesis to CTM-UFMG.

Concerning the proposed methodology for intake pressure correction, other options should be evaluated in order to obtain the same results. The use of engine 1D models is a possibility, but for this approach, these models must be validated as a bridge between engine experimental tests and engine CFD 3D models. Other task is to improve the results of the pressure correction procedure, in order to obtain more accurate results for trapped mass of air, lambda and IMEP, which is stated as a future work propose.

Perhaps the most important conclusion from the methodology proposed is that this method should be tested for other engine operating conditions, other fuels and other engines, in order to confirm or refuse the proposed hypothesis as a general recommendation for engine CFD 3D modelling using RANS approach for turbulence applied to naturally aspired engines.

It is concluded based on the results obtained that the unprecedented hypothesis proposed in this thesis is confirmed for the evaluated engine. The hypothesis proposed in section 4.2 states that engine CFD 3D models using RANS approach for turbulence cannot reproduce the trapped mass of air inside the cylinder of naturally aspired engines, and this way it cannot reproduce combustion process without changing the values of submodels constants. The hypothesis is tested for six different engine operating conditions, and for all of them the results are clear that the model overestimates the trapped mass of air.

This proposed hypothesis is associated in this thesis to the pulsating flow effects over volumetric efficiency, which is verified by several experimental publications in literature for long time, once RANS approach for turbulence cannot capture the detailed effects of pulsating flow over volumetric efficiency. This association is not tested for lack of time, and thus it is proposed as future work.

Although the methodology proposed increase the accuracy of the engine CFD 3D model for the six evaluated engine opperating conditions, it needs some improvement in order to make it capable of achieving validation against combustion experimental results such as IMEP. Several future work proposals are stated over the thesis, which are considered important tasks to overcome the weakness and increase the strengths of the proposed methodology.

It is also important to state that, once the proposed methodology is validated against six different engine operating conditions, it can be used at interpolation or extrapolation tasks, along with interpolation or extrapolation validated procedures.

5.1 FUTURE WORK PROPOSALS

Several future work proposals are described over the text. The most important ones are reinforced below:

- Implement the proposed methodology for different engine geometries and fuels, in order to evaluate if it can be considered a general consideration for engine CFD 3D modelling of naturally aspired engines;
- Update the global heat transfer model, with special focus on exhaust valve heat transfer correlations and constants, in order to produce a model capable of estimating wall temperatures without the necessity of a second iteration;
- Propose a method to evaluate the sensibility of the engine CFD 3D model to input data, in order to implement the standard method for verification and validation proposed at (ASME, 2009).

BIBLIOGRAPHY

ALKIDAS, A. C. *Effects of Operational Parameters on Structural Temperatures and Coolant Heat Rejection of a SI Engine*. [S.l.], 1993.

ALKIDAS, A. C. Combustion advancements in gasoline engines. *Energy Conversion and Management*, Elsevier, v. 48, n. 11, p. 2751–2761, 2007.

ANGELBERGER, C.; POINSOT, T.; DELHAY, B. *Improving near-wall combustion and wall heat transfer modeling in SI engine computations*. [S.l.], 1997.

BAI, C.; GOSMAN, A. Development of methodology for spray impingement simulation. *SAE transactions*, JSTOR, p. 550–568, 1995.

BAKER, D.; ASSANIS, D. A methodology for coupled thermodynamic and heat transfer analysis of a diesel engine. *Applied Mathmatical Modelling*, v. 18, p. 590–601, 1994.

BARATTA, M.; RAPETTO, N. Fluid-dynamic and numerical aspects in the simulation of direct cng injection in spark-ignition engines. *Computers & Fluids*, Elsevier, v. 103, p. 215–233, 2014.

BARROS, J. E. M. *Estudo de motores de combustão interna aplicando análise orientada a objetos*. Tese (Doutorado em Engenharia Mecânica) — Universidade Federal de Minas Gerais, Belo Horizonte, 2003.

BAUMANN, M.; MARE, F. D.; JANICKA, J. On the validation of large eddy simulation applied to internal combustion engine flows part ii: numerical analysis. *Flow, turbulence and combustion*, Springer, v. 92, n. 1-2, p. 299–317, 2014.

BAUMGARTEN, C. *Mixture Formation in Internal Combustion Engines*. Berlin Heidelberg: Springer-Verlag, 2006.

BENAJES, J.; OLMEDA, P.; MARTÍN, J.; BLANCO-CAVERO, D.; WAREY, A. Evaluation of swirl effect on the global energy balance of a hsdi diesel engine. *Energy*, Elsevier, v. 122, p. 168–181, 2017.

BERNARD, G.; LEBAS, R.; DEMOULIN, F.-X. *A 0D phenomenological model using detailed tabulated chemistry methods to predict diesel combustion heat release and pollutant emissions*. [S.l.], 2011.

BERNI, F.; CICALESE, G.; FONTANESI, S. A modified thermal wall function for the estimation of gas-to-wall heat fluxes in cfd in-cylinder simulations of high performance spark-ignition engines. *Applied Thermal Engineering*, Elsevier, v. 115, p. 1045–1062, 2017.

BOHAC, S. V.; BAKER, D. M.; ASSANIS, D. N. A global model for steady state and transient si engine heat transfer studies. *SAE transactions*, JSTOR, p. 196–214, 1996.

BORMAN, G.; NISHIWAKI, K. Internal-combustion engine heat transfer. *Progress in Energy and Combustion Sciences*, v. 13, n. 1, p. 1–46, 1987.

BROATCH, A.; OLMEDA, P.; MARGOT, X.; ESCALONA, J. New approach to study the heat transfer in internal combustion engines by 3d modelling. *International Journal of Thermal Sciences*, Elsevier, v. 138, p. 405–415, 2019.

BROATCH P. OLMEDA, A. G. J. S. A.; WAREY, A. Impact of swirl on in-cylinder heat transfer in a light-duty diesel engine. *Energy*, v. 119, p. 1010–1023, 2017.

BROEKAERT, S.; CUYPER, T. D.; PAEPE, M. D.; VERHELST, S. Experimental investigation of the effect of engine settings on the wall heat flux during hcci combustion. *Energy*, Elsevier, v. 116, p. 1077–1086, 2016.

BROEKAERT, S.; DEMUYNCK, J.; CUYPER, T. D.; PAEPE, M. D.; VERHELST, S. Heat transfer in premixed spark ignition engines part i: Identification of the factors influencing heat transfer. *Energy*, Elsevier, v. 116, p. 380–391, 2016.

BUHL, S.; DIETZSCH, F.; BUHL, C.; HASSE, C. Comparative study of turbulence models for scale-resolving simulations of internal combustion engine flows. *Computers & Fluids*, Elsevier, v. 156, p. 66–80, 2017.

CD-ADAPCO. *STAR-CD Version 4.20*: Methodology for internal combustion engine applications. New York, 2013.

CERDOUN, M.; CARCASCI, C.; GHENAIET, A. An approach for the thermal analysis of internal combustion engines' exhaust valves. *Applied Thermal Engineering*, Elsevier, v. 102, p. 1095–1108, 2016.

CERIT, M.; COBAN, M. Temperature and thermal stress analyses of a ceramic-coated aluminum alloy piston used in a diesel engine. *International Journal of Thermal Sciences*, Elsevier, v. 77, p. 11–18, 2014.

CEVIZ, M. Intake plenum volume and its influence on the engine performance, cyclic variability and emissions. *Energy Conversion and Management*, Elsevier, v. 48, n. 3, p. 961–966, 2007.

CLENCI, A. C.; IORGA-SIMĂN, V.; DELIGANT, M.; PODEVIN, P.; DESCOMBES, G.; NICULESCU, R. A cfd (computational fluid dynamics) study on the effects of operating an engine with low intake valve lift at idle corresponding speed. *Energy*, Elsevier, v. 71, p. 202–217, 2014.

COLIN, O.; BENKENIDA, A. The 3-zones extended coherent flame model (ecfm-3z) for computing premixed/diffusion combustion. *Oil & Gas Science and Technology*, EDP Sciences, v. 59, n. 6, p. 593–609, 2004.

COLIN, O.; BENKENIDA, A.; ANGELBERGER, C. 3d modeling of mixing, ignition and combustion phenomena in highly stratified gasoline engines. *Oil & gas science and technology*, EDP Sciences, v. 58, n. 1, p. 47–62, 2003.

COSTA, R. B. R. da. *Estudo experimental da tecnologia dual-fuel em motor de combustão interna utilizando biogás, GNV e etanol*. Dissertação (Mestrado em Engenharia Mecânica) — Universidade Federal de Minas Gerais, Belo Horizonte, 2017.

CUYPER, T. D.; BROEKAERT, S.; CHANA, K.; PAEPE, M. D.; VERHELST, S. Evaluation of empirical heat transfer models using tfg heat flux sensors. *Applied Thermal Engineering*, Elsevier, v. 118, p. 561–569, 2017.

DENG, B.; FU, J.; ZHANG, D.; YANG, J.; FENG, R.; LIU, J.; LI, K.; LIU, X. The heat release analysis of bio-butanol/gasoline blends on a high speed si (spark ignition) engine. *Energy*, Elsevier, v. 60, p. 230–241, 2013.

DENG, X.; LEI, J.; WEN, J.; WEN, Z.; SHEN, L. Numerical investigation on the oscillating flow and uneven heat transfer processes of the cooling oil inside a piston gallery. *Applied Thermal Engineering*, Elsevier, v. 126, p. 139–150, 2017.

DRAKE, M.; HAWORTH, D. Advanced gasoline engine development using optical diagnostics and numerical modeling. *Proceedings of the Combustion Institute*, Elsevier, v. 31, n. 1, p. 99–124, 2007.

DUCLOS, J.; ZOLVER, M.; BARITAUD, T. 3d modeling of combustion for di-si engines. *Oil & Gas Science and Technology*, EDP Sciences, v. 54, n. 2, p. 259–264, 1999.

DUDAREVA, N. Y.; ENIKEEV, R.; IVANOV, V. Y. Thermal protection of internal combustion engines pistons. *Procedia Engineering*, Elsevier, v. 206, p. 1382–1387, 2017.

EÇA, L.; HOEKSTRA, M. A procedure for the estimation of the numerical uncertainty of cfd calculations based on grid refinement studies. *Journal of Computational Physics*, Elsevier, v. 262, p. 104–130, 2014.

FAN, X.; CHE, Z.; WANG, T.; LU, Z. Numerical investigation of boundary layer flow and wall heat transfer in a gasoline direct-injection engine. *International Journal of Heat and Mass Transfer*, Elsevier, v. 120, p. 1189–1199, 2018.

FINLAY, I.; GALLACHER, G.; BIDDULPH, T.; MARSHALL, R. The application of precision cooling to the cylinder-head of a small, automotive, petrol engine. *SAE transactions*, JSTOR, p. 399–410, 1988.

FINOL, C.; ROBINSON, K. Thermal modelling of modern engines: a review of empirical correlations to estimate the in-cylinder heat transfer coefficient. *Proceedings of the institution of mechanical engineers, part D: journal of automobile engineering*, Sage Publications Sage UK: London, England, v. 220, n. 12, p. 1765–1781, 2006.

FONSECA, L.; OLMEDA, P.; NOVELLA, R.; VALLE, R. M. Internal combustion engine heat transfer and wall temperature modeling: An overview. *Archives of Computational Methods in Engineering*, Oct 2019. ISSN 1886-1784.

FONSECA, L. G. *Caracterização do escoamento de ar em um motor de combustão interna utilizando mecânica dos fluidos computacional*. Dissertação (Mestrado em Engenharia Mecânica) — Universidade Federal de Minas Gerais, Belo Horizonte, 2014.

GE, H.-W.; SHI, Y.; REITZ, R. D.; WICKMAN, D. D.; WILLEMS, W. Optimization of a hsdi diesel engine for passenger cars using a multi-objective genetic algorithm and multi-dimensional modeling. *SAE International Journal of Engines*, JSTOR, v. 2, n. 1, p. 691–713, 2009.

GIANNAKOPOULOS, G.; FROUZAKIS, C. E.; BOULOUCHOS, K.; FISCHER, P. F.; TOMBOULIDES, A. Direct numerical simulation of the flow in the intake pipe of an internal combustion engine. *International Journal of Heat and Fluid Flow*, Elsevier, v. 68, p. 257–268, 2017.

GÜRBÜZ, H. Parametrical investigation of heat transfer with fast response thermocouple in si engine. *Journal of Energy Engineering*, v. 142, n. 4, p. 04016014, 2016.

HAN, Z.; PARRISH, S. E.; FARRELL, P. V.; REITZ, R. D. Modeling atomization processes of pressure-swirl hollow-cone fuel sprays. *Atomization and sprays*, Begel House Inc., v. 7, n. 6, 1997.

HAN, Z.; REITZ, R. D. Turbulence modeling of internal combustion engines using rng κ-ε models. *Combustion science and technology*, Taylor & Francis, v. 106, n. 4-6, p. 267–295, 1995.

HAN, Z.; REITZ, R. D. A temperature wall function formulation for variable-density turbulent flows with application to engine convective heat transfer modeling. *International journal of heat and mass transfer*, Elsevier, v. 40, n. 3, p. 613–625, 1997.

HANRIOT, S. d. M.; QUEIROZ, J. M.; MAIA, C. B. Effects of variable-volume helmholtz resonator on air mass flow rate of intake manifold. *Journal of the Brazilian Society of Mechanical Sciences and Engineering*, Springer, v. 41, n. 2, p. 79, 2019.

HANRIOT, S. de M. *Estudo dos fenômenos pulsantes do escoamento de ar nos condutos de admissão em motores de combustão interna*. Tese (Doutorado em Engenharia Mecânica) — Universidade Federal de Minas Gerais, Belo Horizonte, 2001.

HASSE, C. Scale-resolving simulations in engine combustion process design based on a systematic approach for model development. *International Journal of Engine Research*, SAGE Publications Sage UK: London, England, v. 17, n. 1, p. 44–62, 2016.

HEYWOOD, J. B. Engine combustion modelling - an overview. In: SPRINGER US. *Combustion modeling in reciprocating engines*. New York, 1980.

HEYWOOD, J. B. *Internal Combustion Engine Fundamentals*. New York: McGraw-Hill, 2018.

INAGAKI, M.; NAGAOKA, M.; HORINOUCHI, N.; SUGA, K. Large eddy simulation analysis of engine steady intake flows using a mixed-time-scale subgrid-scale model. *International Journal of Engine Research*, SAGE Publications Sage UK: London, England, v. 11, n. 3, p. 229–241, 2010.

INCROPERA, F. P.; LAVINE, A. S.; BERGMAN, T. L.; DEWITT, D. P. *Fundamentals of heat and mass transfer*. [S.l.]: Wiley, 2007.

IRIMESCU, A.; MEROLA, S. S.; TORNATORE, C.; VALENTINO, G. Development of a semi-empirical convective heat transfer correlation based on thermodynamic and optical measurements in a spark ignition engine. *Applied Energy*, Elsevier, v. 157, p. 777–788, 2015.

JAMES, E. H. *Combustion modelling in spark ignition engines*. 1984.

JEEVANASHANKARA; MADHUSUDANA, C.; KULKARNI, M. Thermal contact conductances of metallic contacts at low loads. *Applied Energy*, v. 35, n. 2, p. 151 – 164, 1990.

JEMNI, M. A.; KANTCHEV, G.; ABID, M. S. Influence of intake manifold design on in-cylinder flow and engine performances in a bus diesel engine converted to lpg gas fuelled, using cfd analyses and experimental investigations. *Energy*, Elsevier, v. 36, n. 5, p. 2701–2715, 2011.

JOINT COMMITTEE FOR GUIDES IN METROLOGY. *JCGM 100:2008*: Evaluation of measurement data - guide to the expression of uncertainty in measurement. [S.l.], 2008. 120 p.

KHALILARYA, S.; NEMATI, A. et al. A numerical investigation on the influence of egr in a supercharged si engine fueled with gasoline and alternative fuels. *Energy conversion and management*, Elsevier, v. 83, p. 260–269, 2014.

KIKUSATO, A.; KUSAKA, J.; DAISHO, Y. *A Numerical Study on Predicting Combustion Chamber Wall Surface Temperature Distributions in a Diesel Engine and their Effects on Combustion, Emission and Heat Loss Characteristics by Using a 3D-CFD Code Combined with a Detailed Heat Transfer Model*. [S.l.], 2015.

LI, Y.; KONG, S.-C. Coupling conjugate heat transfer with in-cylinder combustion modeling for engine simulation. *International Journal of Heat and Mass Transfer*, Elsevier, v. 54, n. 11-12, p. 2467–2478, 2011.

LINSE, D.; KLEEMANN, A.; HASSE, C. Probability density function approach coupled with detailed chemical kinetics for the prediction of knock in turbocharged direct injection spark ignition engines. *Combustion and Flame*, Elsevier, v. 161, n. 4, p. 997–1014, 2014.

LIU, Y.; GUESSOUS, L.; SANGEORZAN, B.; ALKIDAS, A. Laboratory experiments on oil-jet cooling of internal combustion engine pistons: Area-average correlation of oil-jet impingement heat transfer. *Journal of Energy Engineering*, American Society of Civil Engineers, v. 141, n. 2, p. C4014003, 2014.

LU, Y.; ZHANG, X.; XIANG, P.; DONG, D. Analysis of thermal temperature fields and thermal stress under steady temperature field of diesel engine piston. *Applied Thermal Engineering*, Elsevier, v. 113, p. 796–812, 2017.

LV, J.; WANG, P.; BAI, M.; LI, G.; ZENG, K. Experimental visualization of gas–liquid two-phase flow during reciprocating motion. *Applied Thermal Engineering*, Elsevier, v. 79, p. 63–73, 2015.

MA, P. C.; EWAN, T.; JAINSKI, C.; LU, L.; DREIZLER, A.; SICK, V.; IHME, M. Development and analysis of wall models for internal combustion engine simulations using high-speed micro-piv measurements. *Flow, Turbulence and Combustion*, Springer, v. 98, n. 1, p. 283–309, 2017.

MANDANIS, C.; SCHMITT, M.; KOCH, J.; WRIGHT, Y. M.; BOULOUCHOS, K. Wall heat flux and thermal stratification investigations during the compression stroke of an engine-like geometry: A comparison between les and dns. *Flow, Turbulence and Combustion*, Springer, v. 100, n. 3, p. 769–795, 2018.

MARE, F. di; KNAPPSTEIN, R. Statistical analysis of the flow characteristics and cyclic variability using proper orthogonal decomposition of highly resolved les in internal combustion engines. *Computers & Fluids*, Elsevier, v. 105, p. 101–112, 2014.

MARE, F. di; KNAPPSTEIN, R.; BAUMANN, M. Application of les-quality criteria to internal combustion engine flows. *Computers & Fluids*, Elsevier, v. 89, p. 200–213, 2014.

MASOULEH, M. G.; KESKINEN, K.; KAARIO, O.; KAHILA, H.; WRIGHT, Y. M.; VUORINEN, V. Flow and thermal field effects on cycle-to-cycle variation of combustion: scale-resolving simulation in a spark ignited simplified engine configuration. *Applied energy*, Elsevier, v. 230, p. 486–505, 2018.

MEHDIPOUR, R.; BANIAMERIAN, Z.; DELAURÉ, Y. Three dimensional simulation of nucleate boiling heat and mass transfer in cooling passages of internal combustion engines. *Heat and Mass Transfer*, Springer, v. 52, n. 5, p. 957–968, 2016.

MELO, T. C. C. de. *Análise experimental e simulação computacional de um motor flex operando com diferentes misturas de etanol hidratado na gasolina*. Tese (Doutorado em Engenharia Mecânica) — Universidade Federal do Rio de Janeiro, Rio de Janeiro, 2012.

MENEVEAU, C.; POINSOT, T. Stretching and quenching of flamelets in premixed turbulent combustion. *Combustion and Flame*, Elsevier, v. 86, n. 4, p. 311–332, 1991.

MEZHER, H.; CHALET, D.; MIGAUD, J.; CHESSE, P. Frequency based approach for simulating pressure waves at the inlet of internal combustion engines using a parameterized model. *Applied energy*, Elsevier, v. 106, p. 275–286, 2013.

MICHL, J.; NEUMANN, J.; ROTTENGRUBER, H.; WENSING, M. Derivation and validation of a heat transfer model in a hydrogen combustion engine. *Applied Thermal Engineering*, Elsevier, v. 98, p. 502–512, 2016.

MILLO, F.; LUISI, S.; BOREAN, F.; STROPPIANA, A. Numerical and experimental investigation on combustion characteristics of a spark ignition engine with an early intake valve closing load control. *Fuel*, Elsevier, v. 121, p. 298–310, 2014.

MISDARIIS, A.; VERMOREL, O.; POINSOT, T. Les of knocking in engines using dual heat transfer and two-step reduced schemes. *Combustion and Flame*, Elsevier, v. 162, n. 11, p. 4304–4312, 2015.

NETTO, N. A. D. *Estudo experimental de tecnologias que visam a maximização da eficiência de conversão de combustível em um motor monocilindro de pesquisa*. Dissertação (Mestrado em Engenharia Mecânica) — Universidade Federal de Minas Gerais, Belo Horizonte, 2018.

NIJEWEME, D. O.; KOK, J.; STONE, C.; WYSZYNSKI, L. Unsteady in-cylinder heat transfer in a spark ignition engine: experiments and modelling. *Proceedings of the Institution of Mechanical Engineers, Part D: Journal of Automobile Engineering*, Sage Publications Sage UK: London, England, v. 215, n. 6, p. 747–760, 2001.

OLMEDA, P.; MARTÍN, J.; NOVELLA, R.; CARREÑO, R. An adapted heat transfer model for engines with tumble motion. *Applied energy*, Elsevier, v. 158, p. 190–202, 2015.

PARIOTIS E.G., K. G.; RAKOUPOULOS, C. Comparative analysis of three simulation models applied on a motored internal combustion engine. *Energy Conversion and Management*, v. 60, p. 45–55, 2012.

PEREIRA, L. V. M. *Estudo Experimental da Influência de um Ressonador de Volume Variável na Massa de Ar Admitida por um Motor de Combustão Interna*. Tese (Doutorado em Engenharia Mecânica) — Universidade Federal de Minas Gerais, Belo Horizonte, 2008.

PERINI, F.; MILES, P. C.; REITZ, R. D. A comprehensive modeling study of in-cylinder fluid flows in a high-swirl, light-duty optical diesel engine. *Computers & Fluids*, Elsevier, v. 105, p. 113–124, 2014.

PIEDRAHITA, C. A. R. *Contribución al conocimiento del comportamiento térmico y la gestión térmica de los motores de combustión interna alternativos.* Tese (Doutorado) — Universitat Politècnica de València, 2009.

QI, Y.; DONG, L.; LIU, H.; PUZINAUSKAS, P.; MIDKIFF, K. Optimization of intake port design for si engine. *International Journal of Automotive Technology*, Springer, v. 13, n. 6, p. 861–872, 2012.

RAMOS, J. I. *Internal combustion engine modelling*. New York: CRC Press, 1989.

RANZ, W.; MARSHALL, W. R. et al. Evaporation from drops. *Chem. eng. prog*, v. 48, n. 3, p. 141–146, 1952.

RASHEDUL, H.; KALAM, M.; MASJUKI, H.; ASHRAFUL, A.; IMTENAN, S.; SAJJAD, H.; WEE, L. Numerical study on convective heat transfer of a spark ignition engine fueled with bioethanol. *International Communications in Heat and Mass Transfer*, Elsevier, v. 58, p. 33–39, 2014.

REITZ, R. et al. Modeling atomization processes in high-pressure vaporizing sprays. *Atomisation and Spray Technology*, v. 3, n. 4, p. 309–337, 1987.

ROBERT, A.; RICHARD, S.; COLIN, O.; MARTINEZ, L.; FRANCQUEVILLE, L. D. Les prediction and analysis of knocking combustion in a spark ignition engine. *Proceedings of the Combustion Institute*, Elsevier, v. 35, n. 3, p. 2941–2948, 2015.

ROSA, N.; VILLEDIEU, P.; DEWITTE, J.; LAVERGNE, G. A new droplet-wall interaction model. *ICLASS06-167*, ICLASS-2006, 2006.

SAKOWITZ, A.; MIHAESCU, M.; FUCHS, L. Flow decomposition methods applied to the flow in an ic engine manifold. *Applied Thermal Engineering*, Elsevier, v. 65, n. 1-2, p. 57–65, 2014.

ŠARIĆ, S.; BASARA, B.; ŽUNIČ, Z. Advanced near-wall modeling for engine heat transfer. *International Journal of Heat and Fluid Flow*, Elsevier, v. 63, p. 205–211, 2017.

SCHIFFMANN, P.; GUPTA, S.; REUSS, D.; SICK, V.; YANG, X.; KUO, T.-W. Tcc-iii engine benchmark for large-eddy simulation of ic engine flows. *Oil & Gas Science and Technology*, EDP Sciences, v. 71, n. 1, 2016.

SCHMITT, M.; BOULOUCHOS, K. Role of the intake generated thermal stratification on the temperature distribution at top dead center of the compression stroke. *International Journal of Engine Research*, SAGE Publications Sage UK: London, England, v. 17, n. 8, p. 836–845, 2016.

SCHMITT, M.; FROUZAKIS, C. E.; TOMBOULIDES, A. G.; WRIGHT, Y. M.; BOULOUCHOS, K. Direct numerical simulation of the effect of compression on the flow, temperature and composition under engine-like conditions. *Proceedings of the Combustion Institute*, Elsevier, v. 35, n. 3, p. 3069–3077, 2015.

SCHMITT, M.; FROUZAKIS, C. E.; WRIGHT, Y. M.; TOMBOULIDES, A. G.; BOULOUCHOS, K. Direct numerical simulation of the compression stroke under engine-relevant conditions: Evolution of the velocity and thermal boundary layers. *International Journal of Heat and Mass Transfer*, Elsevier, v. 91, p. 948–960, 2015.

SCHMITT, M.; FROUZAKIS, C. E.; WRIGHT, Y. M.; TOMBOULIDES, A.; BOULOUCHOS, K. Direct numerical simulation of the compression stroke under engine relevant conditions: Local wall heat flux distribution. *International Journal of Heat and Mass Transfer*, Elsevier, v. 92, p. 718–731, 2016.

SCHMITT, M.; FROUZAKIS, C. E.; WRIGHT, Y. M.; TOMBOULIDES, A. G.; BOULOUCHOS, K. Investigation of wall heat transfer and thermal stratification under engine-relevant conditions using dns. *International Journal of Engine Research*, SAGE Publications Sage UK: London, England, v. 17, n. 1, p. 63–75, 2016.

SILVA, E.; OCHOA, A.; HENRÍQUEZ, J. Analysis and runners length optimization of the intake manifold of a 4-cylinder spark ignition engine. *Energy Conversion and Management*, Elsevier, v. 188, p. 310–320, 2019.

SOUZA, G. R. de; PELLEGRINI, C. de C.; FERREIRA, S. L.; PAU, F. S.; ARMAS, O. Study of intake manifolds of an internal combustion engine: A new geometry based on experimental results and numerical simulations. *Thermal Science and Engineering Progress*, Elsevier, v. 9, p. 248–258, 2019.

TANOV, S.; SALVADOR-IBORRA, J.; ANDERSSON, Ö.; OLMEDA, P.; GARCÍA, A. Influence of the number of injections on piston heat rejection under low temperature combustion conditions in an optical compression-ignition engine. *Energy Conversion and Management*, Elsevier, v. 153, p. 335–345, 2017.

TAYLOR, G. I. The instability of liquid surfaces when accelerated in a direction perpendicular to their planes. i. *Proceedings of the Royal Society of London. Series A. Mathematical and Physical Sciences*, The Royal Society London, v. 201, n. 1065, p. 192–196, 1950.

THE AMERICAN SOCIETY OF MECHANICAL ENGINEERS. *ASME V&V 20-2009*: Standard for verification and validation in computational fluid dynamics and heat transfer. New York, 2009. 88 p.

TOOSI, A. N.; FAROKHI, M.; MASHADI, B. Application of modified eddy dissipation concept with large eddy simulation for numerical investigation of internal combustion engines. *Computers & Fluids*, Elsevier, v. 109, p. 85–99, 2015.

TORREGROSA, A.; BROATCH, A.; OLMEDA, P.; CORNEJO, O. Experiments on subcooled flow boiling in ic engine-like conditions at low flow velocities. *Experimental Thermal and Fluid Science*, Elsevier, v. 52, p. 347–354, 2014.

TORREGROSA, A.; BROATCH, A.; OLMEDA, P.; SALVADOR-IBORRA, J.; WAREY, A. Experimental study of the influence of exhaust gas recirculation on heat transfer in the firedeck of a direct injection diesel engine. *Energy Conversion and Management*, Elsevier, v. 153, p. 304–312, 2017.

TORREGROSA, A.; OLMEDA, P.; DEGRAEUWE, B.; REYES, M. A concise wall temperature model for di diesel engines. *Applied Thermal Engineering*, Elsevier, v. 26, n. 11-12, p. 1320–1327, 2006.

TORREGROSA P. OLMEDA, J. M. A.; ROMERO, C. A tool for predicting the thermal performance of a diesel engine. *Heat Transfer Engineering*, v. 32, n. 10, p. 891–904, 2011.

VERSTEEG, H. K.; MALALASEKERA, W. *An introduction to computational fluid dynamics: the finite volume method*. [S.l.]: Pearson education, 2007.

WAKIL, M. M. E.; UYEHARA, O.; MYERS, P. *A theoretical investigation of the heating-up period of injected fuel droplets vaporizing in air*. [S.l.], 1954.

WANG, P.; HAN, K.; YOON, S.; YU, Y.; LIU, M. The gas-liquid two-phase flow in reciprocating enclosure with piston cooling gallery application. *International Journal of Thermal Sciences*, Elsevier, v. 129, p. 73–82, 2018.

WANG, P.; LIANG, R.; YU, Y.; ZHANG, J.; LV, J.; BAI, M. The flow and heat transfer characteristics of engine oil inside the piston cooling gallery. *Applied Thermal Engineering*, Elsevier, v. 115, p. 620–629, 2017.

WANG, T.; LI, W.; JIA, M.; LIU, D.; QIN, W.; ZHANG, X. Large-eddy simulation of in-cylinder flow in a disi engine with charge motion control valve: Proper orthogonal decomposition analysis and cyclic variation. *Applied Thermal Engineering*, Elsevier, v. 75, p. 561–574, 2015.

WOSCHNI, G. *A universally applicable equation for the instantaneous heat transfer coefficient in the internal combustion engine*. [S.l.], 1967.

XING, T. A general framework for verification and validation of large eddy simulations. *Journal of Hydrodynamics*, Springer, v. 27, n. 2, p. 163–175, 2015.

YAKHOT, V.; ORSZAG, S.; THANGAM, S.; GATSKI, T.; SPEZIALE, C. Development of turbulence models for shear flows by a double expansion technique. *Physics of Fluids A: Fluid Dynamics*, AIP, v. 4, n. 7, p. 1510–1520, 1992.

YAKHOT, V.; ORSZAG, S. A. Renormalization group analysis of turbulence. i. basic theory. *Journal of scientific computing*, Springer, v. 1, n. 1, p. 3–51, 1986.

YAMAKAWA, M.; YOUSO, T.; FUJIKAWA, T.; NISHIMOTO, T.; WADA, Y. .; SATO, K.; YOKOHATA, H. Combustion technology development for a high compression ratio si engine. *SAE International Journal of Fuels and Lubricants*, JSTOR, v. 5, n. 1, p. 98–105, 2012.

ZHANG, L. Parallel simulation of engine in-cylinder processes with conjugate heat transfer modeling. *Applied Thermal Engineering*, Elsevier, v. 142, p. 232–240, 2018.

A DETAILED GEOMETRY

The geometry of the simulation domain consists in volume of fluid region inside in cylinder, intake and exhaust ducts (manifolds, runners, ports), as already described in section 3.3. The generation of the geometry described in Figure 3.3 is based in the CAD solid parts assembled in Figure 3.2.

The superimposition of both Figure 3.2 and Figure 3.3 is described in Figure A.1, where it is highlighted the correspondence between the geometry of the simulation domain and the geometry of the solid parts which represent the selected engine.

Figure A.1 – Geometry of the simulation domain highlighted inside engine parts. Geometry volumes are highlighted for in cylinder (red) and intake and exhaust ducts (blue).

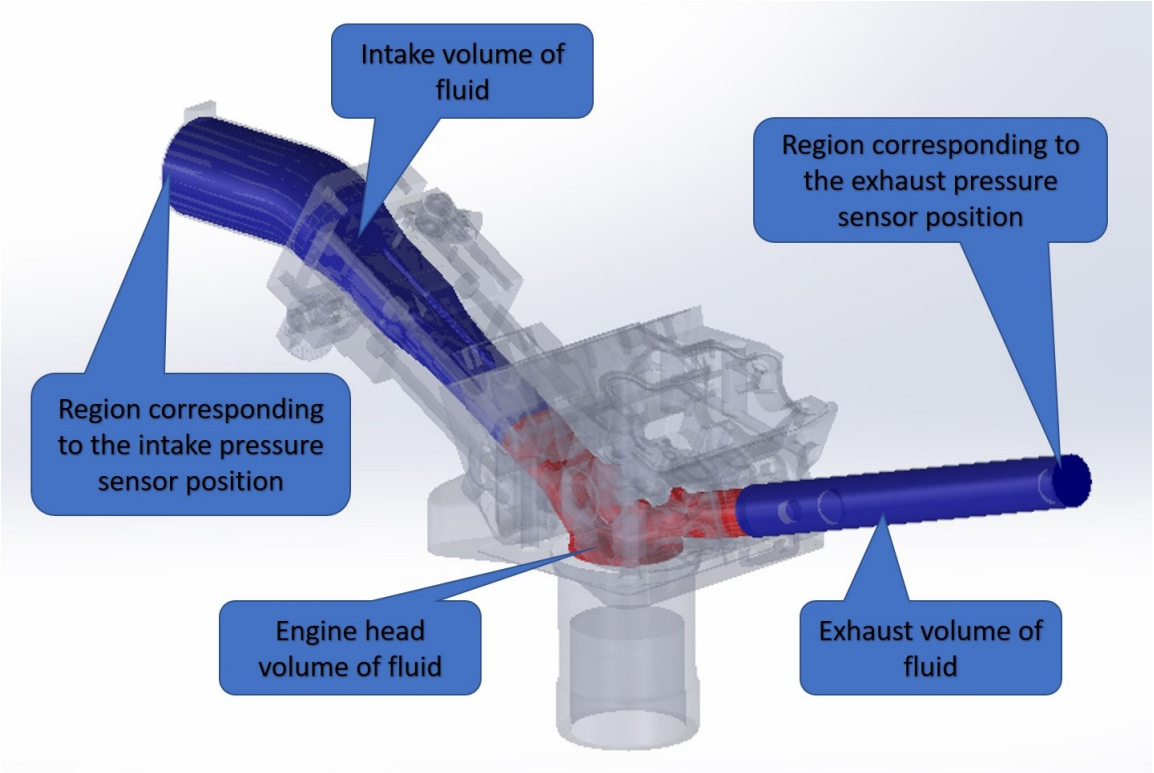

SOURCE: Elaborated by the author.

In Figure A.1, volume of fluid corresponding to intake and exhaust manifolds is highlighted in blue, engine head volume of fluid which comprises in cylinder and ports is highlighted in red, and the solid parts of the engine are transparent.

The dimensions of the simulation domain are described in Figure A.2, for the complete geometry including intake and exhaust manifolds, along with in cylinder, intake port and exhaust port. Special attention is paid to the dimensions of the in cylinder, intake port and exhaust port region, which are described in Figure A.3.

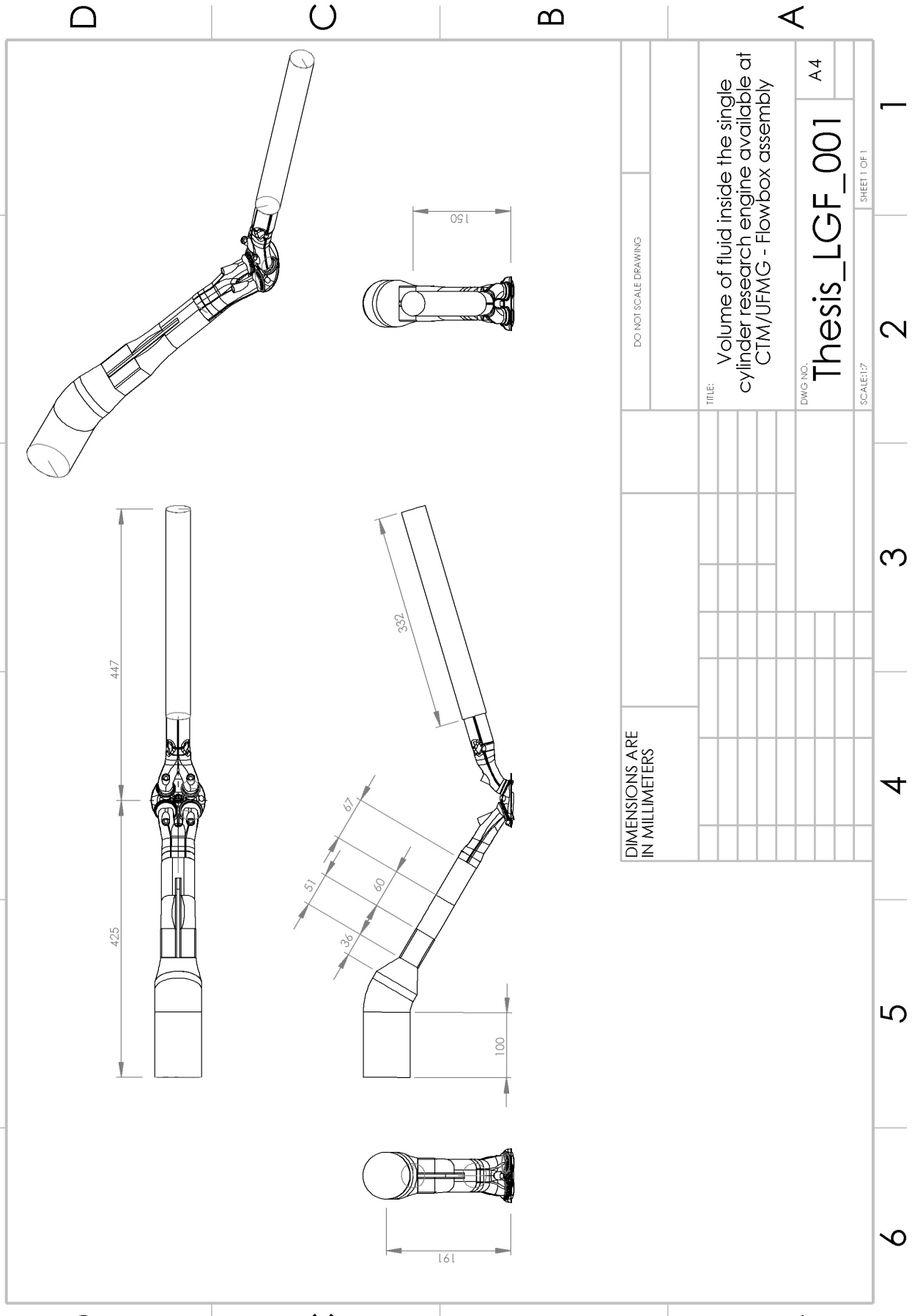

Figure A.2 – Internal volume geometry details: complete geometry.

SOURCE: Elaborated by the author.

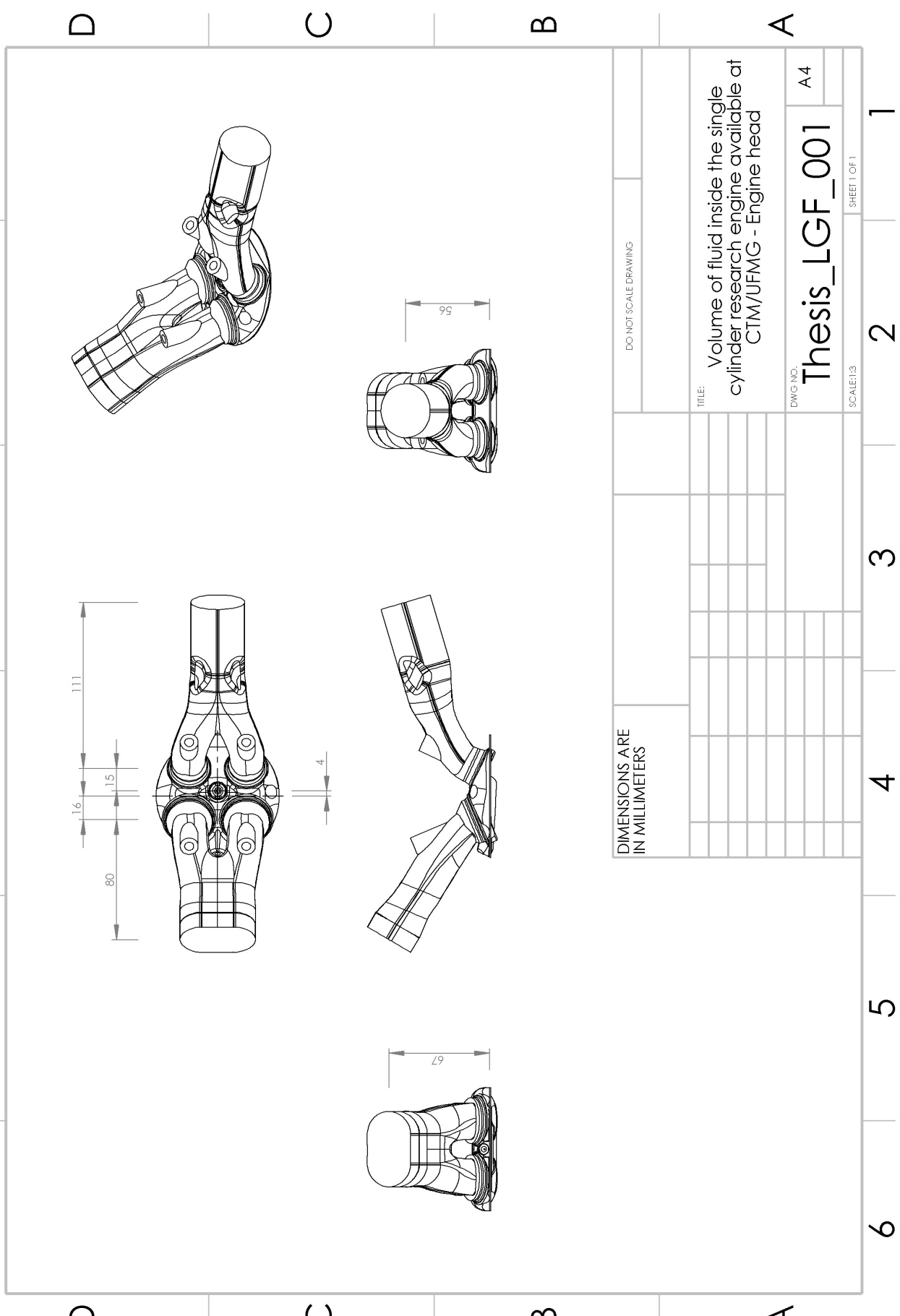

Figure A.3 – Internal volume geometry details: engine head internal volume.

SOURCE: Elaborated by the author.

B GRID DETAILED INFORMATION

B.1 GRID REFINEMENT

The geometry of the simulation domain, described in Figure 3.3, is used in the grid generation procedure, described in Figure 2.1. In this thesis, the grid study is based in the simulation of the engine CFD 3D model using four different grids systematically refined. The refinement is based in the characteristic length h calculated by Equation 3.1, and the reference h value for each grid is described in Table B.1.

Table B.1 – Reference characteristic length for different grids used in this work.

GRID	1	2	3	4
h $[mm]$	1.000	0.900	0.810	0.720
r $[dim]$	-	1.11	1.11	1.11

SOURCE: Elaborated by the author.

B.1.1 2D Template

Considering the grid generation procedure and the in cylinder geometry, a 2D template is generated based on cylinder bore, cylinder dome and valves relative geometry for each grid in Table B.1. The 2D template for each grid is similar to the one illustrated by Figure B.1, which is the 2D template for grid 1 in Table B.1, with a reference characteristic length of 1mm.

Figure B.1 – Template 2D generated for the in cylinder geometry of the evaluated engine. Template corresponding to grid 1, for a characteristic length of 1 mm.

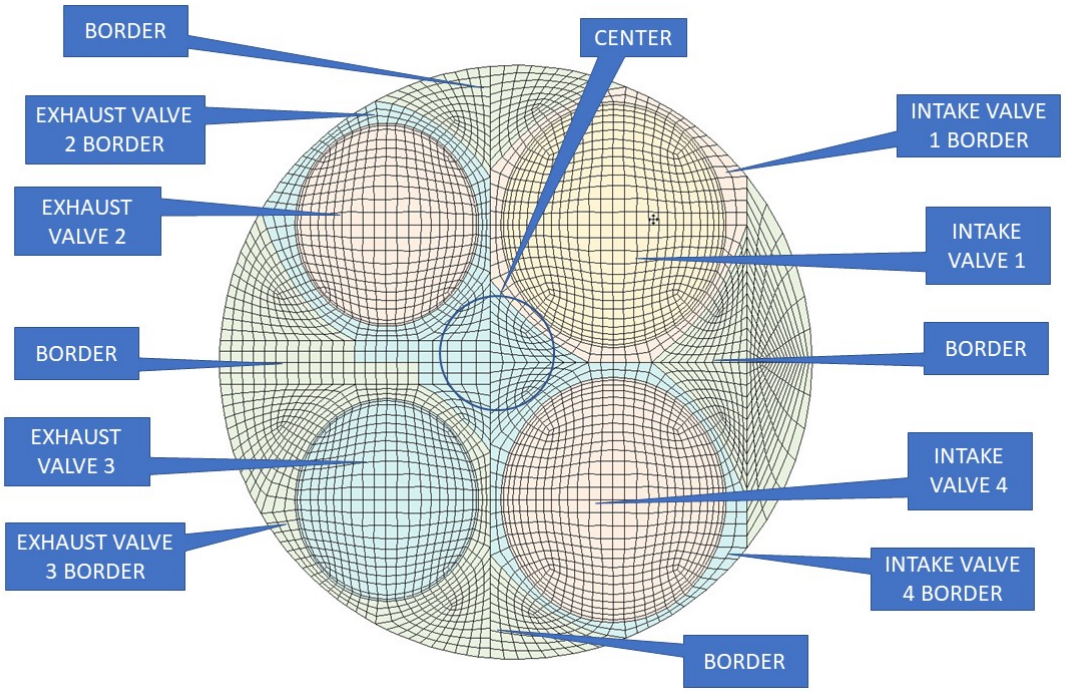

SOURCE: Elaborated by the author.

The size of the area elements in Figure B.1 changes from one region to the other, and also inside each region it can be seen by visual inspection some variation in the element size. This variation is quantified by the average data for each grid region in Table B.2.

Table B.2 – Reference characteristic length for different regions into the 2D template for the grid 1, with reference characteristic length of 1 mm.

REGION	AREA $[mm^2]$	NUMBER OF CELLS	CHARACTERISTIC AREA $[mm^2]$	CHARACTERISTIC LENGTH $[mm]$
CENTER	260.9	188	1.388	1.178
BORDER	1312.6	1066	1.231	1.110
INTAKE VALVE 1	829.5	640	1.296	1.138
INTAKE VALVE 1 BORDER	199.4	128	1.558	1.248
EXHAUST VALVE 2	557.2	448	1.244	1.115
EXHAUST VALVE 2 BORDER	266.1	332	0.802	0.895
EXHAUST VALVE 3	557.2	448	1.244	1.115
EXHAUST VALVE 3 BORDER	265.9	332	0.801	0.895
INTAKE VALVE 4	829.5	640	1.296	1.138
INTAKE VALVE 4 BORDER	199.0	128	1.555	1.247
TOTAL	5277.4	4350	1.213	1.101

SOURCE: Elaborated by the author.

From Table B.2, it can be seen that although the reference characteristic length for grid 1 is 1 mm, it is not possible to achieve this exact value for the 2D template, but an approximate value of 1.101 mm. It is also clear in Table B.2 that the characteristic length presents great variations between different regions of the 2D template. This is also observed for all of the other grids in Table B.1, in such a manner that for 2D template, the actual characteristic length in Table B.3 is slightly different then the reference one in Table B.1.

Table B.3 – Actual characteristic length and grid refinement factor of the 2D template for all of the grids evaluated.

GRID	1	2	3	4
h $[mm]$	1.101	0.892	0.824	0.704
r $[dim]$	-	1.234	1.083	1.170

SOURCE: Elaborated by the author.

B.1.2 Grids at Top Dead Center and Bottom Dead Center

Based in the 2D templates for those the characteristic lengths are described in Table B.3, a 3D template is then generated for each grid. The 3D template is used along with cylinder, intake and exhaust ports geometry to generate a reference mesh, which is used to create the mesh database necessary for simulation of moving parts. After the database is ready, the mesh for any instant during engine cycle can be previously generated and evaluated.

The most important examples for 3D instant grid evaluation are the grid at top dead center (TDC), similar to Figure B.2, and bottom dead center (BDC), similar to Figure B.3, which are examples of grid visualization relatives to grid 1, with a characteristic length of 1 mm. Both Figure B.2 and Figure B.3 are visualizations of instant grids produced during the grid generation process, in such a manner that only intake and exhaust ports are described. The grid for both intake and exhaust manifolds is inserted in another step of simulation workflow.

Figure B.2 – Instant 3D grid at top dead center, for the grid 1 with a characteristic length of 1 mm.

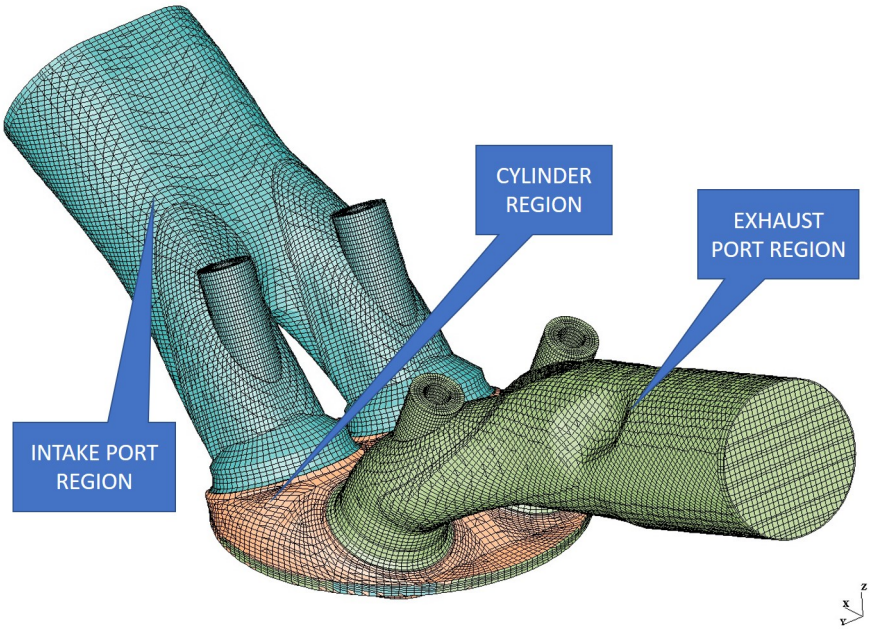

SOURCE: Elaborated by the author.

It has already been observed that the reference characteristic length in Table B.1 can not be exactly obtained by the 2D template, due to technical attributes of the grid generation process. It is also true in terms of the 3D instant grids at TDC and BDC, that the reference characteristic length can not be exactly achieved. The actual characteristic length and the grid refinement factor for all of the evaluated grids is described in Table B.4, for TDC and BDC instant grids, without the inclusion of inatake and exhasut manifolds.

The results in Table B.4 for the actual characteristic length associated to all of the grids show that the reference characteristic length can not be exactly reproduced by the 3D grid at both TDC and BDC instant grids. The grids at BDC present a much better approximation to the reference characteristic length for all of the grids in Table B.4, due to the volume available for

Figure B.3 – Instant 3D grid at bottom dead center, for the grid 1 with a characteristic length of 1 mm.

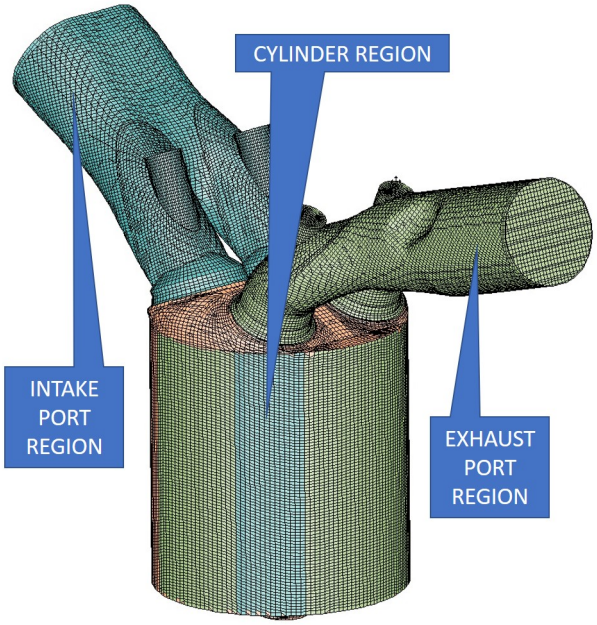

SOURCE: Elaborated by the author.

Table B.4 – Actual characteristic length and grid refinement factor of the 3D grids at TDC and BDC for all of the grids evaluated.

GRID	1	2	3	4
h (TDC) $[mm]$	0.980	0.846	0.756	0.715
r $[dim]$	-	1.159	1.119	1.057
h (BDC) $[mm]$	1.044	0.898	0.803	0.734
r $[dim]$	-	1.163	1.118	1.094

SOURCE: Elaborated by the author.

the grid generator in order to distribute and control the volume of each cell group. On the other hand, the grids at TDC are much harder to make it closer to the reference characteristic length, due to the cell compression performed by the grid generator.

B.1.3 Troubleshooting during grid generation

Nevertheless, there is still some troubleshooting needed before running any case, because several problems can occur during mesh generation, specially the construction of negative volume cells. The best grid correction step is the one after generating the reference mesh, before creating mesh database, and the best way to correct it is to run some case to check if the grid is good enough to perform calculation without causing divergence or instability of the simulation. This way, an iterative process is used, generating the reference mesh, correcting the reference mesh problems, and running a reference case, until the grid is able to run an entire cycle calculation, and can be considered finished. Only after running a test case, the grid can be considered finished, and able to be used for engine calculation, because any divergence occurring after this step should be attributed to the physics of the case,

and not to the quality of the grid itself.

B.1.4 Results for grid refinement

The values presented at Table B.4 for grids similar to the ones described at Figure B.2 and Figure B.3 are referent to the grid generation process. After including the grids for both intake and exhaust manifolds, and performing the simulations, the actual values for all of those quantities are different. One example of a complete grid used in the simulation is Figure 3.4, including intake and exhaust manifold grids.

The grid showed in Figure 3.4 represents the complete simulation domain at bottom dead center, and is associated to a reference characteristic length of 1 mm. In Figure 3.4, the intake and exhaust regions are highlighted as the group between manifold and port grids, as they are evaluated at the results of the simulation from one flow boundary to the respective valve curtain surface. The valve curtain surfaces are not clear in Figure 3.4, but are implicit along with the complete domain. This instant grid illustrates the association between manifolds, ports and cylinder, along with their relative sizes at BDC, and is used to represent all of the grids evaluated in this study. The results obtained by all of the simulations performed for the grid dependence study are presented in Table B.5, in terms of characteristic length at TDC.

Table B.5 – Characteristic length h [*mm*] of the TDC, for different grids, evaluated for total grid and for in cylinder, intake and exhaust regions.

GRID	1		2		3		4	
TOTAL	0.983	-1.73%	0.891	-1.05%	0.799	-1.35%	0.735	0.89%
CYLINDER	0.883	-11.7%	0.778	-13.6%	0.716	-11.6%	0.640	-12.2%
INTAKE	0.976	-2.43%	0.889	-1.21%	0.797	-1.59%	0.737	1.11%
EXHAUST	1.011	1.10%	0.908	-0.86%	0.813	0.39%	0.743	1.95%

SOURCE: Elaborated by the author.

In Table B.5, the values observed for the characteristic length at TDC for all of the grids evaluated in the grid dependence study are presented, along with the relative difference to the respective characteristic length reference value in Table B.1. The characteristic length results at TDC in Table B.5 are also presented for the total grid, along with specific results for in cylinder, intake and exhaust grids, highlighted in Figure 3.4. For all of the grids evaluated, the in cylinder characteristic length is more than 10% smaller than reference characteristic length, which is a consequence of the reduction in the simulation volume at TDC.

The TDC characteristic length for the total grid presents relative differences always smaller than 2.0% for all of the grids, although the in cylinder characteristic lengths are considerably different than the reference ones. This can be explained by the results for the number of cells in Table B.6, at TDC, for all of the grids evaluated.

From Table B.6, it can be seen that the coarser grid has 1.7 million cells at TDC, but for the same grid at the same instant, the intake number of cells is 1.2 million and the exhaust is 0.5 million. This way, the in cylinder number of cells represents 3% of the total number of cells.

Table B.6 – Number of cells at TDC, for the total domain, and for in cylinder, intake and exhaust regions.

GRID	1	2	3	4
TOTAL	1,703,791	2,288,175	3,165,894	4,059,032
CYLINDER	62,849	91,996	117,916	165,277
INTAKE	1,167,444	1,542,108	2,138,521	2,702,778
EXHAUST	473,498	654,071	909,457	1,190,977

SOURCE: Elaborated by the author.

Even with a 10% smaller characteristic length, the in cylinder number of cells is dominated by the manifold cells which represent almost 97% of the total number of cells. For this reason, the total characteristic length of each grid at TDC presents small relative differences to the respective reference values.

It is also important to highlight that, due to the complex phenomena taking place inside the cylinder, the characteristic length for all of the grids evaluated would be considered to coarse for several analysis, except for the average cycle analysis. The details of the reactive flow field, flame front propagation and other phenomena can only be captured by much finer in cylinder grids.

Similar to what is performed for TDC, the results obtained by all of the simulations performed for the grid dependence study are presented in Table B.7, in terms of characteristic length at BDC.

Table B.7 – Characteristic length h [mm] of the BDC, for different grids, evaluated for total grid and for in cylinder, intake and exhaust regions.

GRID	1		2		3		4	
TOTAL	0.998	-0.19%	0.891	-0.22%	0.799	-0.44%	0.735	1.22%
CYLINDER	1.042	4.20%	0.778	1.13%	0.716	1.53%	0.640	0.74%
INTAKE	0.975	-2.46%	0.889	-1.26%	0.797	-1.64%	0.737	1.12%
EXHAUST	1.011	1.10%	0.908	0.86%	0.813	0.39%	0.743	1.95%

SOURCE: Elaborated by the author.

In Table B.7, the values observed for the characteristic length at BDC for all of the grids evaluated in the grid dependence study are presented, along with the relative difference to the respective characteristic length reference value in Table B.1. The characteristic length results at BDC in Table B.7 are also presented for the total grid, along with specific results for in cylinder, intake and exhaust grids, highlighted in Figure 3.4. For all of the grids evaluated, the in cylinder characteristic length presents relative differences smaller than 5%, in comparison to the respective reference characteristic length in Table B.1.

The results obtained by the grid dependence study for the total number of cells at BDC are presented at Table B.8, for all of the grids evaluated.

In terms of BDC, the total number of cells for the coarser grid is almost 2.1 million, and the in cylinder number of cells is 0.4 million, this way the in cylinder number of cells represent

Table B.8 – Number of cells at BDC, for the total domain, and for in cylinder, intake and exhaust regions.

GRID	1	2	3	4
TOTAL	2,082,415	2,858,443	3,946,080	5,148,748
CYLINDER	435,329	653,624	885,958	1,244,385
INTAKE	1,173,588	1,550,748	2,150,665	2,713,386
EXHAUST	473,498	654,071	909,457	1,190,977

SOURCE: Elaborated by the author.

almost 21.0% of the total number of cells. It is important to highlight that this is the maximum in cylinder number of cell during the engine cycle.

Comparing Table B.5 and Table B.7, it is important to highlight that the relative differences in terms of characteristic length are always negative at TDC and always positive at BDC, in comparison to reference values in Table B.1. It is also important to state that TDC and BDC values are extreme ones for in cylinder characteristic length, this way the characteristic length of the in cylinder grid changes during the entire cycle, between the values presented at Table B.5 and Table B.7.

B.1.5 Closing remarks associated to grid refinement

The trends observed in subsection B.1.1 through subsection B.1.4 show that each grid present variable characteristic length in space, due to necessity to comprise the grid at the different regions of the cylinder, and in time, due to the strategies to represent movements of piston and valves. The use of a representative characteristic length is a classical strategy to control grid refinement, in order to attend to standard verification and validation procedures (ASME, 2009). Although, when it comes to internal combustion engine CFD 3D modelling, even if it is possible to make the value of the characteristic length close to the reference value, or still if the tolerance for the variation of the characteristic length is enlarged to 15% or 20%, it is almost impossible to control the refinement between different instants of the simulation, and maintain the reference characteristic length.

In this thesis, the classical grid refinement strategy is implemented, and the results are presented using such strategy, once this is one of the best practices available. Although, it is important to highlight that if it is an objective to control the grid refinement in order to calculate simulation uncertainty, a new strategy to control grid refinement must be proposed, in order to consider the natural variations of the in cylinder grid size during the cycle. One natural way should be to control grid refinement in terms of dimensionless grid factors, which is beyond the scope of this thesis, and is proposed as future work.

B.2 RESULTS FOR DIFFERENT GRIDS

The grid dependence study is performed by systematic simulation of a specific condition of the evaluated system, and evaluation of the results obtained for a specific physical quantity by different grids, in order to verify how the selected results of the proposed model change after successive refinements in the spatial discretization of the simulation domain.

In this thesis, the grid dependence study is performed by simulating the engine CFD 3D model presented in chapter 3 using the grids described in section B.1 for the engine operating condition of 1000 rpm 3 bar. The engine CFD 3D model calculates transient results for several variables concerning the flow field at intake and exhaust ducts (manifolds, ports) and inside the cylinder. Based on those transient results, some cycle average representative results can be calculated, which are of special interest in terms of comparison to experimental data.

B.2.1 Selection of trapped mass of air

The transient results can be used as evaluation results for the grid independence results, but they are not the most recommended, not even the by standard procedures (ASME, 2009). One of the standard procedures available nowadays recommends that the variable selected for evaluation of the grid refinement is an average value for the entire calculation, and also an important one for the physics involved. The instantaneous value of the in cylinder flow field velocities are important for the physics, but it is known by previous experience that the use of those quantities implies in the definition of an statistical method to evaluate the grid dependence. It is also important to highlight that the proposed model uses RANS approach for turbulence, this way the instant values are just average ones, in such a manner the all of the fluctuations are represented by the proposed turbulence model. For those reasons, it does not seem a wise choice to evaluate the grid dependence by the flow field velocities, once the engine CFD 3D model calculates only an average representative value for this quantity.

Cycle average quantities are much more effective when it comes to the comparison of results between different grids, and the IMEP of the engine cycle is one of the most important cycle average values which could be calculated by an engine CFD 3D model, in order to compare with experimental data. This way, the first choice in this thesis was to evaluate the change in IMEP for 1000 rpm 3 bar, calculated by the four different grids described in section B.1. During the simulation phase, the results obtained by all of the grids for 1000 rpm 3 bar, using experimental intake pressure boundary condition, presented excess of air, similar to what is described in section 4.1. But at that point in the project, the pulsating flow head loss method described in section 2.3 was not even an option, once the systematic excess of air for six different engine operating conditions had not been obtained.

The results obtained by the four grids presented excess of air, in such a manner that in cylinder lambda calculated by the engine CFD 3D model could not fit the required value by the experimental data for the selected case, so lambda was not an option. The injected mass of fuel

was not an option, once it is not a results of the refinement of the grid. The only variable which was connected to the IMEP, and could be evaluated for all of those grids was the trapped mass of air.

Considering the first approach for the grid dependence study, the selection of the trapped mass of air was the last choice. Although, it came out at the end of the project that the same trapped mass of air became the most important result in all of the simulations using experimental data for intake pressure boundary condition. This same quantity is directly related to the volumetric efficiency of the engine, and it comes out that the engine CFD 3D result for trapped mass of air is also the result calculated by the same model for volumetric efficiency.

This way, the trapped mass of air was not the first choice for the evaluation variable used at the grid dependence study, but after the results of this project, the natural selection of any grid dependence study for engine CFD 3D modelling of naturally aspired engines is trapped mass of air. This is for the following reasons:

- It is a cycle average value, which produce an efficient comparison between different grids;
- It is an essential result of the engine CFD 3D model using experimental data boundary conditions, considering the pulsating flow head loss method;
- It is a result sensitive to the grid refinement, but not so sensitive as instant values, as would be valve curtain velocities or curtain instant mass flow.

This way, it is not necessary to attend to experimental data for lambda, injected mass of fuel, and especially to IMEP, during the grid dependence study. It is only necessary to evaluate how the trapped mass of air changes for the different grids at the same engine operating condition, despite the excess of air and the misfire or low quality combustion calculations. The adjustment of the model to produce good quality combustion calculations only comes after the end of the grid dependence study, and after the pulsating flow head loss method implementation.

B.2.2 Grid dependence results

The results for the grid dependence study, considering the cycle average trapped mass of air, are presented in Table B.9, along with the computational cost associated to each grid.

The engine CFD 3D simulations performed at all of the four grids in Table B.9 involves the following information:

- The simulations are performed running three cycles, and using the results of the third cycle;
- The simulations start at 330.1 CAD and finish at 2,521.0 CAD, with a main time step of 0.1 CAD;

Table B.9 – Computational cost for different grids.

GRID	1	2	3	4
Characteristic length [mm]	1.000	0.900	0.810	0.729
Trapped air mass [mg]	212.4	211.0	210.4	208.4
$\Delta\phi\%$	-	-0.69%	-0.29%	-0.96%
Total number of time steps	22,295	22,480	22,295	22,295
Total time for simulation [hours]	364.8	518.8	707.2	964.0
Time per time step [s]	58.9	83.1	114.2	155.7
Time per time step per processor [s]	2.18	3.08	4.23	5.77

SOURCE: Elaborated by the author.

- The first time step is 1 and the last time step is 21,965;
- The simulations are performed at servers with similar capacities, all using 27 parallel processes and 16 physical cores;

It is observed in Table B.9 that grid 2 spent almost 200 time steps more the other ones, and that all of the simulations performed more time steps than the last one. This is due to the operations of restarting, which increase the total amount of time steps.

In Table B.9, the results for trapped mass of air obtained by the four grids evaluated in this study are presented, along with the relative variation between consecutive grids $\Delta\phi\%$ calculated by Equation 3.2. The grids are indicated by the representative characteristic length, and for each grid the complete information is described in section B.1. For all of the grids, the following information is available concerning computational cost: total number of time steps; total time spent by all of the three cycles, including the restarting operation, in hours of simulation; the average time per time step, in seconds; the average time per time step per processor, also in seconds.

The first important information that comes out from Table B.9 is that it consumed 2,555 hours of simulation, or almost four months of 30 days, simulating 24 hours a day. This is just the time in operation, and does not consider the time the servers are stopped due to energy loss, license server loss and others.

Two important observations are made, considering the further simulation of other grids. The first one deals with the simulation of a fifth grid considering the same grid refinement factor of 1.11, which would require a grid with a characteristic length of 0.656 [mm]. Considering the rate of increase in the time per time step, and estimating a rate of 1.3 for grid 5, the time per time step in grid 5 would be 202.4 s, which would demand more 1,253 extra hours of simulation, or 52 extra days of simulation.

The variation of trapped mass of air between consecutive grids, $\Delta\phi\%$, is always is always smaller than 1.0%, for example, between grids 1 and 2, it is -0.7%. It is also important to observe that, the variation between grids 1 and 4, should it be considered, is -1.9%, this way it is greater than 1.0%. Even in such case, the comparison between the greatest variation, between grids 1 and 4, and the estimated computational cost for a fifth grid, makes it clear that the extra grid

should not be evaluated. The increase in computational cost does not makes it affordable to spent more time, in a calculation with consecutive differences smaller than 1.0%, and with the greatest difference smaller than 2.0%.

The second important information is about the attendance to standard procedure available nowadays. The best practice available recommends a grid refinement factor always greater than 1.3, when it comes to verification and validation procedure. One thing to note is that it is clearly stated during this thesis that no verification and validation is proceeded, indeed, the method developed in this thesis is of great importance in order to proceed with verification and validation workflows, in such a manner it is not possible to proceed a verification and validation procedure for different engine operating conditions without a method similar to the one proposed in section 2.3. The other one is an estimation of the computational cost demanded for another grid which would attend to the recommended value of grid refinement factor. The grid refinement factor between grids 1 and 3 is smaller than 1.3, than the only grid available for the recommended procedure is grid 4. The increase in computational cost between grids 1 and 4 is 2.64, in such a manner the smaller estimate value for the increase in computational cost, with the same infrastructure, would be 2.5 between grid 4 and the next grid to attend to the standard. The estimated time per time step would by 389 seconds, which for 22,295 time steps would demand 100 extra days of simulation.

Considering the results in terms of trapped mass of air and $\Delta\phi\%$, and also the estimations in terms of computational cost for extra simulations, the grid dependence study is considered concluded, and grid 2 is selected as the best trade off between quality of results and computational cost.

B.3 TIME STEP

The evaluation of the change in the results due to a change in the time step is the last step in the grid dependence study performed in this thesis. Once grid 2 is already selected as the best trade off between quality of results and computational cost, it is used for the time step refinement.

The variable selected for the time step evaluation is the trapped mass of air, similar to the grid test. Once the available time for the simulations was almost all consumed due to the grid test, only one extra time step is evaluated. In case, the engine CFD 3D model using grid 2 is evaluated for a reference time step of 0.05 CAD, which is half of the time step used for the grid test. The results for the time step evaluation are presented in Table B.10.

The engine CFD 3D simulations performed at both time steps in Table B.10 involves the following information:

- The simulations are performed running three cycles, and using the results of the third cycle;

Table B.10 – Time step evaluation

TIME STEP	1	2
Time Step [CAD]	0.10	0.05
Trapped air mass [mg]	211.0	209.2
$\Delta\phi\%$	-	-0.83%
Initial time step	1	1
Final time step	21,965	43,931
Total number of time steps	22,480	44,647
Total time for simulation [hours]	518.8	915.8
Time per time step [s]	83.1	73.8
Time per time step per processor [s]	3.08	2.76

SOURCE: Elaborated by the author.

- The simulations start at 330.1 CAD and finish at 2,521.0 CAD;
- The simulations are performed at servers with similar capacities, all using 27 parallel processes and 16 physical cores;

The results in Table B.10 for the trapped mass of air and for variation of trapped mass of air show a relative decrease smaller than 1.0%, associated to an increase of almost 100% in the computational cost. This way, the time step of 0.1 CAD is selected as the best trade off between quality of results and computational cost.

Although, it is interesting to observe in Table B.10 that the time per time step is reduced from 0.1 CAD to 0.05 CAD. This is due to the smaller number of iterations at each time step, in order to achieve convergence. Nevertheless, the decrease in the time per time step is much smaller than the increase in the total number of time steps, which is practically double.

B.4 CONCLUSIONS OF THE GRID DEPENDENCE STUDY

Based on the information in section B.1, subsection B.1.4, and section B.3, the following conclusions are drawn.

The grid refinement based on the characteristic length is not the best strategy to control grid refinement between consecutive grids, concerning engine CFD 3D modelling. This is due to the inherent complex grid generation process, which inducess several variations in the characteristic length for the same grid. In this thesis, it is the best alternative, but for future works, new approaches should be evaluated in order to achieve a better control of the grid refinement process.

Concerning the grid dependence study and the time step evaluation, the results presented and lead to the selection of grid 2, with a reference characteristic length of 0.9 mm, and time step of 0.1 CAD, always considering the compromising between quality of results and computational cost.

Considering the selection of the trapped mass of air as the evaluation result, it is strongly recommended, based on the exposed in subsection B.1.4 that the grid dependence study for engine CFD 3D models using experimental data for intake pressure boundary condition is trapped mass of air as evaluation variable, for both grid and time step refinement evaluation.